MULTISCALE EVOLUTION OF SOUTHEAST US STORMS AND THEIR ENVIRONMENTS

A Dissertation

by

MATTHEW C. BROWN

Submitted to the Graduate and Professional School of
Texas A&M University
in partial fulfillment of the requirements for the degree of

DOCTOR OF PHILOSOPHY

Chair of Committee,	Christopher J. Nowotarski
Committee Members,	Kenneth P. Bowman
	Craig C. Epifanio
	Robert D. Hetland
Head of Department,	R. Saravanan

December 2021

Major Subject: Atmospheric Sciences

ABSTRACT

The evolution of atmospheric features across multiple spatiotemporal scales combine to influence the ability for environments to support severe convection and produce damaging winds, hail, and tornadoes. Determining the nature of these influences can help improve our understanding and prediction of these severe convective hazards. Such advances are especially pertinent for the Southeast US whose storm characteristics – namely the prevalence of storms occurring in high-shear, low-CAPE environments (HSLC), for which predictability is inherently lowered, and socioeconomic vulnerabilities – compound existing forecast uncertainty. This dissertation sets out to reduce these uncertainties by examining how variability across three spatiotemporal scales – climate , synoptic, and storm-scale – contribute to the prevalence and underlying characteristics of Southeast severe convection. On the climate scale, several atmospheric and Gulf of Mexico SST patterns are shown to modulate Southeast storm environments in ways that favor the development of widespread tornado outbreaks. Furthermore, a subset of cool season outbreak patterns contribute to the development of HSLC conditions, suggesting that their associated CAPE deficits have some large-scale origin which may lend increased predictability to their associated tornadoes. On the synoptic scale, storm environments evolving across local sunset are shown to change differently depending on the amount of CAPE and shear present pre-sunset, contributing to subsequent changes in storm mode and tornadogenesis frequency. Lastly on the storm-scale, simulations of low-CAPE supercells occurring during this near-sunset period exhibit storm updrafts which increase in depth, width, and strength in the presence of a rapidly destabilizing background environment. These enhancements are primarily attributed to off-hodograph propagation, which act to increase storm-relative flow beyond what is predicted by the base-state hodograph evolution alone. The sum of these results serves to advance our physical model and prediction of Southeast US severe storms and tornadoes.

DEDICATION

To my loving and supportive family and friends, whose unwavering support through my entire undergraduate and graduate careers have kept me sane, humble, and motivated to push forward to to this finish line; to the amazing teachers and mentors I have had the opportunity to encounter at Penn State and Texas A&M, particularly Dr. Raymond Najjar and Dr. Andrew Dzambo whose encouragement during METEO 003 helped a freshman hospitality management student make one of the best decisions he could have ever made:

Words cannot express how blessed I am to have crossed paths with each and every one of you.

ACKNOWLEDGEMENTS

First, I need to extend my the deepest gratitude to my advisor, Chris Nowotarski, for his support, guidance, and patience throughout my graduate career. His mentorship has helped me navigate the ups and downs of graduate school – classes, conferences, publishing, and a global pandemic to boot – and it is because of him that I am a better scientist and a better person today then when I first came to him 5 years ago. I would also like to recognize the Nowotarski research group – especially Marc, Leland, and Justin – who, beyond their invaluable input and support, have become like family to me. Thanks are also in order for my numerous collaborators through various phases of my PhD research, including Andrew R. Dean, Bryan T. Smith and Richard L. Thompson, John M. Peters, and Casey E. Davenport. The research presented later in this dissertation would not be the same without their constructive feedback, fresh ideas, willingness to share code and data, and overall support. Huge thanks as well to Kyle Wodzicki not only for his unending support of TAMU ATMO graduate students for several years, but also his fantastic LaTeX script used to build this dissertation document.

CONTRIBUTORS AND FUNDING SOURCES

Contributors

This work was supported by an advisory committee consisting of Professor Christopher Nowotarski (advisor), Professor Kenneth Bowman, and Professor Craig Epifanio of the Texas A&M University Department of Atmospheric Sciences, and Dr. Robert Hetland of Pacific Northwest National Laboratory (formerly with the Texas A&M University Department of Oceanography).

The analyses presented in Chapter 2 were performed using self-organizing map (SOM) code provided by Professor Christopher Nowotarski. These efforts were published in 2020 in a Journal of Climate article listed in the References section. The analyses presented in Chapter 3 were performed with data and input from Andrew R. Dean, Ryan Jewell, Bryan T. Smith and Richard L. Thompson of the Storm Prediction Center (SPC), as well as entrainment CAPE (ECAPE) code and input from Professor John M. Peters of the Naval Postgraduate School Department of Meteorology. These efforts were published in 2021 in a Weather and Forecasting article also listed in the References section. The analyses presented in Chapter 4 were conducted using the base state substitution (BSS) code and input from Professor Casey E. Davenport of the University of North Carolina at Charlotte.

All other work conducted for this dissertation was completed by the student independently.

Funding Sources

This work was made possible in part by the National Science Foundation (NSF) under grant Grant AGS-1928319. Its contents are solely the responsibility of the authors and do not necessarily represent the official views of NSF.

TABLE OF CONTENTS

LIST OF FIGURES

FIGURE Page

LIST OF TABLES

1. INTRODUCTION AND BACKGROUND

The focus of CONUS severe convective storms research for the last several decades has remained largely fixed on the Great Plains and its associated storm characteristics, notably their increased prevalence during late afternoon hours and warm season months (e.g., Kelly et al. 1978; Brooks et al. 2003; Anderson-Frey et al. 2016; Anderson-Frey et al. 2017), as well as their prototypical environments marked by ample wind shear (both low- and deep-layer) and instability (e.g., Rasmussen and Blanchard 1998; Thompson et al. 2003; Thompson et al. 2013). As a result, our understanding and prediction of storms in different environments has progressed slower by comparison. This scientific deficit, however, has given rise to new areas of severe convective storms research in recent years, including a renewed focus on the southeastern United States.

Long recognized as a secondary area of interest in the US storm and tornado climatologies (Kelly et al. 1978; Schaefer et al. 1980), the Southeast presents a unique challenge to researchers and forecasters alike. Numerous studies have noted that the tornado characteristics of this region represent a departure from those associated with Great Plains severe convection. These include the increased prevalence of nocturnal and cold season events, as well as non-supercellular modes (Brooks et al. 2003; Trapp et al. 2005; Ashley et al. 2019). Furthermore, many of these non-traditional tornadoes occur in environments which, while strongly sheared, lack appreciable buoyancy – hence their moniker high-shear, low-CAPE (HSLC; Dean and Schneider 2008; Guyer and Dean 2010; Sherburn and Parker 2014; Sherburn et al. 2016). While studies like Gropp and Davenport (2018) have characterized the response of high-CAPE storms to the cooling and stabilization of the near-sunset period known as the early evening transition (EET), it remains unclear how the EET looks for pre-sunset HSLC environments and what impacts this evolution has on the maintenance of HSLC storm updrafts. These complicating factors result in overall reduced probability of detection and increased false alarm rates for their associated convective hazards (Brotzge et al. 2013; Anderson-Frey et al. 2016; Anderson-Frey et al. 2019). Numerous socioeconomic factors further contribute to this uncertainty and tornado vulnerability, including increased mobile home density, high poverty rates, and projected changes in population beyond the suburbs (e.g. Simmons and Sutter 2007; Ashley et al. 2008; Strader et al. 2017). The sum of these factors make Southeast storms not only difficult to predict, but particularly dangerous as evidenced by recent deadly severe weather outbreaks (e.g, CDC 2012; May and Bigham 2012; Knupp et al. 2014).

While substantial inroads have been made by the aforementioned studies in characterizing Southeast storms and their associated predictability, several questions remain regarding the physical processes contributing to Southeast storm maintenance and tornadogenesis, particularly during evening hours and in HSLC environments. For instance, to what extent do large-scale atmospheric patterns modulate Southeast environments in ways that can favor widespread severe convection and increased risk for tornadoes? Once these favorable environments are in place, how do they evolve on smaller spatiotemporal timescales, such as during the EET, and influence the characteristics and tornadogenesis potential of subsequent storms? Lastly, what factors govern the maintenance and forcing of low-CAPE storm updrafts occurring during this transitional period, and how do these compare to the factors relevant to high-CAPE storms?

This dissertation seeks to investigate these differing scales of environmental evolution through a variety of analysis methods – including advanced statistical methods, utilization of storm reports, reanalysis data, and near-storm proximity soundings, and high-resolution modeling. Chapter 2 of this analysis will begin on the seasonal/sub-seasonal and regional scales, examining the numerous broad features that have been shown to influence regional storm environment, including jet stream/streak strength and positioning (Uccellini and Johnson 1979; Kloth and Davies-Jones 1980; Maddox and Doswell III 1982) , Gulf of Mexico sea surface temperatures (Thompson et al. 1994; Edwards and Weiss 1996; Molina et al. 2016; Jung and Kirtman 2016), and other large scale variations in temperature, pressure and moisture as they relate to Southeast tornado outbreaks. Chapter 3 will examine the near-storm environments of Southeast storms occurring in the vicinity of the EET, and determine how pre-sunset CAPE and shear values influence subsequent environmental evolution and the ability for storms to persist into evening hours. Chapter 4 will incorporate these environmental evolution pathways into an idealized modeling framework towards understanding EET impacts on updraft characteristics in HSLC storms. Finally, Chapter 5 will synthesize the findings from the precedent chapters and propose future avenues for Southeast and HSLC research.

2. SOUTHEASTERN U.S. TORNADO OUTBREAK LIKELIHOOD USING DAILY CLIMATE INDICES*

2.1 Introduction

A multitude of thermodynamic and kinematic factors spanning multiple spatiotemporal scales influence the formation of tornadoes, such that forecasting them remains challenging. Despite this complexity, numerous studies over the preceding decades have identified storm environment characteristics that favor tornadoes and tornado outbreaks. These features range from the synoptic scale, including the positioning of upper and mid-level troughs, jet streaks, air-mass boundaries, regional moisture and instability, and low-level jet variability (e.g., Uccellini and Johnson 1979; Kloth and Davies-Jones 1980; Maddox and Doswell III 1982; Atkins et al. 1999; Thompson and Edwards 2000; Munoz and Enfield 2011), down to more localized characteristics of the near-storm environment, such as convective available potential energy (CAPE), storm relative helicity (SRH), lifting condensation level (LCL), and both deep (0-6 km) and low-level (0-1 km) shear (e.g., Davies and Johns 1993; Rasmussen and Blanchard 1998; Markowski et al. 1998a; Edwards and Thompson 2000; Thompson et al. 2003; Rasmussen 2003; Thompson et al. 2007).

Though questions still remain regarding how synoptic and mesoscale processes affect regional storm environments, less is known about global-scale patterns that lead to conducive synoptic/regional patterns for tornadoes. A number of recent papers have probed the relationships between various large-scale circulation and pressure patterns and CONUS tornadoes. Perhaps the most thoroughly explored of these relationships is with the El Niño Southern Oscillation (ENSO), which has been known to alter the latitudinal position of the jet stream (Miller 1972; Ropelewski and Halpert 1986; Smith et al. 1998; Nunn and DeGaetano 2004), thus influencing synoptic weather patterns and the likelihood of widespread tornadic activity (Schaefer 1986; Johns and Doswell III 1992). Earlier attempts to constrain this ENSO-CONUS tornado relationship yielded varying con-

---

* Reprinted with permission from "Southeastern U.S. Tornado Outbreak Likelihood Using Daily Climate Indices" by M. C. Brown and Nowotarski, C. J., 2020. *J. Climate*, **33**(8), 3229-3252., ©2020 by American Meteorological Society.

clusions. Several such studies initially cast doubt on whether ENSO phase has any significant impact on the frequency (Schaefer and Tatom 1999; Marzban and Schaefer 2001) or strength (Agee and Zurn-Birkhimer 1998; Schaefer and Tatom 1999) of tornadic activity. Knowles and Pielke (2005) noted increases in the prevalence of strong tornadoes and "large number outbreaks"corresponding to La Niña conditions (i.e., the cool phase of ENSO). Cook and Schaefer (2008) asserted that winters with neutral ENSO conditions in tropical Pacific SSTs were associated with larger and more frequent tornado outbreaks, particularly in contrast with El Niño (warm phase) conditions. These and other related studies (e.g. Bove 1998, Sankovich et al. 2004) were somewhat limited, however. Examples include large variability and the presence of non-meteorological biases within the tornado report database, and limited sample size – both in relation to tornadoes themselves, and methodological characterization of tornado/outbreak days – potentially limiting the robustness of these results.

More recent papers have sufficiently addressed these limitations and provided more agreement on this subject. Allen et al. (2015) identified robust increases in tornado and hail reports across portions of the Central Plains and Southeast in association with La Niña conditions, and noted a latitudinal shift in these reports in response to mean seasonal positioning of the jet stream, surface cyclogenesis, and its associated instability axes. Furthermore, this study demonstrated that the influence of ENSO on CONUS severe convection extends well into spring months, in contrast to much of the earlier literature which suggested that any potential ENSO impacts would be isolated to winter months. Cook et al. (2017) came to similar conclusions regarding the favorability of La Niña conditions for severe convection, but instead through the lens of tornado outbreaks. The most recent additions to the literature have further contextualized this relationship by considering ENSO interactions with other parts of the climate system and in terms of its intrinsic variability. Molina et al. (2018) considered the interplay between ENSO and Gulf of Mexico (GOM) SSTs – a key source of moist instability associated with increased hail and tornado counts across portions of the US during both the warm season (Molina et al. 2016; Jung and Kirtman 2016) and cool season (Thompson et al. 1994; Edwards and Weiss 1996). In particular, this study found that both the frequency and location of significant tornadoes (EF2+ on the enhanced Fujita scale) vary by ENSO phase and strength, and warm GOM SSTs can enhance tornado probabilities even in ENSO-neutral phases. Molina and Allen (2019) further solidified this GOM influence by performing trajectory analysis of parcels participating in tornadic storms and finding that the GOM accounts for over half of attendant moisture contributions in both spring and winter, though the exact origin and length of these trajectories exhibit some seasonal dependence. Lastly, Allen et al. (2018) found that variations in ENSO intensity influence the seasonal peak and temporal onset on CONUS tornadoes.

Other studies have turned to different global patterns to explain variability in CONUS tornadic activity. Lee et al. (2013) found that warm tropical Pacific SSTs which develop during the transition between dominant ENSO phases (Trans Niño) are more conducive to spring tornado outbreaks, though the authors themselves note that the weak statistical strength of this relationship. Both Thompson and Roundy (2013) and Barrett and Gensini (2013) suggested that certain phases of the Madden-Julian Oscillation (MJO) modulate large-scale circulations in ways that favor or impede tornadogenesis during the spring, though the phases they deem favorable vary depending on the month chosen for analysis. Tippett (2018) agreed that tornado likelihood seems to vary by MJO phase, but also noted that the exact connection is sensitive to how one defines their MJO and tornado day metrics. Munoz and Enfield (2011) related the negative Pacific-North American (PNA) phase to a strengthening of the intra-Americas low-level jet, which subsequently enhances moisture flux into the Mississippi and Ohio River basins. Elsner et al. (2016) tangentially noted a decrease in tornadic activity across the Southeast during the positive North Atlantic Oscillation (NAO) phase. Lastly, some recent studies (Trapp and Hoogewind 2018; Childs et al. 2018) have suggested that Arctic conditions may influence the frequency of CONUS tornadoes via modifications of North American jet stream patterns, albeit in opposite seasons – July for the former study, winter the latter.

Though these studies have provided valuable insights regarding global-scale influence on severe weather variability, the methodology adopted often limits the applicability of their results. While several of the papers mentioned above have begun to investigate cool season tornadoes, the focus of this literature remains skewed towards warm-season storm environments and their associated tornadoes. Though the warm season coincides with a peak in tornadic activity across much of the CONUS, a secondary peak in the winter months has been documented within the southeastern US (Fike 1993; Guyer et al. 2006). Many of these cool-season storms form in environments that deviate substantially from the prototypical high-shear, high-CAPE storm environment (Guyer and Dean 2010; Sherburn and Parker 2014; Sherburn et al. 2016). These high-shear, *low*-CAPE (HSLC) storms are inherently more difficult to predict (Dean and Schneider 2008; Dean and Schneider 2012; Anderson-Frey et al. 2019). Hence, studies addressing Southeast US cool season tornadoes are valuable for increasing our physical understanding of these atypical storms. Furthermore, several teleconnection patterns and their subsequent environmental responses exhibit substantial seasonal and intraseasonal variability (e.g., Barnston and Livezey 1987; Thompson and Edwards 2000, and more recently, Gensini and Marinaro 2016, Allen et al. 2018, Molina et al. 2018). Thus, studies focused solely on warm-season months – or interpreting cool-season results through the lens of warm-season teleconnections – may fail to capture physically relevant patterns inherent to the cool season. The same can be said in terms of geographical location, in that a teleconnection phase relevant to Great Plains tornadoes may not be important for Southeast tornadoes, and vice versa, as evidenced by geographical variability in the findings of several of the studies discussed thus far. This study will attempt to address these concerns by considering teleconnections and their possible association with Southeast tornadoes across multiple seasons.

Second, several of the aforementioned studies conflate weak and significant tornadoes when analyzing storm environment in order to alleviate issues stemming from limited sample size, but proximity sounding studies have shown that the near-storm environments which spawn weak tornadoes (EF0 and EF1) bear greater semblance to nontornadic storm environments (Thompson et al. 2003). Therefore, our analyses will focus on the storm characteristics as they relate to outbreaks of significant tornadoes (EF2 and higher) as defined by the Storm Prediction Center (SPC). With these factors taken into consideration, the following research questions will be addressed:

1. On what timescale(s) and during which seasons do global teleconnection patterns most

distinctly correspond with tornado outbreaks in the southeastern US?

2. How are the storms coincident with these patterns temporally and spatially distributed, and do these distributions differ from climatological averages?

3. How do regional atmospheric conditions evolve during these outbreak patterns, and how are they physically linked with the teleconnections themselves?

2.2 Data and methods

2.2.1 Teleconnection data and indices

In light of previous research, a number of daily teleconnection indices were chosen to represent variations of large-scale environmental features (e.g., the polar front jet, Pacific SSTs, etc.). Daily indices for the Arctic Oscillation (AO), NAO, PNA, Eastern Pacific Oscillation (EPO), and Western Pacific Oscillation (WPO) were obtained from the Climate Prediction Center (CPC 2012; data available at ftp://ftp.cpc.ncep.noaa.gov/cwlinks/) and Earth System Research Laboratory (ESRL: Physical Sciences Division 2019; data available at https://www.esrl.noaa.gov/psd/forecasts/reforecast2/teleconn/). Daily Gulf of Mexico (GOM) SST anomalies are taken from the NOAA OI SST V2 High Resolution analysis (Reynolds et al. 2007) and averaged over the Full GOM domain established by Molina et al. (2016). These SST anomalies were then detrended using least squares regression, since clustering techniques tend to group together recent SST anomalies due to the warming trend in the dataset (Molina et al. 2016). Both the raw and detrended SST anomalies (herein referred to as SSTA and SSTAD, respectively) are analyzed for completeness. Since this SST record only extends back to September 1981, all of the chosen teleconnection patterns are only considered from 1982 - 2017 for consistency.

2.2.2 Storm report data

In order to categorize severe convective activity, storm report data were obtained from the SPC SVRGIS database (Schaefer and Edwards 1999), comprised of tornado, hail, and thunderstorm wind reports from within the prescribed southeastern US domain (Fig. 2.1a) for the years 1982-2017.

The reports were filtered following the methodology of Edwards (2010) to remove those reports potentially influenced by tropical cyclones, for which their associated near-storm environment is largely controlled by the tropical cyclone itself rather than large-scale atmospheric conditions. Several limitations and biases pervade the observational records of storm events, including the increase in reports due to improved technology, new reporting policies, and increased population (e.g. Verbout et al. 2006, Doswell III et al. 2009; Brooks et al. 2014). To mitigate these problems, a similar approach to previous teleconnection studies was adopted in which reports are consolidated into storm days. For the purposes of this study, any day (12Z - 12Z) with 5+ wind or hail reports or at least 1+ tornado report within the study domain is categorized as a severe convective (SC) day. Other SC day thresholds were tested, but the chosen definition proved most successful in removing false positive days (i.e. SC days flagged due to a few isolated wind and/or hail reports) while still retaining days where large, spatially and temporally coherent groupings of severe reports occurred. In addition to this SC day definition, days with no tornadoes are considered nontornadic (NT), days with tornadoes of only F/EF 0 or 1 are considered weakly tornadic (WT), and days with 1-5 tornadoes of F/EF 2 and above are considered significantly tornadic (ST), and days with 6 or more tornadoes of F/EF 2 and above were considered outbreak days (OB; akin to the violent tornado days, or VTDs, in Thompson and Roundy 2013). Given these categorizations, with the assumption that temporal trends in reporting biases are similar for all hazard types, the biases and trends discussed above should not significantly affect our conclusions.

2.2.3 Self-organizing map (SOM) clustering algorithm

Daily teleconnection indices were gathered at varying lead times of 3 days, 1 week, 2 weeks, 1 month, and 2 months prior to each SC day – chosen somewhat arbitrarily, but with the intent of covering the spectrum of potentially relevant temporal scales of teleconnection influence. These time series were then clustered using self-organizing maps (SOMs), via the SOM Matlab Toolbox (Vesanto et al. 2000). This statistical technique (Kohonen 1995), is essentially a non-linear principal component analysis, and has been used in recent studies (e.g., Nowotarski and Jensen 2013;

Anderson-Frey et al. 2017; Nowotarski and Jones 2018) to objectively classify high dimensional meteorological data. This technique clusters input data into characteristic nodes, using a grouping function that preserves the topology of the data. The data (in this case, SC days) grouped into each node can consequently be used to identify prominent modes of teleconnection variability and examine how they lead to different storm characteristics, as opposed to averaging or correlation techniques that might obscure multiple patterns leading to tornadoes or outbreaks.

A 3×3 SOM was created for all seven teleconnection indices (AO, NAO, PNA, EPO, WPO, SSTA, SSTAD) at each of the five tested lead times across four seasonal periods following the meteorological season convention | March/April/May (MAM), June/July/August (JJA), September/October/November (SON) | and December/January/February (DJF), for a total of 140 different SOM configurations. Five additional SOM dimensions were also tested in order to assess the sensitivity of the results to the SOM geometry. Though these additional SOMs will not be shown explicitly, their results are discussed later to gauge the robustness of the identified patterns. One sample SOM output (in this case, AO at a lead time of 60 days, during MAM) is shown for reference in Appendix Figure B.1. After the SOMs were created, the percentages of nontornadic (NT), weakly tornadic (WT), significantly tornadic (ST), and outbreak (OB) days matching each node were computed. The statistical significance of each of these percentages relative to seasonal averages (from 1982-2017) is tested, taking into account both the percentage of matches and the size of the SOM node (i.e., the number of days grouped into a node). The z-statistic is calculated following Barrett and Gensini (2013):

$$z = \frac{p_{node} - p_{climo}}{\sqrt{\frac{p_{node}(1-p_{node})}{n_{node}}}}, \tag{2.1}$$

where p_{node} is the storm type percentage within a given node, p_{climo} is the climatological percentage for that storm type, and n_{node} is the number of days grouped into the analyzed node. Student's t tests are performed using this z-score with 95% confidence threshold to determine whether the nodal percentages significantly exceed climatology. This alone, however, is not sufficient to determine whether a nodal pattern is a unique predictor for a given storm type. Even if a given storm type percentage is statistically significant, if the node contains a small number of those storm events compared to seasonal totals, it has limited value as a predictor. Thus, a second threshold is applied to isolate only the nodes which account for an above average ($> 100\%/9$ nodes $\approx 11.11\%$) fraction of a given type of storm event. Null patterns, defined as patterns whose storm type percentages are significantly lower than climatology and contain an above average fraction of their null event type(s), were also considered in order to assess pattern uniqueness. For NT and OB days, null events are defined as all other event types, whereas the null for WT is NT and the null of ST is both NT and WT. Subsequent analyses will focus primarily on the nodes and null nodes which pass both of the outlined criteria.

Nodal kernel density estimations (KDEs) of diurnal and seasonal storm report time and location are created for each seasonal period, as well as each of the selected nodes. This methodology mirrors recent literature (i.e. Anderson-Frey et al. 2016; Anderson-Frey et al. 2019) which has opted for KDEs over traditional two-dimensional binning or histogram approaches, as they provide smoother transitions between densities and avoid potential sensitivities to bin design. Each data point is replaced by a Gaussian kernel, and an optimization method is applied to seasonal climatology to determine the appropriate bandwidths (shown in Table 2.1) for each season, and these are subsequently applied to their associated nodes. These climatological and nodal distributions are then overlaid in order to diagnose potential spatiotemporal shifts associated with each node. Composite anomalies of regional conditions during several patterns are developed using data from National Centers for Environmental Prediction (NCEP) North American Regional Reanalysis (NARR; Mesinger et al. 2006). The variables chosen for analysis match those selected in related literature, including 250-, 500-, and 850-mb winds; 500-mb geopotential heights; 10-m winds; deep-layer shear (10 m - 500 mb); low-level shear (10 m - 850 mb); 2-m temperature and dewpoint, and surface pressure; as well as CAPE, SRH, and LCL. These anomalies are computed relative to SC day seasonal climatology for each analyzed time step (i.e. 12Z anomaly from 12Z climatology), allowing us to identify synoptic patterns specifically related to outbreak days, while also limiting the effect of diurnal variability. Additionally, we will diagnose HSLC conditions by comparing regional CAPE and shear values to the HSLC metrics presented in Sherburn and Parker (2014), with surface-based CAPE (SBCAPE) values ≤ 500 J kg^{-1} and deep-layer shear (used as proxy for 0-6 bulk shear) values > 18 m s^{-1} corresponding to HSLC conditions.

2.3 Results

From 1982-2017 in the prescribed domain, there were 4141 SC days. Figure 2.1b shows the type breakdown of these days for the entire period and each season, both by percentage and number. The largest number of ST and OB days take place in MAM, as expected, but both the SON and DJF percentages of ST and OB days are higher than those of MAM. This indicates that though SC days are less likely in the fall and winter, when they do occur they are more likely to be ST or OB days. This extension of ST and OB days into fall and winter months beyond the peak of the Midwest/Great Plains US tornado season is consistent with previous tornado climatology studies (e.g., Thompson et al. 2012, Smith et al. 2012). Lastly, both the number and percentage of ST and OB events in JJA are distinctly lower than those of all other seasons, for which reason we will exclude JJA results from the following discussion.

2.3.1 SOM output

Figure 2.2 shows the MAM outbreak SOM results. Outbreak and associated null patterns are gathered across all lead times for each teleconnection, and shown in red and blue, respectively. For all presented patterns, the line thickness corresponds to the extent to which the node's OB percentage exceeds its seasonal average (referred to as OB %), and opacity corresponds to the percentage of OB days grouped into that node (referred to as total %). The average teleconnection patterns preceding all SC days in a given season are shown for reference (in dotted purple), with ±1 standard deviation shaded in gray.These MAM percentages are provided in Table 2.2 for reference. Herein, patterns will be identified by their teleconnection and lead time (i.e. AO60).

During MAM months, eight significant OB patterns (red lines in Fig. 2.2) were identified across six teleconnections. For the AO (Fig. 2.2a), there is a 60 day pattern of sustained large, positive indices. For the NAO (Fig. 2.2b), there are two patterns - one at a lead time of 30 days showing a transition from weak positive to sustained negative values. The second NAO pattern is consistent with this, showing sustained negative indices seven days out from the SC day. Both the NAO7 and NAO30 patterns differ from the identified null patterns, which show positive NAO values up through the SC day. The PNA teleconnection (Fig. 2.2c) shows one pattern consisting of prolonged, moderately negative indices for 60 days. The EPO (Fig. 2.2d) displays an oscillatory OB pattern, shifting between positive and near-zero values over a span of 14 days. However, similar patterns (albeit with lower magnitude values) were identified as null nodes, so the uniqueness of EPO14 is debatable. For the WPO (Fig. 2.2e), there is one OB pattern showing weakly negative values for a period of seven days. This is contrasted by two null patterns, which contain positive values during that time frame. No OB patterns exist for SSTA (Fig. 2.2f), but there are several null patterns displaying prolonged negative anomalies. Lastly for SSTAD (Fig. 2.2g), there are two OB patterns – one oscillating between negative and positive values across a 60 day period, and a second showing slightly negative anomalies increasing towards zero seven days prior to the SC day. The null nodes for SSTAD show generally decreasing trends, though the magnitudes of these anomalies vary. As with the EPO, the overlap between the SSTAD OB patterns and these null patterns challenge the usefulness of said OB patterns.

SON nodal output (Fig. 2.3) shows five OB patterns across four teleconnections, with associated OB percentages provided in Table 2.3. The NAO displays two OB patterns (Fig. 2.3b) - one lasting 60 days consisting of slightly to moderately negative values, increasing to slightly positive values up through the SC day, and a second with this same pattern but spanning only 30 days. The 60 day NAO null node mirrors these OB patterns, but the others show some overlap. For the WPO (Fig. 2.3e), there is one OB pattern lasting 60 days, showing initially neutral values increasing gradually from roughly 60-20 days out, before decreasing for the remainder of the period. The WPO null nodes generally contrast this OB pattern except during the two weeks prior to the SC day, where there is substantial overlap. Both SSTA and SSTAD SOM outputs (Fig. 2.3f,g, respectively) contain an OB pattern consisting of strongly negative anomalies three days prior to the SC day.

The null nodes for both indices contain mostly neutral to positive anomalies at varying timescales, except for one node which bears semblance to the OB pattern.

There are 6 OB nodes spanning five teleconnections during the DJF period, as shown in Figure 2.4, with associated OB percentages provided in Table 2.4. For the AO (Fig. 2.4a), there exists an OB pattern at a lead time of 30 days, containing strongly positive values which steadily decline to neutral values. A second, 14 day OB pattern shows somewhat consistent results, oscillating between neutral and weak positive indices up through the SC day. The AO null nodes show indices decreasing from neutral values to strongly negative values. The NAO (Fig. 2.4b) displays one OB pattern of sustained positive values during the 30 days preceding the SC day. Though the null nodes show varying magnitudes, they all consistently display lower values than the OB pattern. For the PNA pattern (Fig. 2.4c), the single OB pattern shows positive indices decreasing to neutral values over 14 days. There is some overlap between PNA null patterns and this OB pattern, though none of the null nodes show the same shape and magnitude of said pattern. SSTA output (Fig. 2.4f) shows one OB pattern with mostly neutral anomalies for a period of 30 days, while SSTAD (Fig. 2.4g) has a 14 day OB pattern showing an increase from weakly negative to weakly positive anomalies. The null nodes for both SSTA and SSTAD mostly exhibit sustained negative anomalies on their respective timescales.

2.3.2 Temporal report distributions

Next we examine how the storm reports associated with the significant OB nodes are temporally distributed. Figure 2.5 shows the climatological and nodal distributions of these reports, as well as the OB and total percentages for each pattern. MAM climatology (light/dark gray shading in all panels of Fig. 2.5 with associated OB % of 2.93%) shows storm reports throughout the entire season, with the highest densities spanning April and May. The diurnal range of these report densities spans 18Z to 03Z (19Z to 02Z at the 90th percentile). The majority of the MAM OB nodes resemble climatology, particularly at the 90th percentile, but all seven nodes exhibit some diurnal broadening at various points in the MAM period. NAO7 (Fig. 2.5b) shows the most prominent broadening, with a pronounced extension of reports towards 09Z in late May. In terms of seasonal skew, NAO7 is the only pattern showing a discernible shift in report densities towards later in the MAM period, while AO60 (Fig. 2.5a) shows a shift towards earlier dates.

The SON climatology (with associated OB % of 3.13%) shows report densities largely confined to mid-October and November. The diurnal range for the October grouping spans 18Z to 6Z (19Z to 00Z at the 90th percentile), and then broadens to 15Z to the following 11Z (18Z to 05Z at the 90th percentile) during November. NAO30 and NAO60 (Fig. 2.6a-b, respectively) lack the mid-October grouping, and instead show some high report densities in early September and October. That said, all of the SON OB nodes display a primary grouping in the latter half of November, coincident with prominent diurnal broadening. This broadening extends across nearly the entire SC day for several of the nodes, which may suggest the prevalence of nocturnal storms which persist into the following day.

Lastly, the DJF climatology (light/dark gray shading in all panels of Fig. 2.7 with associated OB % of 4.57%) has a pyramid-like structure with a small grouping of reports in late December showing a tight diurnal range, which broadens with time into late February. By late February, report densities span nearly the entire SC day, though the highest densities remain between 18Z and 06Z. The DJF OB nodes exhibit the most nodal variance of the analyzed seasons. AO30, PNA14, and SSTAD14 (Fig. 2.7b,d, and f, respectively) all resemble climatology, though the latter two show an extension towards later hours. AO14 and SSTA30 (Fig. 2.7a,e, respectively) show some skew towards the latter half of January along with diurnal broadening (most prominently in AO14). NAO30 (Fig. 2.7c) shows a unique pattern, with two secondary groupings in late December and early January showing broad diurnal ranges, and a primary grouping in late February which spans the entire SC day.

2.3.3 Spatial report distributions

Next we consider the spatial characteristics of the identified OB nodes. Figure 2.8 shows the MAM spatial distribution of both climatology and the OB nodes (with the same color scheme as

Fig. 2.5-2.7). MAM climatology shows report densities stretching across most of the northern extent of the study domain, with the highest densities located across Arkansas, northern Louisiana and Mississippi, along with a small grouping across eastern Tennessee and northern Georgia. The MAM OB nodes are essentially identical to climatology at the 70th percentile, perhaps due to increased sample size. The higher report density contours exhibit more variability, with NAO7 and WPO7 (Fig. 2.8b,f, respectively) favoring the east and west portions of the domain, respectively, but still largely resemble climatological locations.

SON spatial climatology, shown in Figure 2.9 bears semblance to MAM climatology, but its 70th percentile extends southeastward towards the Louisiana Gulf Coast. WPO60 (Fig. 2.9c) matches this climatology all but perfectly, and NAO30 (Fig. 2.9a) differs only in that its 90th percentile extends into the eastern portion of the domain. The remaining three nodes (Fig. 2.9b,d-e, respectively) are not dissimilar from climatology, but all display an extension of their highest report densities towards the Louisiana coast.

Figure 2.10 shows the DJF spatial climatology, which is positioned further southward of the other seasonal climatologies, with its highest densities centered on Mississippi and extending slightly east and west into its neighboring states. All DJF OB nodes except AO30 show their 90th percentile contours extending northward relative to climatology across Arkansas, and also into western Tennessee for NAO30 and SSTA30 (Fig. 2.10c,e, respectively). In terms of east-west placement, AO14 (Fig. 2.10a) has the western most skew of the OB nodes, while AO30 (Fig. 2.10b) is the only node displaying report densities as far east as Georgia and down into the Florida Panhandle.

2.3.4 Discussion

In the final section of this paper, we examine the environmental conditions associated with the OB teleconnection patterns identified in order to provide a general physical justification for each pattern. These analyses will focus on the most unique and robust patterns. In order to make this determination, we will compare the OB patterns with current literature, as well as consider the consistency of these patterns across all tested SOM dimensions.

Beginning with the MAM OB patterns, the NAO results fit within the context of Elsner et al. (2016) with OB patterns showing sustained negative NAO indices directly preceding the SC day, and null OB patterns showing opposite patterns. These same OB and null patterns were present, in some form, in every one of the SOM geometries tested, further solidifying their significance. The Elsner study hypothesized that a positive NAO and its associated North Atlantic subtropical high would decrease Southeast tornado likelihood, so conversely a negative NAO could increase tornado likelihood due to a weaker subtropical high and lower pressure across the Southeast. However, since this has not been shown explicitly, we will further examine the NAO30 pattern and its positive to negative NAO transition, thus bridging the gap between the Elsner study and our own. PNA60 agrees with the conclusions of Munoz and Enfield (2011), and its prolonged negative PNA values – typically associated with La Nina events – also lends support to Allen et al. (2015) and Cook et al. (2017). Though addressing different teleconnection patterns, these studies relate their findings to a shift in the jet stream and cyclone track, which through various physical processes favor deep convection and increase tornado likelihood across the central and southeastern US. Given the thoroughness of these previous analyses, we will not explicitly examine PNA60 in our study. EPO14, SSTAD7, and SSTAD60 all show substantial overlap with their associated null nodes, which could suggest that they are not uniquely associated with outbreaks. Furthermore, these patterns do not appear in the majority of the other SOM geometries. Despite analyzing different seasons, the lack of a clear SSTAD signal aligns well with Molina et al. (2018) in that GOM SST anomalies can provide thermodynamic support, but additional tropical-extratropical interaction might be necessary for corresponding convection to form. WPO7 is consistent with its null cases, but several of the other tested SOM dimensions either omit or conflict with this pattern. This leaves AO60, which appears in nearly all tested SOM dimensions and therefore will be chosen for further investigation.

The selection of SON OB nodes is much less clear cut, as all of the identified patterns show varying levels of overlap with their associated null patterns. The transition to slightly positive or near-neutral shown in both NAO patterns would not seem distinctly favorable for tornadic activity in the context of both the Elsner study and our MAM results. That said, similar NAO patterns appear as predictors of both ST (Appendix Fig. B.2) and OB days in every tested SOM dimension. We will further analyze NAO60 given its higher OB percentages. Patterns similar to WPO60 appear in several of the other examined SOM geometries, but these patterns show even more overlap with null cases. The strongly negative values in both SSTA3 and SSTAD3 disagree with previous literature – namely EEdwards and Weiss (1996) and Thompson et al. (1994) – and seem counterintuitive given our current understanding of Gulf of Mexico influence of CONUS severe convective activity. These cold anomalies are thought to limit the inland transport of low-level moisture and instability across the Southeast, thus inhibiting thunderstorm activity. Despite this contradiction, patterns resembling SSTA3 and SSTAD3 show up in every tested SOM configuration, so the regional conditions associated with these patterns warrant additional investigation. Though SSTA3 also contains a high OB percentage, we will further analyze SSTAD3, since this quantity has been utilized in several recent GOM SST severe studies (e.g., Molina et al. 2016; Jung and Kirtman 2016, Molina et al. 2018).

Of the DJF OB nodes, the most inconclusive are PNA14 and SSTA30. The former shows some overlap with its null nodes, while the latter is neither consistent with nor opposed to the existing literature, and neither pattern appears in the majority of the tested SOM geometries. Perhaps the net neutral values in SSTA30 indicate that its associated storms bear weak relation to GOM SSTs. SSTAD14, however, is consistent with Edwards and Weiss (1996) in that a positive trend in GOM SSTs is related to an increase in Southeast severe convection, though we are dealing with SST anomalies and outbreaks. Similar patterns show up in both SSTA and SSTAD OB plots in several of the other analyzed SOM configurations. AO14 and AO30 echo the findings of Childs et al. (2018) that the AO is relevant to cold season tornadoes, though the Childs et al. study cites the positive AO phase as being supportive of tornadic activity. This phase supports warm, moist Southeast conditions due to an enhanced polar jet which confines continental polar air to northern latitudes. Though this signal can be seen in the DJF ST patterns (Appendix Fig. B.3), the OB patterns instead show a decrease from positive values. In terms of SOM dimension, half of the tested SOM maps show the AO14 pattern, while the other half show the AO30 pattern. We will examine the AO30 node further given its initially large, positive AO values in order to provide additional comparison with the Childs study. Lastly, NAO30 directly contrasts the findings of the aforementioned Elsner study, which along with agreement between NAO30 and its null patterns, leads us to further analyze this pattern.

More generally with these OB patterns, we see that AO and NAO are most consistently related to OB days across the analyzed seasons, with SSTA and SSTAD also showing up frequently. Interestingly, both of the Pacific patterns (EPO and WPO) show very limited utility in distinguishing OB days, despite ample literature relating other Pacific-related patterns (namely ENSO) to CONUS tornado frequency. The closest such relationship we are able to discern comes from the PNA pattern, which is indirectly correlated with El Nino phases. This is not to draw into question Pacific influences on CONUS tornadoes, though it might suggest that EPO and WPO are less useful predictors compared to ENSO. Lastly in regards to temporal scales, we see that AO and NAO are more often related to Southeast OB days at longer time scales of 30 or 60 days, while the influence of SSTA/SSTAD is most pronounced on a shorter time scale of 3 days. These differences are likely explained by both the varying temporal scales of these teleconnections and the proximity of their primary driver (i.e., the Arctic and North Atlantic, as opposed to the Gulf of Mexico) to the study domain.

2.3.5 Environmental characteristics

2.3.5.1 MAM

Since the identified OB patterns are either unvarying or bimodal (e.g., values transitioning from positive to negative), we examine the 00Z anomalies (from 00Z averages) only during relevant periods. For sustained patterns like MAM AO60, this average is computed over the entire period in question, while for bimodal patterns such as MAM NAO30 we examine the conditions during the two dominant phases to highlight potential differences. The 00Z step was chosen as it is the closest available time to the mean event times shown in presented temporal density plots (c.f. Fig. 2.5-2.7). All time steps were analyzed to diagnose possible diurnal variation, but this variation was found to be negligible. It bears reiterating that the presented anomalies are relative to severe convective climatology in a given season. We know a priori that severe convection exists on these days, so our intent is to key on the factors which specifically favor widespread tornado development.

Starting with the MAM OB patterns, the sustained positive values shown in AO60 are consistent with an intensified polar vortex and zonal polar front jet across northern latitudes. This pattern inhibits the intrusion of continental polar air into southern latitudes, allowing for above average geopotential heights across the southern CONUS. This is evidenced by 250 mb patterns in Figure 2.11a, showing negative speed anomalies and easterly mean vector anomalies across Mexico and GOM, and positive anomalies and westerly vector anomalies across central and northern CONUS (very similar to Fig. 3b in Allen et al. 2015). Moreover, the southeastern region is located in the right-entrance region of the mean 250-mb jet streak, conducive to synoptic-scale ascent and destabilization. These patterns are corroborated by 500 mb (Fig. 2.11b) and surface patterns (Fig. 2.11c) showing positive geopotential height and surface pressure anomalies across the Southeast. This pattern extends down through the depth of the atmosphere, with mostly southerly anomaly winds and positive speed anomalies at the 850 mb and 10 m levels throughout much of the period (not shown). In addition to these spatial anomalies, it is also worth considering the temporal trends in variables pertinent to the regional storm environment. As such, Figures 2.12 and 2.13 show domain-averaged quantities at 00Z for the duration of each OB pattern, as well as climatological times series for reference. Figure 2.12 shows 2 m temperature and dewpoint, as well as approximate LCL height, while Figure 2.13 contains deep-layer shear, SBCAPE, and 0-3 km SRH during each analyzed OB pattern, along with climatological values and aforementioned HSLC criteria consistent with Sherburn and Parker (2014). Since these values are averaged across the study domain, and thus could conflate both convective and non-convective environments, they are not meant to convey the exact environmental state in which storms are developing. Rather, these values serve to represent general trends during the analyzed periods.

These pressure and circulation patterns would support increased low-level moist instability across the Southeast during this period. Though both temperature and dewpoint values remain largely below climatology (Fig. 2.12a-b, respectively), their respective trends support gradually increasing CAPE (Fig. 2.13b). Furthermore, these thermodynamic trends immediately prior to the SC day favor low LCLs - a key distinguishing factor between nontornadic and tornadic supercells (e.g. Rasmussen and Blanchard 1998; Thompson et al. 2003) that has been shown to impact the positioning and strengthening of near-surface circulation in supercell environments (Brown and Nowotarski 2019). This positive trend in CAPE places SC day values beyond the bounds of HSLC CAPE criteria. Concurrently, deep-layer shear values decrease in magnitude (Fig. 2.13a), but remain mostly above climatology (and the HSLC shear threshold), as do regional SRH values (Fig. 2.13c). Though the CAPE values remain close to climatological values, the sustained increases are likely significant given that numerous studies examining HSLC environments (e.g. Sherburn et al. 2016) have noted that HSLC events are typically associated with ample shear (as supported by Fig. 2.13a), and thus CAPE is the key limiting factor.

For NAO30, a shift from positive (t-30 to t-21 days from SC day) to negative values (t-10 to t-0 days from SC day) would indicate a transition from above average to below average geopotential heights across the eastern US (North Carolina Climate Office 2011), possibly causing a southward intrusion of Arctic air and displacement of the jet stream closer to the study domain. The latter is shown in Figure 2.14a-b, displaying negative speed anomalies and easterly mean vector anomalies across the Southeast, transitioning to positive speed anomalies and westerly anomaly winds. The 500-mb height anomalies shown in Figure 2.14c-d reflect this synoptic shift, with positive height anomalies and anticyclonic circulation transitioning to negative anomalies and cyclonic circulation with time, which in turn supports phasing of positive to negative surface pressure anomalies over the eastern US (Fig. 2.14e-f). As with AO60, thermodynamic trends for this pattern support increased CAPE (Fig. 2.12b) and decreasing LCLs (Fig. 2.13c), as well as increased shear (Fig. 2.12a). Both CAPE and shear fall outside their respective HSLC criteria, suggesting a more traditional storm environment with increased CAPE and shear.

2.3.5.2 SON

Regarding SON OB patterns, NAO60 displays a shift from negative (t-60 to t-21 days from SC day) to weakly positive values (t-20 to t-0 days from SC day), signaling a transition from below average to near or slightly above average geopotential heights across the eastern US. This pattern would be consistent with a slight northward lifting of Arctic air giving way to warmer conditions in its wake, which could also act to shift the jet stream northward. This generally holds true in these analyses, with initially positive speed anomalies and westerly anomaly winds at 250 mb, giving way to neutral anomalies and weak anticyclonic circulation (Appendix Fig. B.4a-b). At 500 mb (Appendix Fig. B.4c-d), negative height anomalies persist over most of the CONUS 60-21 days out from the SC day, but become neutral thereafter. Upper-level synoptic pattern changes drastically during this pattern, with the predominantly westerly flow across the southern US turning southwesterly with time. These upper-level patterns and associated anomalies are magnified several times over for SSTAD3 (Fig. 2.15a-b), with a jet streak extending from Texas up through the Northeast, along with an intense 500 mb Colorado low. Interestingly, this elongated jet streak is nearly identical to the jet-level pattern shown in Figure 6a from Sherburn and Parker (2014) as being associated with Southeast HSLC events. The 500-mb pattern offered in their Figure 6b also is similar to our Figure 2.15b, though the axis of their 500 mb trough is shifted further eastward.

Given these similarities, we would expect the SON patterns to exhibit HSLC conditions leading up to their SC days. Starting with NAO60, Figure 2.13d shows generally increasing shear values, though these values remain well below the HSLC shear threshold through the SC day. Thermodynamically, NAO60 shows steadily decreasing temperatures, (Fig. 2.12d), dewpoints (Fig. 2.12e) and CAPE values (Fig. 2.13e) for most of its duration, though these variables increase slightly immediately prior to the SC day. These CAPE values are both below SC climatology and within the bounds of the HSLC CAPE criteria, with average SC day values of 500 J kg^{-1}. For SSTAD3, domain-averaged shear values are noticeably higher, exceeding the HSLC shear threshold by the SC day (Fig. 2.13d). SSTAD3 resembles NAO60 in that its thermodynamic variables increase immediately before the SC day, but the magnitudes of these variables are uniformly lower, with only 300 J kg^{-1} of SC day CAPE. From these observations, we see that HSLC conditions appear to be invigorated in our SSTAD3 synoptic regime. The differences between NAO60 and SSTAD3 in terms of deep-layer shear are relatively straightforward; the upper-level flow of the latter (Fig. 2.14a-b) is noticeably stronger is association with prominent troughing over the central US. The more perplexing question, however, remains | what is limiting CAPE in this synoptic regime?

Examining the low-level characteristics of both NAO60 (Appendix Fig. B.4f,h) and SSTAD3 (Fig. 2.15c-d), we see that both exhibit mostly easterly anomaly winds and positive 10 m wind anomalies across the GOM in association with high pressure across the Carolinas. This forcing contributes to pronounced negative anomalies in both SSTA3 and SSTAD3 via mechanical mixing and overturning (such as in Appendix Fig. B.5). As to whether this influences Southeast CAPE values, near-surface air transported over these waters would be drier (and possibly cooler) relative to a typical Northern Gulf parcel, especially given that easterly parcel trajectories are likely originating from the nearby surface ridge. CAPE deficits increase in magnitude for the patterns exhibiting stronger surface ridging, supporting this argument.

Given the slower response time of overturning and subsequent inland transport, this mechanism would be most relevant under sustained flow regimes in which air parcels continuously originate from areas of enhanced mechanical mixing. However, a closer examination of low-level streamlines in both OB nodes suggest a transition to southerly surface transport immediately preceding the SC day, likely in response to approaching troughs and associated frontal boundaries. This shift away from areas of cold, overturned waters would support an influx of heat and moisture into the Southeast, as evidenced by increasing temperatures and dewpoints, and rapidly decreasing LCLs (Fig. 2.12d-f). All else held constant, these low-level thermodynamic adjustments would result in a large increases in surface-based CAPE, but the observed CAPE increases (Fig. 2.13e) still leave values well below SC climatology. Thus, there must be some secondary limiting factor aloft partially counteracting these surface influences. It is possible that the aforementioned surface ridging is associated with subsidence and mid-to-upper level warming, which would act to reduce regional CAPE values. Closer examination of the mid-to-upper troposphere (850 - 500 mb) temperature profiles (Appendix Fig. B.6) immediately prior the SC day reveals a warming trend throughout the depth of this layer, consistent with subsidence. To this end, the magnitude of this upper-level heating increases along with the strength of the coincident anticyclonic circulation. In spite of these upper-level trends, enhanced low-level shear (not shown) and SRH (Fig. 2.13f) in response to invigorated low-level flow, combined with lower LCLs related to shifting low-level trajectories (Fig. 2.12f) provide sufficient impetus for widespread severe convection, even with relatively reduced instability.

2.3.5.3 DJF

Lastly with DJF patterns, AO30 shows a steady decline from strongly positive to near-zero values, which should correspond to a gradual weakening of an initially strong, zonal polar front jet, allowing for a slight southward intrusion of Arctic air and a southward jet stream displacement. This progression is shown in the associated 250- and 500-mb fields with a jet streak expanding southwestward (albeit with variable speed anomalies), placing the domain broadly in its left entrance region (Appendix Fig. B.7a-b), along with a transition from positive to neutral 500-mb geopotential height anomalies (Appendix Fig. B.7c-d). These patterns support positive surface pressure anomalies which decrease in magnitude with time (Appendix Fig. B.7e-f). CAPE and shear trends are generally consistent with SC climatology (Fig. 2.13g-h), but climatology itself corresponds to HSLC conditions. Finally, NAO30 displays sustained positive NAO values, which correspond with prolonged above average geopotential heights over the eastern US, as demonstrated by anomalous anticyclonic circulation aloft and associated positive surface pressure anomalies (Appendix Fig. B.8). These patterns suppress shear across the Southeast, with values plummeting below average by the SC day (Fig. 2.13g), but result in above average CAPE values (Fig. 2.13h). The net effect of the synoptic regimes for both DJF OB patterns are decreased LCLs (Fig. 2.12i) and increased SRH (Fig. 2.13i), both of which favor the development of tornadoes.

2.4 Summary and conclusions

This study relates numerous climate indices to Southeast tornado outbreak likelihood across multiple seasons using a self-organizing map technique. Several of the identified outbreak patterns explicitly agree with or fit into the context of previous literature, particularly in spring months (MAM), while other patterns either differ from the literature or are altogether new. The physical implications of these patterns for tornado outbreak likelihood vary slightly by teleconnection, but are largely consistent with one another and with previous studies. Though the direct influence of these patterns is often dynamic – particularly the positioning and strength of the jet stream, and modulation of cyclone tracks – their ramifications are two-fold. Dynamically, these modulations provide synoptic ascent and a source of shear, while alteration of lower tropospheric flow patterns causes an influx of Gulf moist instability. For MAM teleconnections, the net result of these factors is a high-shear, high-CAPE Southeast setup reminiscent of a traditional Great Plains outbreak environment. For DJF teleconnections, similar increases in CAPE and shear exist, but HSLC conditions emerge as a result of the season. SON teleconnections are unique, however, in that their associated synoptic patterns actually contribute to HSLC conditions through a combination of processes both aloft and at the surface.

As with any study relating atmospheric characteristics across multiple spatiotemporal scales, there are some factors that must be considered. First, there are inherent limitations when focusing exclusively on tornado outbreaks, particularly smaller sample size and sensitivity of spatiotemporal distributions to individual reports. In our study, the former concern is largely addressed by our statistical significance testing. The latter might be partially offset by the fact that the frequency of severe reports on outbreak days exceeds that of non-outbreak SC days, but this could also mean that outbreak reports dominate such distributions.

One other matter is the temporal consistency of the identified OB patterns. In other words, if we see an OB pattern at a longer time scale, shouldn't this same pattern also show up on shorter time scales? Sometimes this is accurate, as with SON NAO30 and NAO60 (c.f. Fig. 2.3b), but this is not always the case. This could be a matter of statistical significance, as SOMs with smaller temporal scales could be overclassifying teleconnection patterns—such as trying to differentiate between varying magnitudes of positive AO values in MAM, when the most important characteristic is simply the existence of sustained positive values. This excessive sorting could compromise the statistical significance of these shorter patterns, even if their underlying physical meaning is valuable. Alternatively, the existence of longer OB patterns which do not manifest themselves on smaller time scales could underscore the importance of prolonged synoptic patterns for outbreak potential. For instance, extended periods of enhanced heat or moisture flux into a region (as with MAM AO60) or increased shear in response to jet placement (as with MAM NAO30) could prime the region, thus increasing the likelihood of widespread severe convective activity (and by extension, tornado outbreaks). This notion of synoptic priming has been offered up in different contexts, including fire weather (Papadopoulos et al. 2014), MJO convection (Katsumata et al. 2009) and convection initiation in the Southern Great Plains Frye and Mote 2010), so it is possible that a similar concept could apply to Southeast severe convection as well. Also temporally, the methodology employed allows for temporal covariance, in which consecutive SC days occurring within the same synoptic regime cause teleconnection patterns to count multiple times within the SOM analyses. Though not entirely unphysical, this could lend undue statistical significance to certain synoptic regimes, particularly for OB cases in which sample size is already limited.

Another key factor is the potential influence of seasonal and intraseasonal variability. Given the analyzed lead times, particularly 30 and 60 days, several of the presented OB patterns span much of their respective seasons, or extend into a separate season altogether. As such, there are associated trends in thermodynamic variables (e.g. temperature, dewpoint, CAPE, LCL) and some dynamic variables (e.g. deep-layer shear, given jet stream seasonality) that could contribute to the regional conditions presented. This is especially true for the time series shown in Figures 2.12-2.13 where, for instance, the gradual decrease in CAPE coinciding with SON NAO60 (blue line in Fig. 2.13) may be partially related to a progression towards winter months. Keeping with this example, however, the magnitude of these CAPE values relative to SC climatology for that particular season does tell us something unique about the conditions associated with that particular teleconnection pattern. Taking into account both the trend and magnitude of the analyzed variables is crucial to leverage these seasonal influences.

Further research is necessary to fully characterize the identified patterns and their contribution to Southeast tornado outbreak frequency. This includes investigating the environmental characteristics of the patterns not examined in the final section of discussion—specifically those consistent with previous literature for comparison with their findings, as well as patterns deemed nonunique due to overlap with null nodes in order to understand why their connection to outbreak potential is less distinct. Different classification or machine learning methodologies might also provide additional insight, as would extending the presented methodology to different regions, time periods, and climate indices. Furthermore, our SOM methodology could be modified to identify patterns of multidimensional data (as in Anderson-Frey et al. 2017) conducive to tornado outbreaks, with the teleconnection patterns corresponding to these patterns being determined subsequently. Other novel techniques, such as the spectral methods implemented in Childs et al. (2018), may prove skillful in separating out components of climate-scale, seasonal, and intraseasonal variability which superimpose themselves on the examined synoptic fields and potentially complicate these sorts of analyses.

In any case, the results presented here add to a growing body of literature on teleconnections between global-scale patterns and regional severe weather likelihood. In addition to the intrinsic value of better understanding the links between the largest and smallest scales, this work may also prove useful in forecasting applications, such that awareness of regional responses to global-scale patterns by local forecasters may improve the identification and forecast lead time of potential severe weather outbreaks.

Table 2.1: Optimized filtering bandwidths for x and y components of temporal (time of day and time of year, respectively) and spatial (longitude and latitude, respectively) KDEs. Reprinted from Brown and Nowotarski (2020), with permission from American Meteorological Society.

	Temporal (x)	**Temporal (y)**	**Spatial (x)**	**Spatial (y)**
MAM	1.063	3.367	0.751	0.252
SON	1.698	3.882	0.903	0.364
DJF	1.884	5.181	0.800	0.341

Table 2.2: Nodal percentage of OB days and percentage of total MAM OB days for each of the identified MAM OB nodes. Reprinted from Brown and Nowotarski (2020), with permission from American Meteorological Society.

MAM (OB% = 2.93%)	**% OB (nodal)**	**% of total OB days**
AO60	8.05	17.07
NAO14	6.78	19.51
NAO30	6.02	24.39
PNA60	7.03	21.95
EPO14	6.75	26.83
WPO7	5.91	29.27
SSTA14	5.67	26.83
SSTA60	6.18	26.83

Table 2.3: Same as Table 2.2, but for SON OB nodes. Reprinted from Brown and Nowotarski (2020), with permission from American Meteorological Society.

SON (OB% = 3.13%)	**% OB (nodal)**	**% of total OB days**
NAO30	9.09	35.29
NAO60	13.21	41.18
WPO60	8.86	41.18
SSTA3	18.18	21.95
SSTAD3	11.9	29.41

Table 2.4: Same as Table 2.2, but for DJF OB nodes. Reprinted from Brown and Nowotarski (2020), with permission from American Meteorological Society.

DJF (OB% = 4.57%)	**% OB (nodal)**	**% of total OB days**
AO14	12.7	36.36
AO30	13.21	31.82
NAO30	14.58	31.82
PNA14	11.11	31.82
SSTA30	13.64	27.27
SSTAD14	11.29	31.82

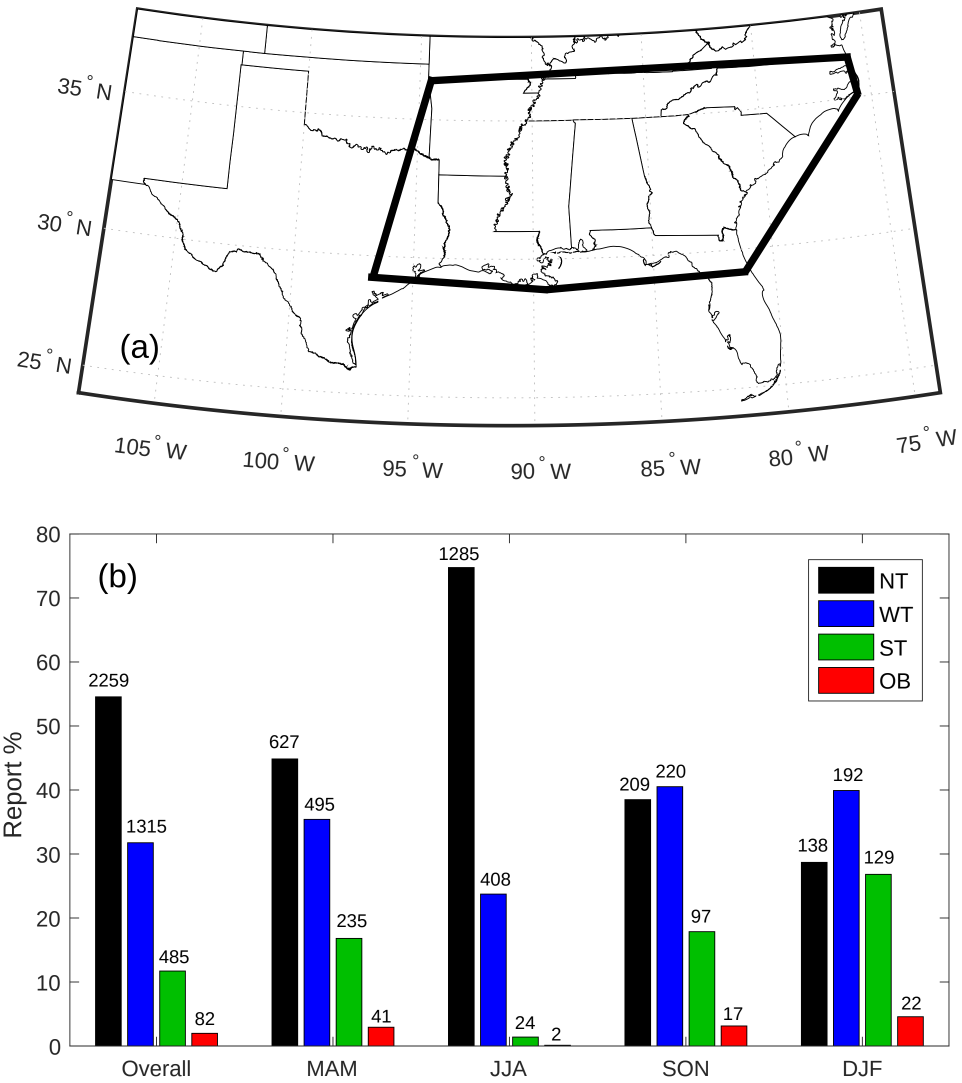

Figure 2.1: (a) Prescribed Southeast domain for analysis, and (b) barplot showing percentage and count of non-tornadic (NT), weakly tornadic (WT), significantly tornadic (ST), and outbreak days for the entire 1982-2017 analysis period, and broken down by season. Reprinted from Brown and Nowotarski (2020), with permission from American Meteorological Society.

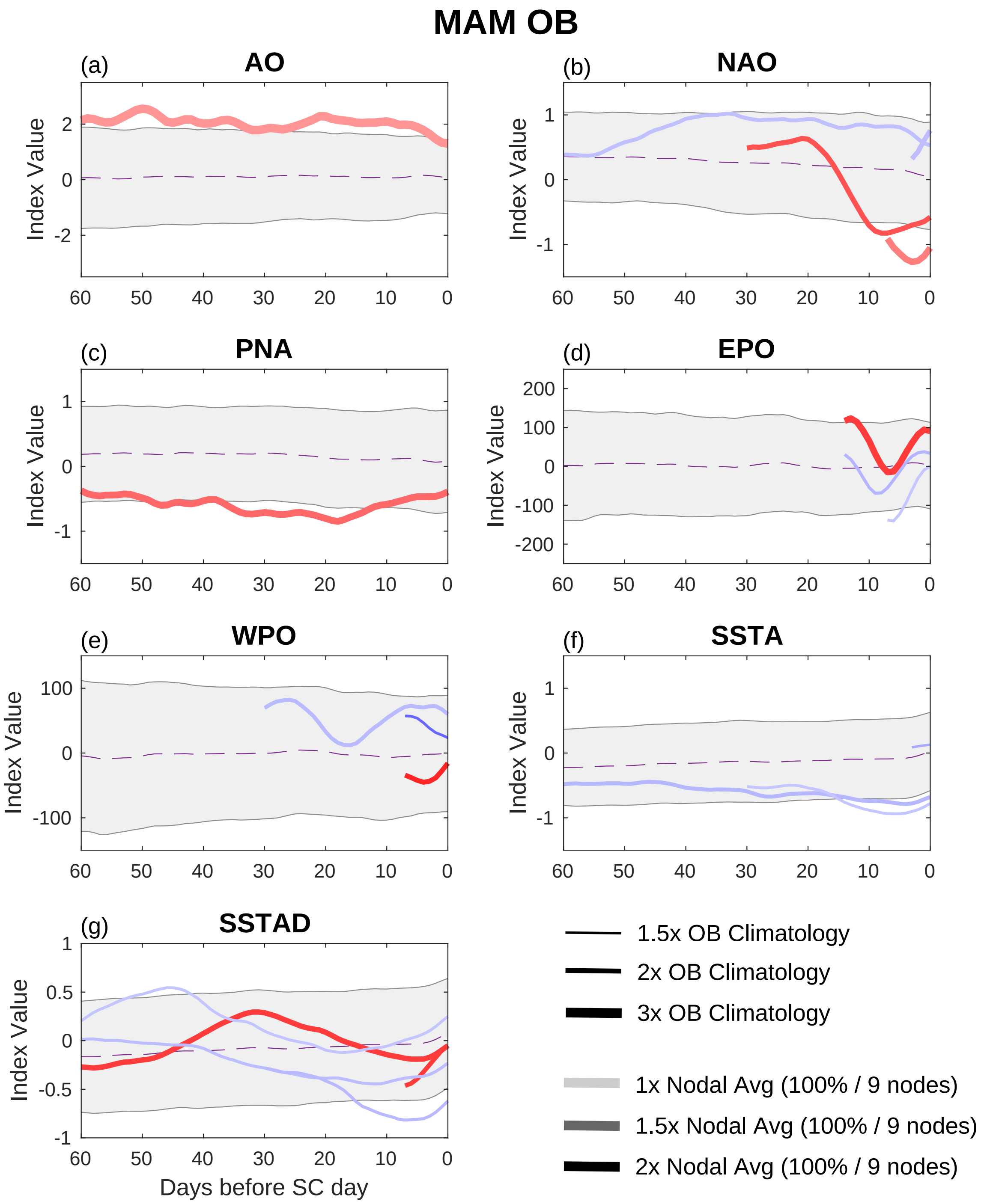

Figure 2.2: Outbreak node patterns (in red) and null patterns (in blue) associated with MAM period, with line thickness corresponding to deviation from climatology and line opacity corresponding to percentage of OB days grouped into each node; the average SC day pattern is shown in dotted purple, with associated error bounds in light gray. Reprinted from Brown and Nowotarski (2020), with permission from American Meteorological Society.

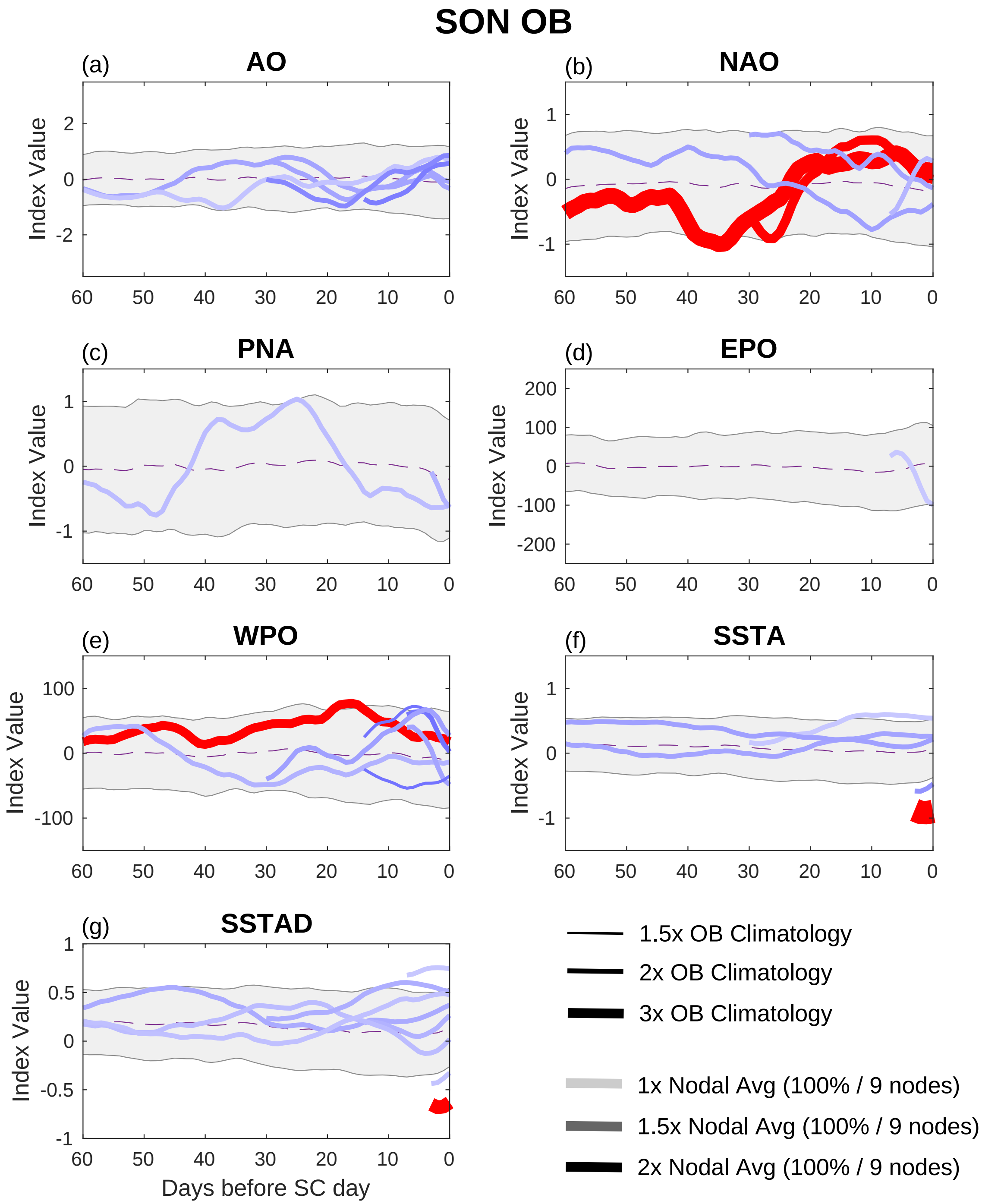

Figure 2.3: Same as Figure 2.2, but for SON period. Reprinted from Brown and Nowotarski (2020), with permission from American Meteorological Society.

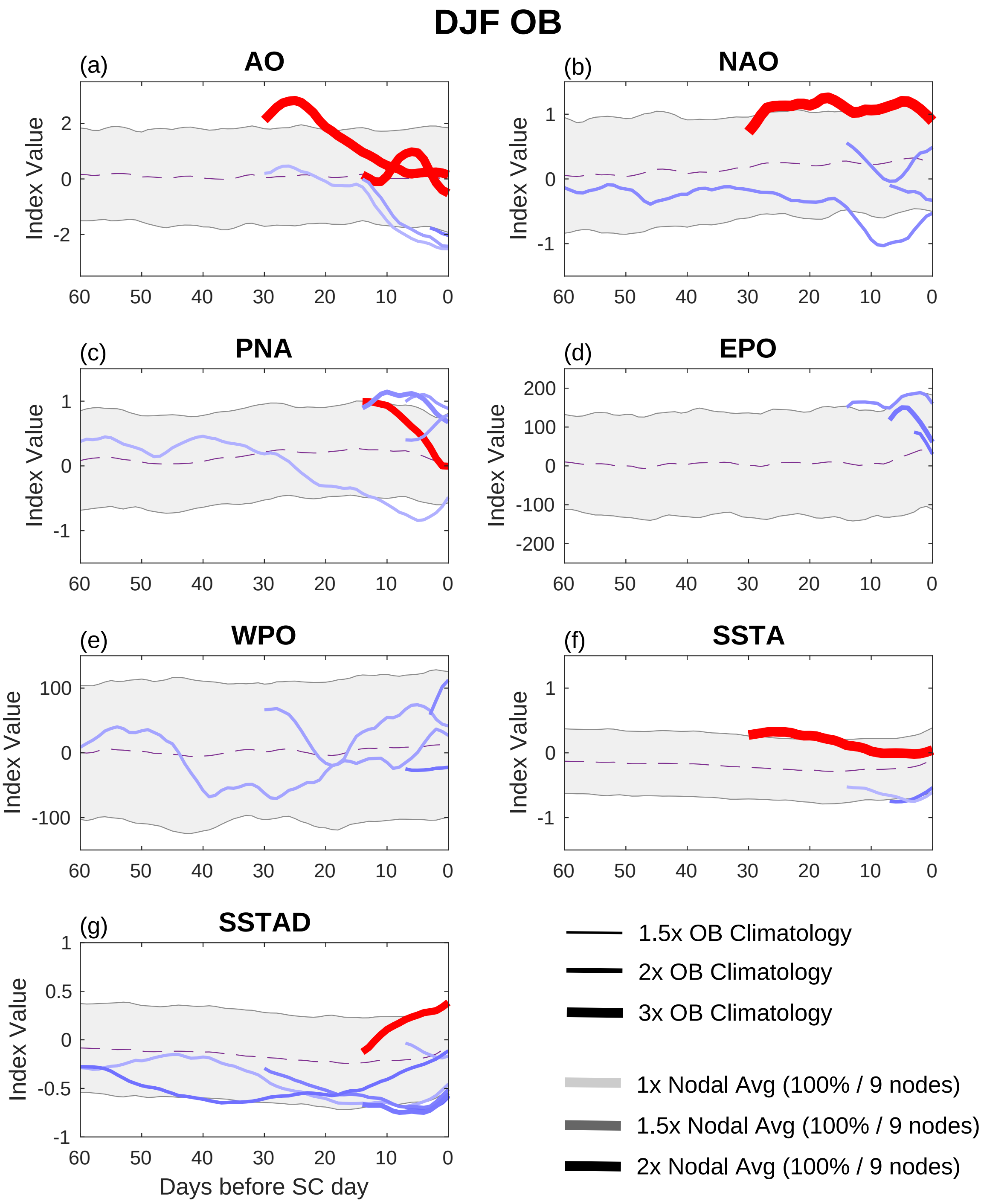

Figure 2.4: Same as Figure 2.2, but for DJF period. Reprinted from Brown and Nowotarski (2020), with permission from American Meteorological Society.

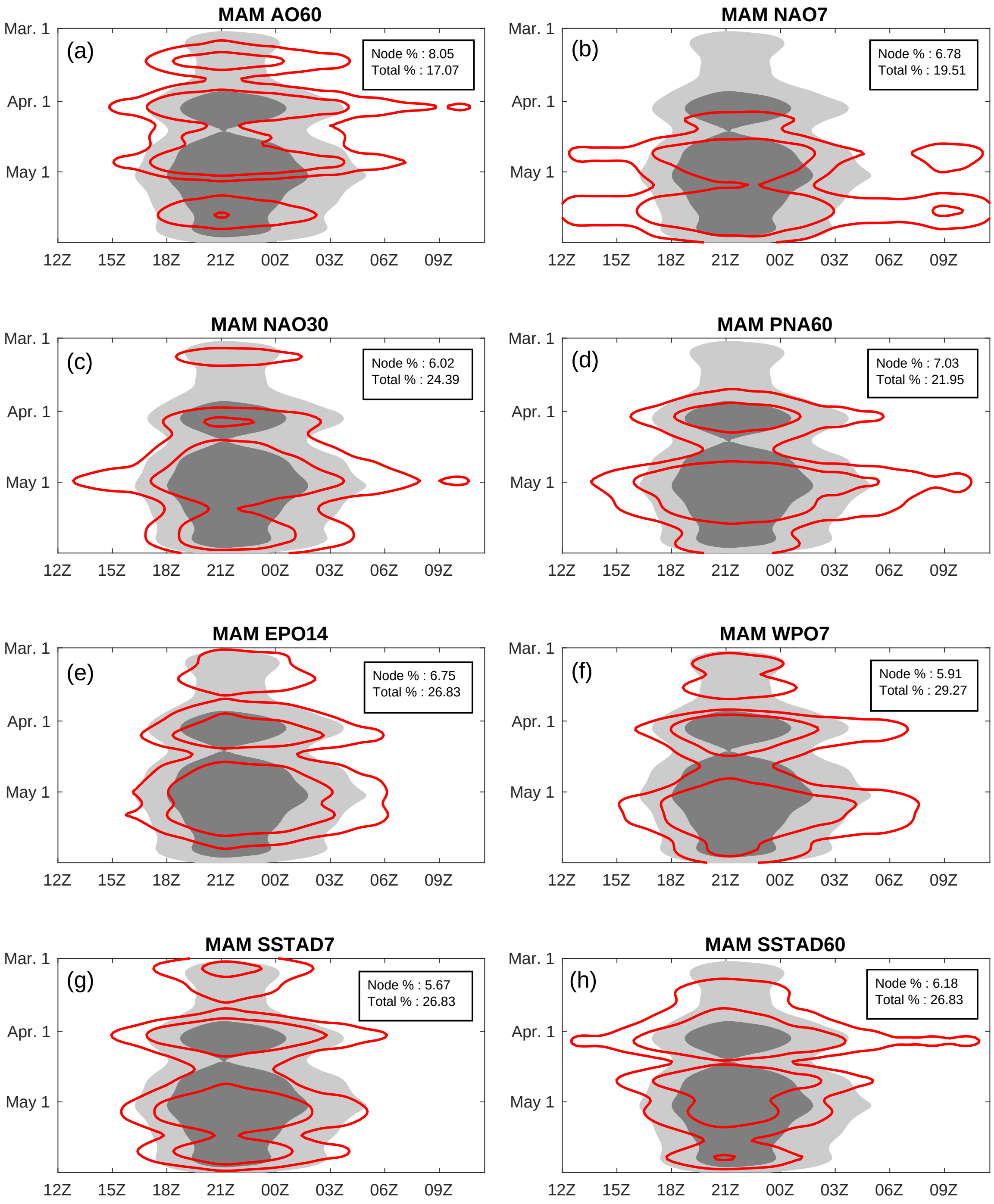

Figure 2.5: Kernel density of storm reports associated with MAM OB nodes by time of day and time of year, with outer and inner shading/contours representing the 75th and 90th percentiles, respectively; black shading corresponds to MAM climatology and red contouring corresponds to nodal distributions. Reprinted from Brown and Nowotarski (2020), with permission from American Meteorological Society.

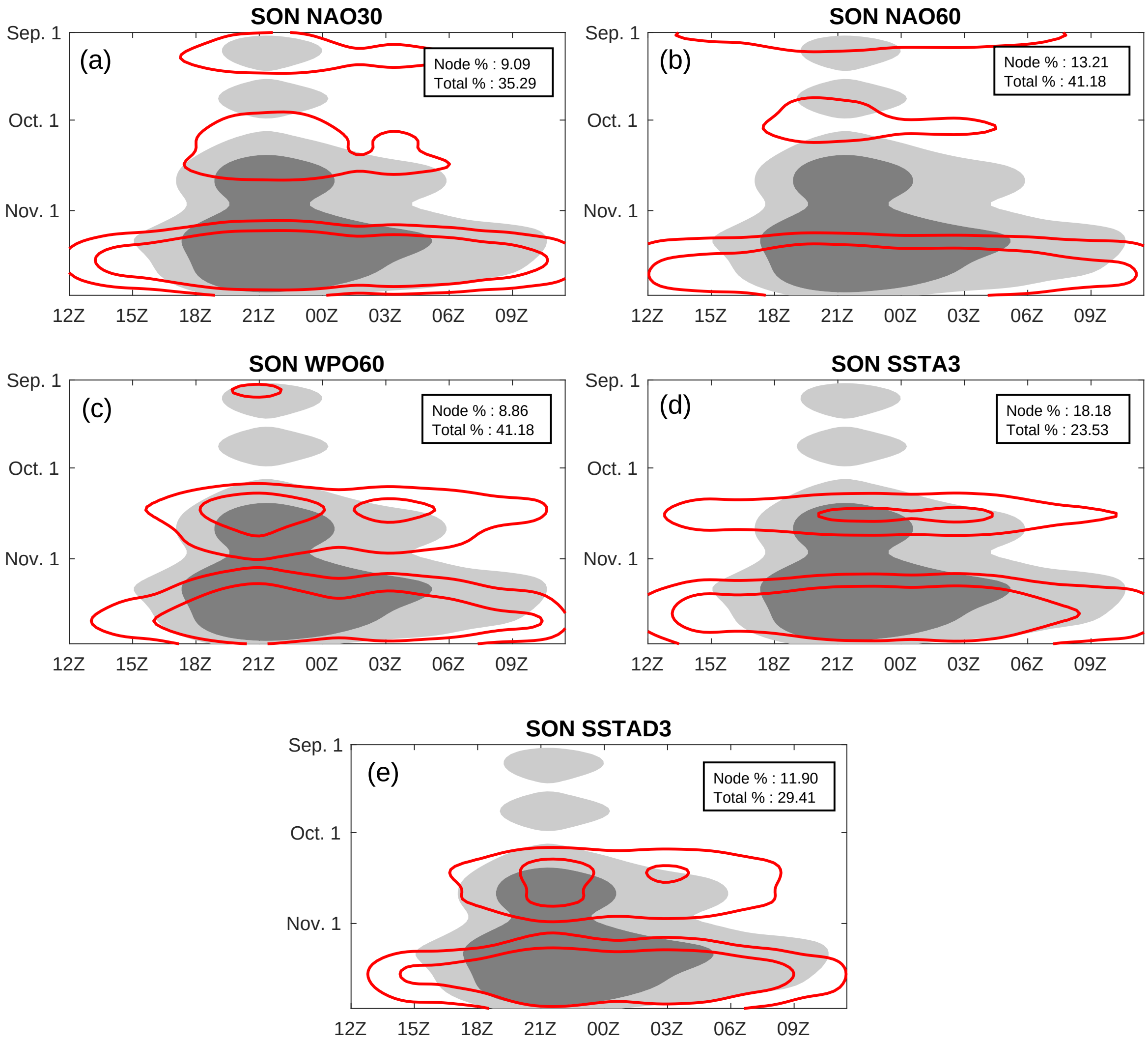

Figure 2.6: Same as Figure 2.5, but for SON period. Reprinted from Brown and Nowotarski (2020), with permission from American Meteorological Society.

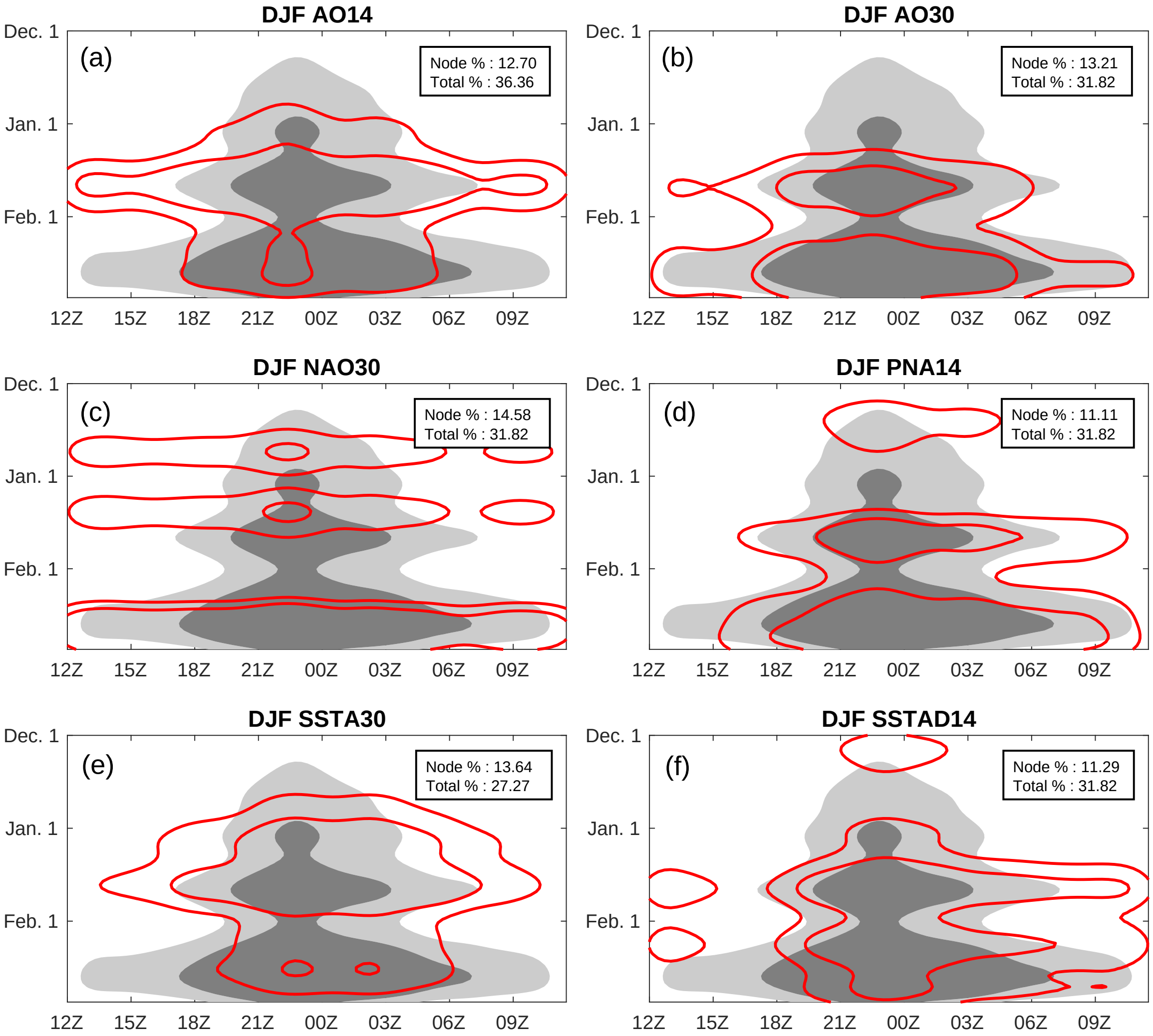

Figure 2.7: Same as Figure 2.5, but for DJF period. Reprinted from Brown and Nowotarski (2020), with permission from American Meteorological Society.

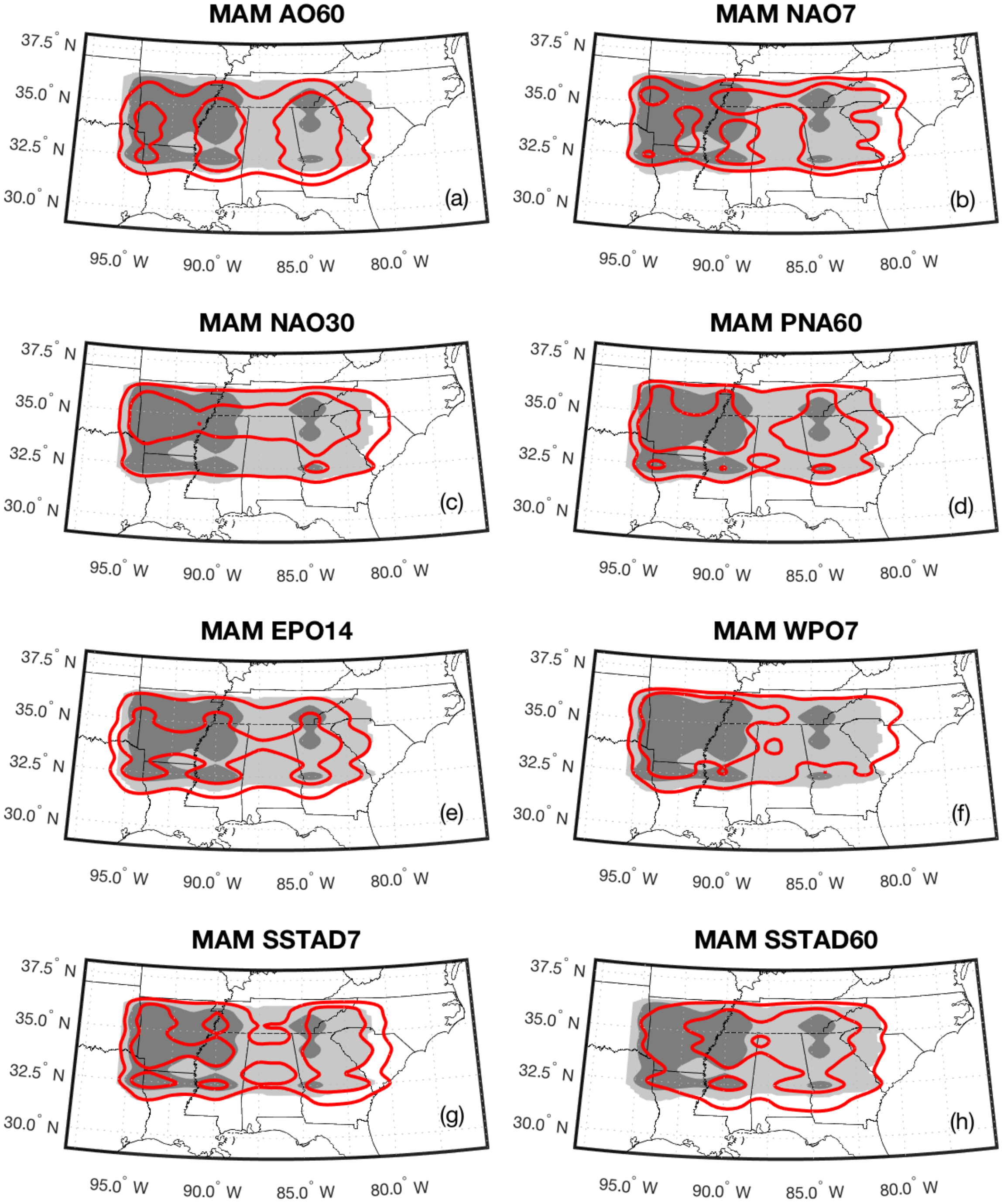

Figure 2.8: Spatial kernel density of storm reports associated with MAM OB nodes, with outer and inner contours representing the 75th and 90th percentiles, respectively; black contouring corresponds to MAM climatology and red contouring corresponds to nodal distributions. Reprinted from Brown and Nowotarski (2020), with permission from American Meteorological Society.

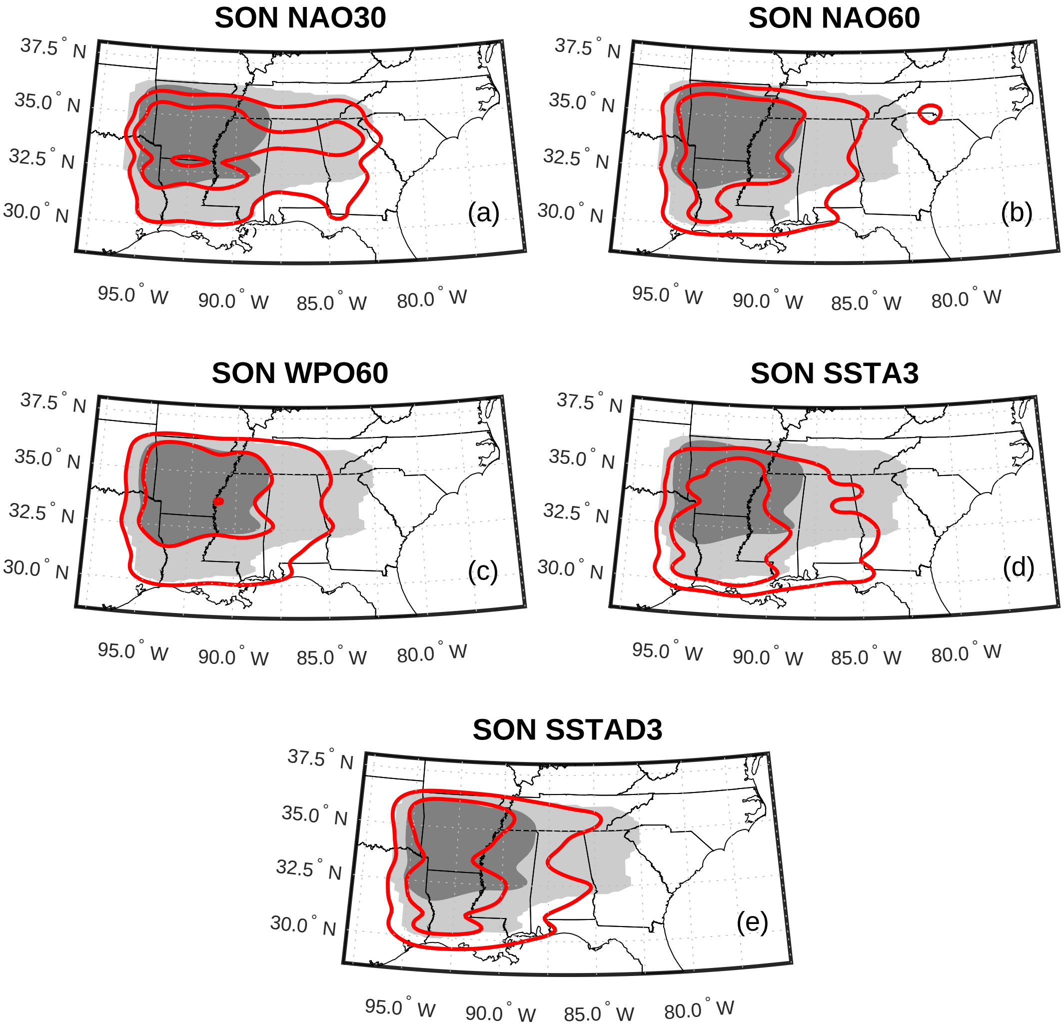

Figure 2.9: Same as Figure 2.8, but for SON period. Reprinted from Brown and Nowotarski (2020), with permission from American Meteorological Society.

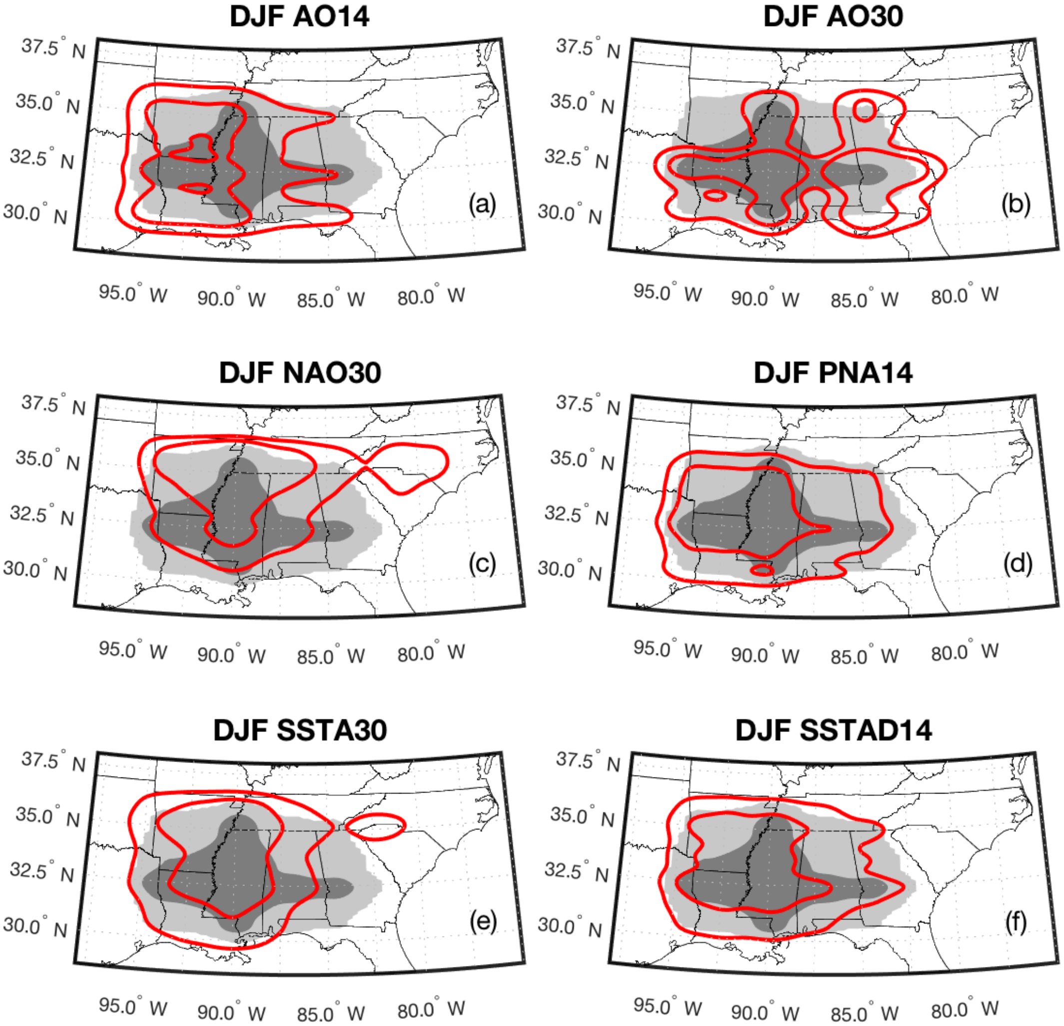

Figure 2.10: Same as Figure 2.8, but for DJF period. Reprinted from Brown and Nowotarski (2020), with permission from American Meteorological Society.

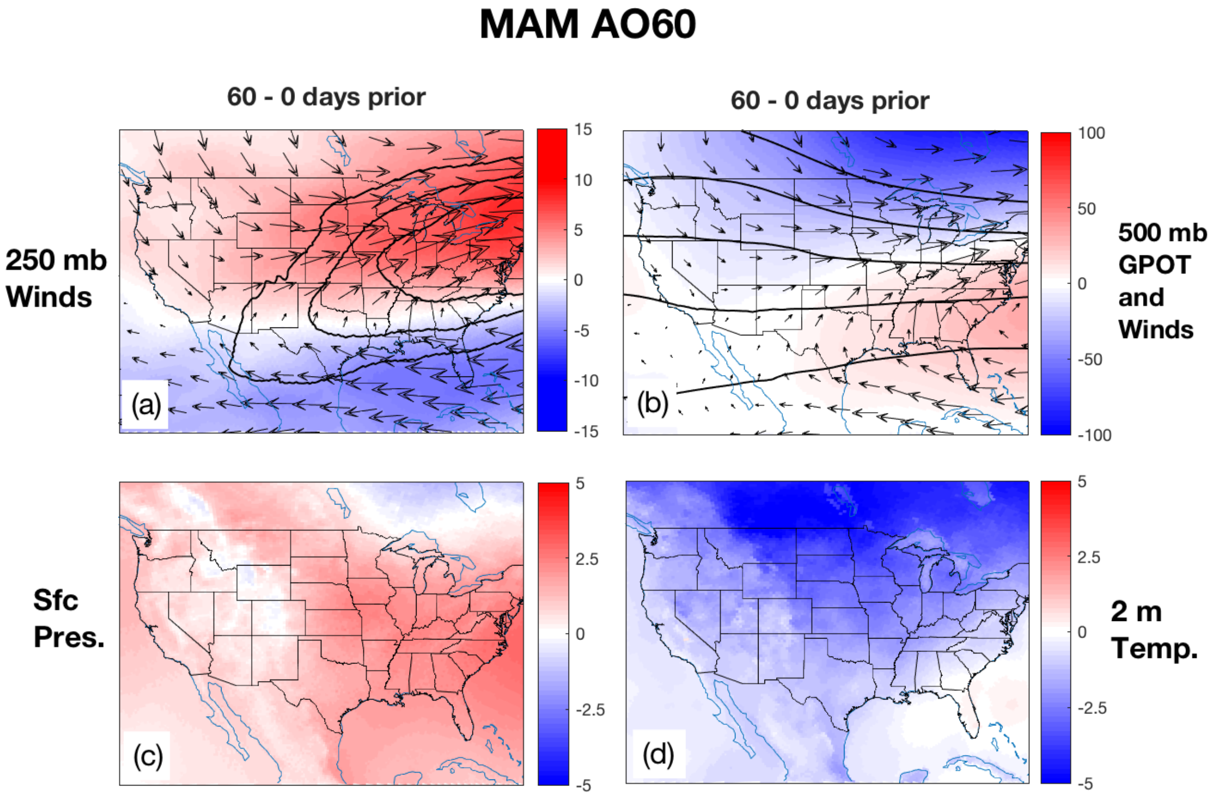

Figure 2.11: Composite anomalies associated with MAM AO60 pattern consisting of (a) 250-mb speed anomalies in m s^{-1} and wind anomaly vectors (with node average speed contours 40, 45, and 50 m s^{-1} shown in black), (b) 500-mb geopotential height anomalies in meters and wind anomaly vectors (with node average height contours of 5400, 5500, 5600, 5700, and 5800 m), (c) surface pressure anomalies in mb, and (d) 2-m temperature in K. Reprinted from Brown and Nowotarski (2020), with permission from American Meteorological Society.

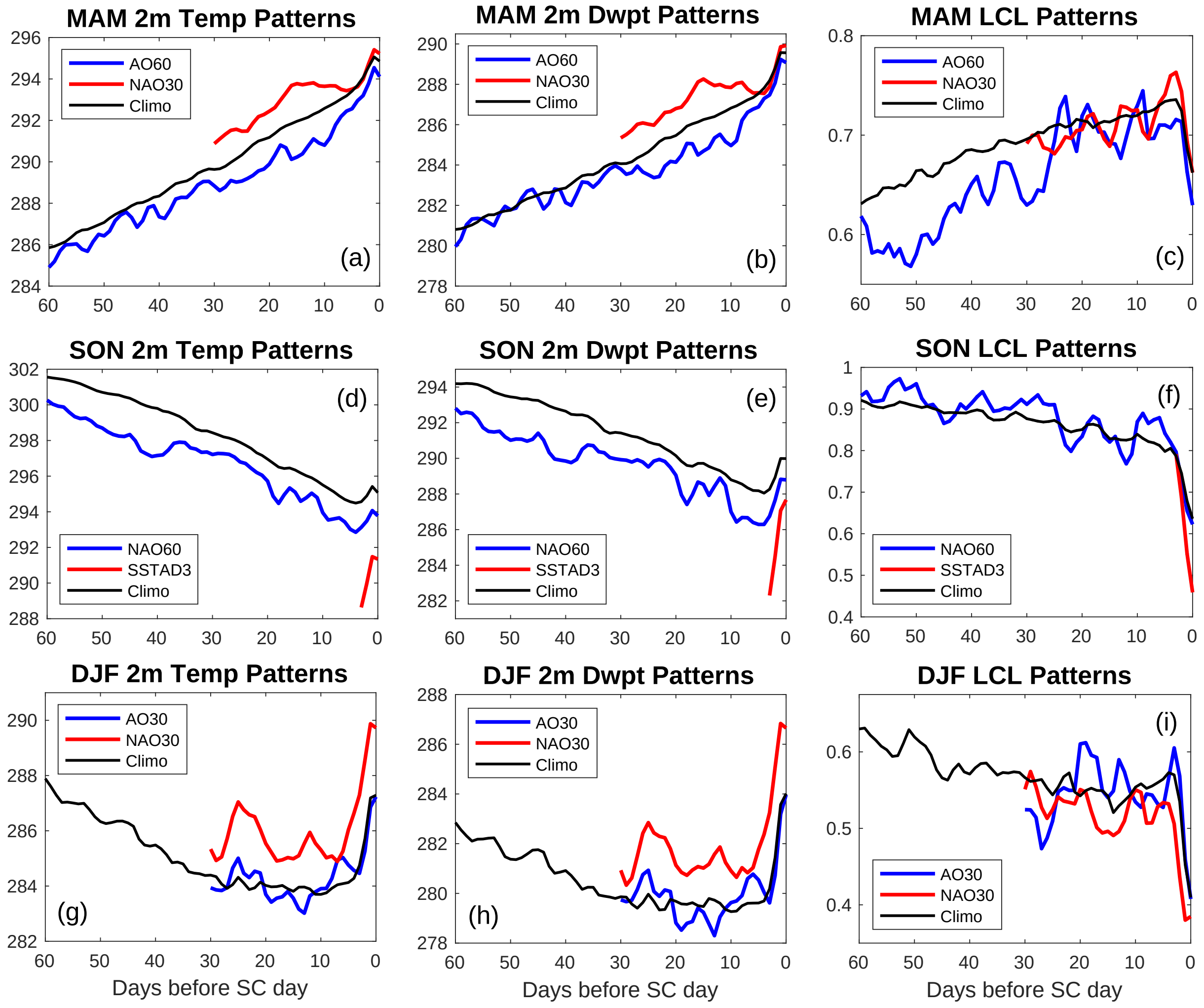

Figure 2.12: Time series of domain average 2m temperature (in K), 2m dewpoint (in K), and approximate LCL (in km) during the analyzed OB patterns as well as SC climatology (in solid black). Reprinted from Brown and Nowotarski (2020), with permission from American Meteorological Society.

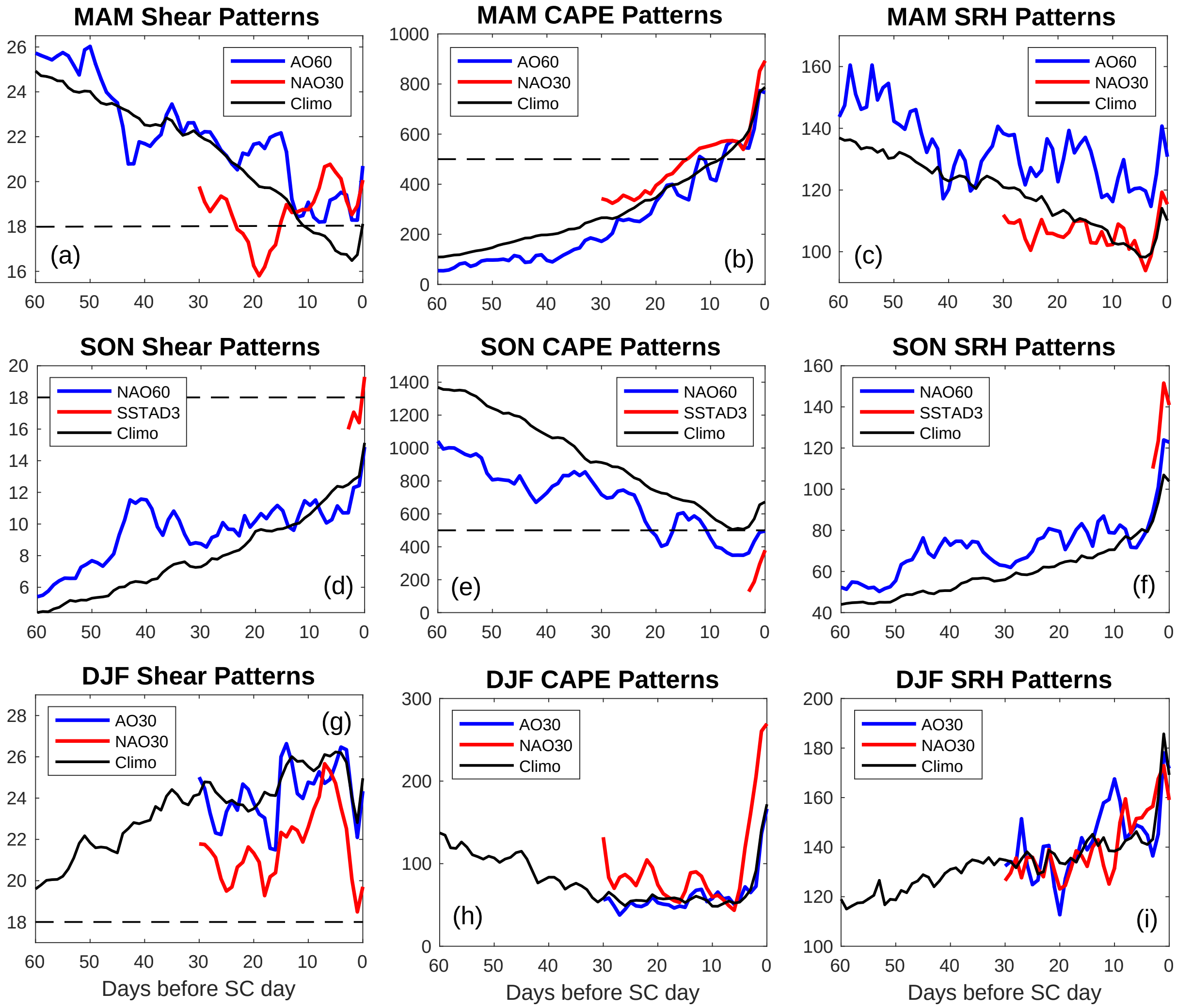

Figure 2.13: Time series of domain average deep-layer (10 m - 500 mb) shear (in m s^{-1}), SBCAPE (in J kg^{-1}), and 0-3 km SRH (in m^2 s^{-2}) during the analyzed OB patterns as well as SC climatology (in solid black), with the HSLC criteria from Sherburn and Parker (2014) shown by dotted black lines. Reprinted from Brown and Nowotarski (2020), with permission from American Meteorological Society.

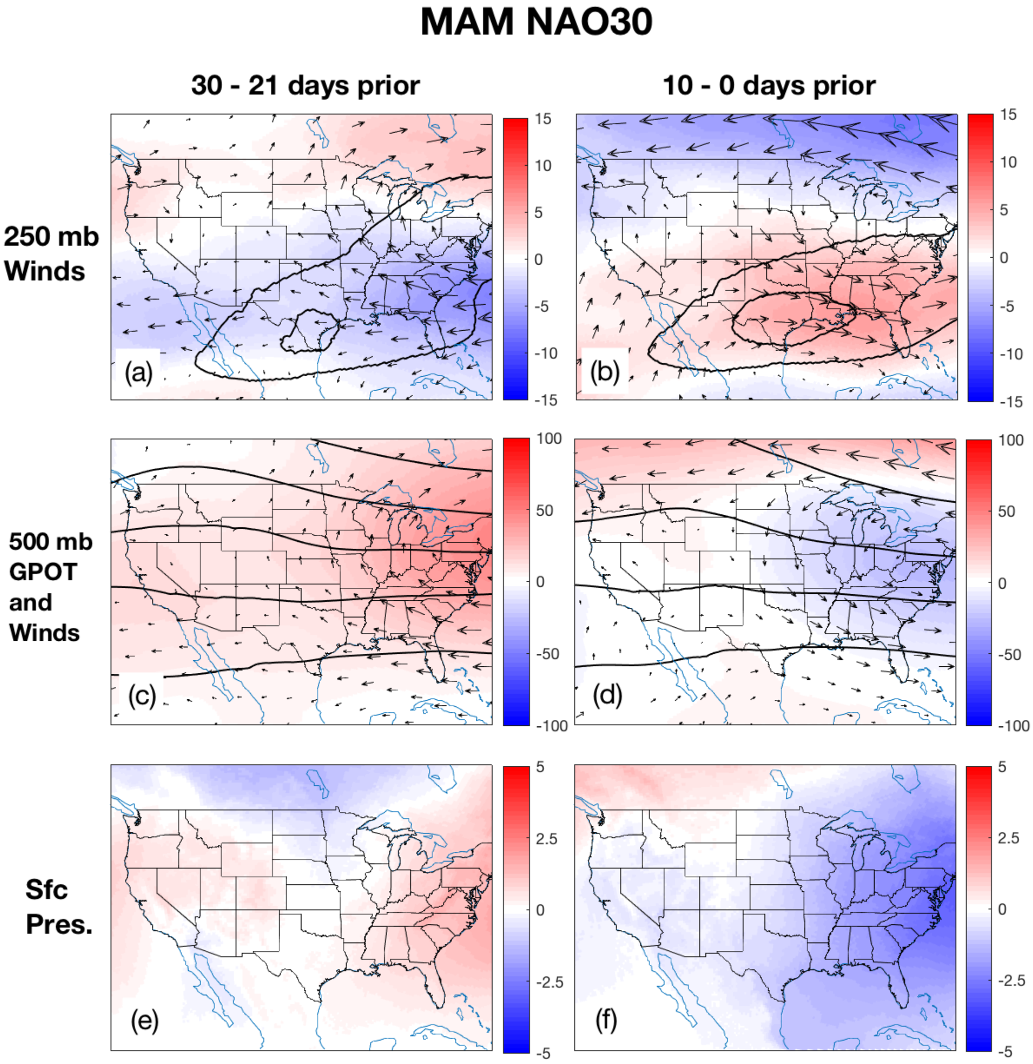

Figure 2.14: Composite anomalies associated with MAM NAO30 pattern consisting of (a)-(b) 250-mb speed anomalies in m s^{-1} and wind anomaly vectors (with node average speed contours of 40 and 45 m s^{-1} shown in black), (c)-(d) 500-mb geopotential height anomalies in meters and wind anomaly vectors (with node average height contours of 5400, 5500, 5600, 5700, and 5800 m), and (e)-(f) surface pressure anomalies in mb. Reprinted from Brown and Nowotarski (2020), with permission from American Meteorological Society.

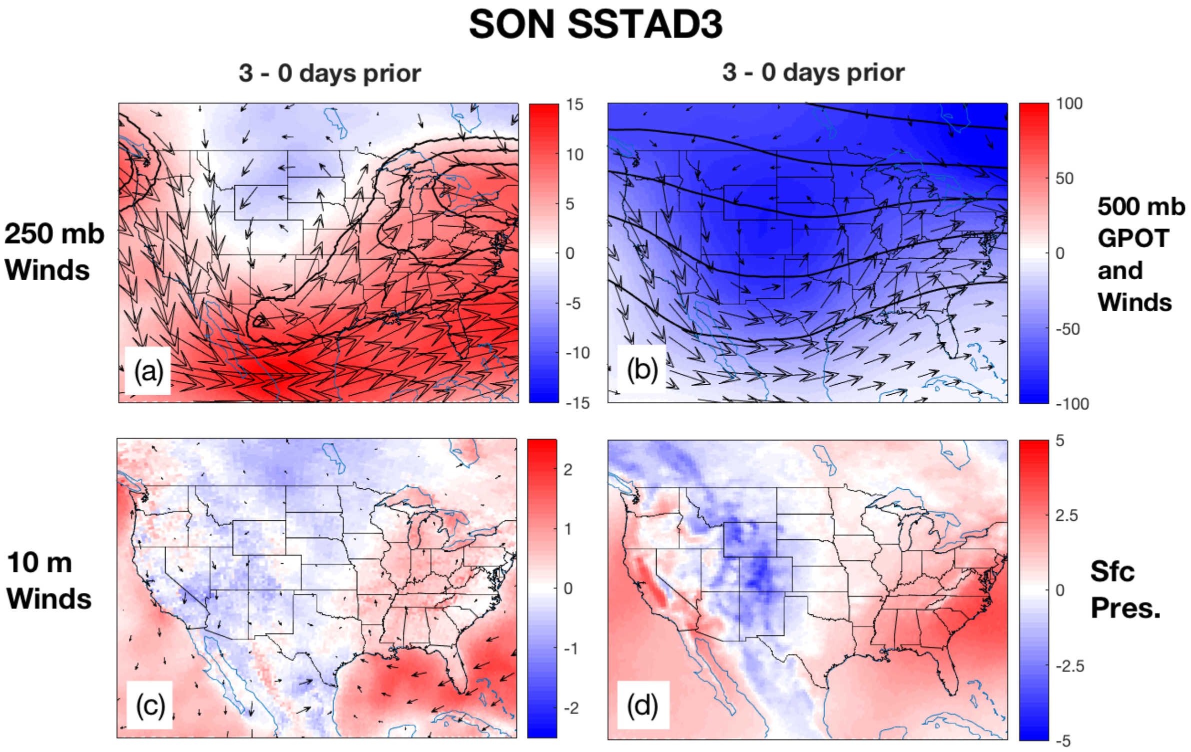

Figure 2.15: Composite anomalies associated with SON SSTAD3 pattern consisting of (a) 250-mb speed anomalies in m s^{-1} and wind anomaly vectors (with node average speed contours 40, 45, and 50 m s^{-1} shown in black), (b) 500-mb geopotential height anomalies in meters and wind anomaly vectors (with node average height contours of 5400, 5500, 5600, 5700, and 5800 m), (c) 10 m speed anomalies in m s^{-1} and wind anomaly vectors, and (d) surface pressure anomalies in mb. Reprinted from Brown and Nowotarski (2020), with permission from American Meteorological Society.

3. THE EARLY EVENING TRANSITION IN SOUTHEASTERN US TORNADO ENVIRONMENTS*

3.1 Introduction

The hours soon before and after local sunset constitute the early evening transition (EET), a period during which surface radiational cooling results in increasing static stability and convective inhibition (CIN). These thermodynamic changes are often accompanied by the onset of nocturnal low-level jets (NLLJ; Blackadar 1957; Shapiro et al. 2016), which can introduce additional low-level shear and storm-relative helicity (SRH) into nocturnal storm environments (relative to daytime environments) and have potential ramifications for storm maintenance and tornadogenesis (e.g., Maddox 1993; Markowski et al. 1998b; Parker 2014). These and other related factors have been offered up as explanation for the peak in near-sunset tornado counts noted in the literature (e.g., Kelly et al. 1978; Mead and Thompson 2011). Understanding how these environmental features and their impact on accompanying convection evolve with time are vitally important for determining the ability of storms to produce severe hazards through the EET. However, it remains unclear whether pre-sunset thermodynamic and kinematic characteristics influence the nature of this evolution and subsequent storm features.

The impact of boundary layer stabilization on near-ground rotation and the maintenance of intense updrafts has been addressed by the recent literature, largely within the context of supercells (e.g., Ziegler et al. 2010; Nowotarski et al. 2011; MacIntosh and Parker 2017), or transitions between supercells and other convective modes (e.g., Billings and Parker 2012; Peters et al. 2017; Geerts et al. 2017; Gropp and Davenport 2018, Gray and Frame 2019). Whether ingesting near-surface (as in MacIntosh and Parker 2017) or elevated air parcels (as in Nowotarski et al. 2011), the updrafts of nocturnal supercells have been shown to persist in spite of increasing environmental near-surface static stability. This resilience may be due to the upward pressure gradient accelerations caused

---

* Reprinted with permission from "The Early Evening Transition in Southeastern US Tornado Environments" by M. C. Brown and Nowotarski, C. J. and Dean, A. R. and Smith, B. T. and Thompson, R. L. and Peters, J. M., 2021. *Wea. Forecasting*, **36**(4), 1431-1452., ©2021 by American Meteorological Society.

in part by updraft rotation (e.g., Rotunno and Klemp 1982; Rotunno and Klemp 1985), which can act to lift negatively buoyant air (Markowski et al. 2012). Increases in low-level shear and SRH associated with the NLLJ may enhance upward accelerations in the lower updraft as demonstrated by the results of Coffer and Parker (2015), which act to increase the participation of near-surface parcels within updrafts in spite of their reduced buoyancy, as in Davenport and Parker (2015) and Gray and Frame (2019). These increases in low-level shear (along with deep-layer shear) have also been shown to increase the magnitude of storm-relative (SR) flow (e.g., Warren et al. 2017; Peters et al. 2019), which can both facilitate the transition from non-supercellular to supercellular modes (Peters et al. 2020b) as well as increase updraft width, buoyancy, and vertical velocity (Peters et al. 2019). Thermodynamic explanations for low-level updraft accelerations have also been offered in studies such as Brown and Nowotarski (2019), which demonstrated that upward buoyancy pressure accelerations (BPA) can exist in supercells below their level of free convection (LFC) despite the presence of CIN and negative buoyancy, which could be of importance for nocturnal supercells. Despite these studies, however, it is not apparent which situations allow these accelerations to overcome low-level stabilization during the EET, and which do not.

Gropp and Davenport (2018) analyzed Great Plains supercells and their near-storm environments as they progress through the EET. Using RUC and RAP proximity soundings, the authors found that large increases in SRH coupled with minimal increases in most unstable (MU)CIN support intense rotating updrafts, allowing supercells to persist well into the evening hours. This agrees with previous studies that found a greater risk of nocturnal supercell tornadoes in the presence of increased SRH (e.g., Davies and Fischer 2009) and reduced low-level static stability (e.g., Mead and Thompson 2011) associated with local moisture increases. This SRH relationship could again be a consequence of increased low-level SR flow (Peters et al. 2019, 2020b). Nevertheless, not all nocturnal tornadoes are supercellular, nor are they confined to the Great Plains. Previous studies of quasi-linear convective systems (QLCS) and their associated hazards (e.g., Trapp et al. 2005; Ashley et al. 2019) as well as the nocturnal tornado climatology of Kis and Straka (2010) have noted a nocturnal maximum in QLCS tornadoes, though the design and precision of their respective

QLCS classification methods vary. Such studies specifically noted that Southeast (SE) events comprise an appreciable fraction of the nocturnal and/or QLCS tornado climatologies. These insights, combined with both pre-existing and projected vulnerability to SE tornado hazards due to mobile home density, increased poverty rates, population increases, and expanding exurbia footprints (e.g., Simmons and Sutter 2007; Ashley et al. 2008; Strader et al. 2017), have given way to increased research focus on SE US tornadoes.

The aforementioned body of research has noted several characteristics common to SE storms and near-storm environments, including a skew towards cool season months and their nocturnal persistence, characterized by strongly sheared environments with limited buoyancy — termed high-shear, low-CAPE, or HSLC environments (e.g., Guyer and Dean 2010, Sherburn and Parker 2014, Sherburn et al. 2016, Anderson-Frey et al. 2019, Brown and Nowotarski 2020). Even the forcing of relevant atmospheric features like LLJs differ for the Southeast. For instance, Great Plains LLJs are influenced by the region's sloped terrain, whose associated thermal wind reversal in evening hours leads to a geostrophic wind maximum above the surface (e.g., Holton 1967) which can enhance preexisting NLLJs driven by nocturnal decoupling. This sloping terrain influence is diminished in the Southeast, and the strength of LLJs is instead perhaps modulated by ageostrophic jet streak circulations associated with midlatitude cyclones (Uccellini and Johnson 1979). Furthermore, Southeast LLJs and their attendant moisture transport can be enhanced by flow over the Intra-Americas Sea (IAS; Rasmusson 1967). Sometimes referred to as the IAS-LLJ, this feature has been shown to influence precipitation and tornadoes across the Southeast (Munoz and Enfield 2011).

Regarding predictability, Brown and Nowotarski (2020) demonstrated that climate-scale variability (e.g., Arctic Oscillation) can modulate SE synoptic patterns in ways that make them more favorable for tornado outbreaks, and even contribute to the formation of HSLC environments. On the storm-scale, however, HSLC tornadoes can be more difficult to predict than HSHC tornadoes (Dean and Schneider 2008; Dean and Schneider 2012; Anderson-Frey et al. 2019), and their increased nocturnal frequency poses enhanced risk to the public (e.g., Ashley et al. 2008). These factors provide both scientific and societal impetus to improve our physical understanding of how HSLC storm environments respond to and evolve across the EET, and what consequences these changes have for nocturnal tornadogenesis.

While some of these studies have considered diurnal variation in tornado characteristics, none to our knowledge have specifically examined how the changes in CAPE, shear, SRH, and CIN that occur during the EET influence the characteristics of subsequent tornadoes. One of the few studies we are aware of that has directly addressed the predictability of SE tornadoes occurring in the vicinity of the EET is Bunker et al. (2019), which found that effective-inflow layer quantities are more skillful nocturnal tornado predictors than fixed-layer quantities. The reason for this added skill of effective-inflow layer quantities is unclear, however, as is the matter of whether this skill is retained in low-CAPE environments. In other words, it is possible that the factors that help facilitate tornadogenesis in low-CAPE environments differ from those relevant in high-CAPE environments. Understanding how the atmospheric features discussed thus far evolve in time and in different background environments is crucial to assess the net effect of the EET on tornadogenesis potential. Based on this knowledge gap, this study addresses the following questions:

1. How do CAPE, shear, SRH, and CIN change during the EET in Southeast storm environments, and does this evolution depend on the amount of CAPE present before the EET (e.g. high-CAPE vs. low-CAPE)?

2. If EET evolution is CAPE-dependent, what impact do these differing evolution pathways have on the frequency and storm mode of subsequent tornadoes?

3. What environmental variables best discriminate between SE tornadic (or significantly tornadic) and nontornadic storms, and does their predictive skill vary as a function of background CAPE and/or storm mode?

4. Can existing forecast guidance metrics, such as STP, be adapted to better predict SE tornadoes using these variables?

Using a tornado event database [originally developed by Smith et al. 2012] spanning 2003 to 2018, we seek to identify SE tornadic events spanning the EET and characterize the CAPE and deep-layer shear of their near-storm environments prior to the EET. We will then analyze how these near-storm environments and the characteristics of their attendant convection evolve across the EET as a function of their CAPE and shear classifications. The next section details the severe weather report database and environmental data utilized in this study, as well the rationale for case selection and temporal binning. Section 3 reports on the results of our analyses, including the temporal characteristics of the SE tornado climatology, the evolution of the near-storm environment and associated storm and tornado characteristics, and the predictability of these tornadoes using proximity-sounding derived quantities. Finally, section 4 discusses the implications of these findings within the broader scope of the literature, as well as future research directions relevant to the study at hand.

3.2 Data and methods

The storm reports utilized in this study are from the updated version of the dataset originally developed in Smith et al. (2012), as used in Anderson-Frey et al. (2019), appended with all 2018 events. This tornado event dataset is developed by mapping county tornado segment data onto a 40 $\times$ 40 km^2 grid, and filtering such that the highest (E)F-scale rating is retained in every given hour and grid box. Severe wind or hail reports corresponding to grid hours with no tornadoes are used to characterize nontornadic environments.[1] Environmental data are matched with each report using the closest data grid point from the SPC hourly mesoanalysis grids (Bothwell et al. 2002), the basis of which are the Rapid Update Cycle (RUC; Benjamin et al. 2004) or Rapid Refresh Model (RAP; Benjamin et al. 2016), using the same 40-km grid spacing as the grid-hour report filtering described previously. Furthermore, the models assimilate rawinsonde, profiler, radar, lightning, and other data (Benjamin et al. 2016, their Table 3). Profiles of temperature, moisture, and wind above the

---

[1] Significant wind and hail reports are obtained using conventional definitions for 2003-2012. Wind and hail reports from 2014-2015 were obtained as part of Thompson et al. 2017, which employs an additional effective bulk shear criterion of 40 kt. Nontornadic cases are not included for 2013 and 2016-2018. Analyses were recomputed for only 2003-2012 reports to test sensitivity to these varying classifications, and results largely remained unchanged.

ground were based on the RUC model through April 2012, and the RAP model beginning in May 2012, with data every 25 mb in the vertical. The SHARPpy sounding analysis software (Blumberg et al. 2017) was used for all parameter calculations for the SPC mesoanalysis sounding profiles matched to each grid-hour tornado or severe-storm event. As with any model output, this dataset carries its own limitations and biases, the details of which are discussed extensively in Thompson et al. (2012) and Anderson-Frey et al. (2016). Limitations relevant to this study — particularly grid spacing — are discussed in later sections.

Radar data and a convective mode decision tree (Fig. 2 in Smith et al. 2012) are then used to manually classify convective mode. As noted in previous literature, the majority of resulting modes such as QLCS and right-moving supercell (RMS) are mutually exclusive, though some overlap is allowed with classifications such as tropical cyclone (TC). Similar to Brown and Nowotarski (2020), all reports associated with TCs are removed, as TC tornado environments are beyond the scope of this study. The remaining storm modes are consolidated into three broad categories — supercell (including all isolated supercells and supercell in line features), QLCS (including all QLCS, bow echo, and non-supercellular cell in line structures), and disorganized (all non-supercellular clusters, cells, and any combinations thereof). Additionally, tornadoes with rating F/EF0-1 are considered weakly tornadic, and F/EF2+ considered significantly tornadic[2]. The same domain defined in Anderson-Frey et al. (2019), consisting of Alabama, Arkansas, Georgia, Kentucky, Louisiana, Mississippi, and Tennessee, is used for consistency with previous literature.

In order to isolate storm environments likely impacted by the EET, local sunset (SS) time is computed for each storm report based on its location and time of year, and rounded to the nearest hour. Each storm report time is similarly rounded, and then arranged into hourly bins relative to its associated SS. The EET is defined following past studies of this time of day, such as Anderson-Frey et al. (2019), spanning ± 2 hours off local SS time. The four hours immediately prior to and after this transition (i.e., SS-6 to SS-3, and SS+3 to SS+6) constitute the pre- and post-transition periods, respectively. By focusing our analyses on this ± 6-hour window centered on local SS, we can

---

[2] These cutoffs are chosen for consistency with numerous other studies in the literature. The suitability of these cutoffs for the SE tornado climatology is examined in section 4.

specifically analyze the environmental changes introduced by the EET, and limit potential overlap of severe convection persisting into subsequent days.

We also seek to classify background CAPE/shear to assess potential influence on environmental changes across the EET. Numerous classification methods have been implemented in the literature. For the purposes of this study, we have chosen a blend of two common methods in which a 06-km bulk wind difference (SHR6) of $\geq$ 18 m s^{-1} is used to denote high-shear. Low-shear conditions are not examined as they correspond to only 10% of all SE tornadoes, consistent with the SHR6 distributions of Thompson et al. (2013). Low-CAPE is defined as an environment with surface-based (SB)CAPE $\leq$ 500 J kg^{-1} as well as MUCAPE $\leq$ 1000 J kg^{-1} (as in Sherburn and Parker 2014), while high-CAPE requires mixed-layer (ML)CAPE $\geq$ 1000 J kg^{-1} (e.g, the complement of the method used in Anderson-Frey et al. 2019). This approach gives two mutually exclusive CAPE/shear categories (HSHC and HSLC) and will assist in determining how aspects of the near-storm environment relevant to tornadogenesis change as a function of buoyancy.

3.3 Results

3.3.1 Diurnal tornado distributions

The criteria described above yield 9250 severe events spanning 1448 individual days (1200-1200 UTC periods) in our prescribed domain and study period. Limiting our scope to the three periods defined earlier (pre-transition, EET, and post-transition), there are 7052 severe events spanning 1258 unique EET periods (± 6 h from local SS). Of these reports, 2796 (39.6%) are significant wind (sigwind), 1105 (15.7%) are significant hail (sighail), 2518 (35.7%) are weak tornadoes (weaktor), and 633 (9.0%) are significant tornadoes (sigtor). These 3151 tornadoes represent over 70% of all SE tornado reports, further underscoring the need to understand the environmental changes induced during the EET.

Before we consider environmental evolution, however, we must examine the temporal distribution of SE tornadoes. Figure 3.1a shows the diurnal cycle of SE tornadoes (in light blue) and sigtors (in black) during the pre-transition, EET, and post-transition periods (marked in dotted black). Tornadoes show a broad bell curve skewed slightly towards pre-SS hours, peaking one hour prior to sunset. Sigtors peak at this same hour, but show less diurnal variability overall such that sigtors account for a larger fraction (over 25%) of post-transition tornadoes. Figure 3.1b-d break down these diurnal tornado distributions further by mode. Unsurprisingly, we see that supercell tornadoes and sigtors (Fig. 3.1b) — the predominant tornadic mode in the climatology — are nearly identical to the overall distribution, though sigtors make up an even larger fraction of nocturnal supercell tornadoes. QLCS tor/sigtors (Fig. 3.1c) are less frequent than supercell tornadoes, but still constitute an appreciable fraction of the SE tornado climatology. This QLCS subset exhibits almost no diurnal variation, with tornadoes and sigtors occurring somewhat equally through the EET. Disorganized tornadoes (Fig. 3.1d) differ entirely in that they are largely confined to daytime hours and contain no sigtors, as might be expected for this convective mode. Post-EET increases in non-supercellular tornado counts may be related to the theorized peak in NLLJ intensity roughly 6-hr post-sunset presented in the literature (Shapiro et al. 2016), though this model applies to the Great Plains NLLJ.

3.3.2 Storm environment evolution

The near-storm environment can change quickly and substantially during the EET. For instance, afternoon HSHC conditions may transition to evening HSLC conditions as buoyancy decreases in response to EET cooling and stabilization. Therefore, we must examine these changes and determine whether they have an impact on the frequency, timing, and convective mode of tornadoes. To do so, we categorize each severe convective day based on when its associated storm reports occurred; these temporal groupings include the pre-transition, EET, and post-transition (as defined earlier) and all combinations thereof, resulting in seven mutually exclusive categories. The category of days with reports in only the pre- and post-transition periods is excluded from subsequent analyses due to substantially smaller report counts. By analyzing the remaining categories, we can ascertain what aspects of the near-storm environment impede or facilitate the maintenance of severe convection across the EET.

We will first examine the days in which storms persisted across all three of our defined periods. Interestingly, only 10% of severe convective days in the SE climatology fall in this category, emphasizing the unique conditions that are likely necessary for convection to produce severe hazards through the EET. For each day and period, we classify its general CAPE/shear characteristics and consider how variables evolve consequently. For instance, if the average pre-transition environment is HSHC, how do CAPE and shear evolve consequently? Alternatively, if the post-transition environment is HSHC, how do CAPE and shear evolve earlier to arrive at that environment? This process is carried out for both environmental classifications, providing a "road map" of how storm environments can evolve diurnally, as shown in Fig. 3.2. Each figure column corresponds to the period that is being used to determine the CAPE/shear category (i.e., column 1 graphs are classified based on the pre-transition environment, and so on as shaded in gray). HSHC and HSLC patterns are displayed in red and blue, respectively. This means, for example, that a blue line in column 2 represents a pattern corresponding to days in which the EET has average HSLC conditions. A two-sample *t* test (at the 95% confidence level) is carried out between the data in each period. Filled (unfilled) data points indicate when the differences between the HSHC and HSLC patterns are statistically significant (insignificant). The sample sizes associated with these patterns are provided in Table 3.1.

HSHC environments show gradual decreases in CAPE throughout the day regardless of which period is used. HSLC CAPE patterns, however, vary based on the constraining period. When the pre-transition environment is HSLC (blue line in column 1), CAPE values start low, but increase gradually during the EET, likely due to increases in moist instability signaled by changes in low-level equivalent potential temperature (θ_e, as computed in SHARPpy; Appendix Fig. C.1a) or other related low-level thermodynamic variables (Appendix Table C.1). When the EET or post-transition environment is HSLC (blue line in columns 2-3, respectively), CAPE starts at moderate values during the pre-transition, before decreasing and remaining relatively low. Interestingly, HSLC CAPE values remain statistically lower than HSHC values the entire day, despite being conditioned on only one period. Regarding SHR6, both environments exhibit sustained, high values the entire day regardless of the constraining period, but HSLC patterns (particularly those based on the pre-transition and EET) maintain higher overall shear magnitudes than HSHC. If we were to examine those environments that comprise the middle ground between these classifications (high-shear, moderate-CAPE), we would see that their associated CAPE/shear values understandably lie in between the HSHC and HSLC patterns, but the shape of their patterns largely resemble HSHC patterns.

If we consider the implications of these patterns for storm environment, we see that HSHC environments remain almost entirely in that environmental category, despite diurnal CAPE decreases. In contrast, there are no mean pathways in which an HSLC storm environment persists from the pre-transition through to the post-transition. Rather, HSLC environments on average are transient, evolving from or into other environments throughout the day (even all the way from HSHC conditions). In fact, only four severe convective days in the entire dataset maintain average HSLC conditions through all three periods. This of course could be influenced by the coarse spatial resolution of the environmental dataset utilized and the CAPE/shear thresholds employed, the implications of which are discussed later. However, these insights, combined with the fact that these HSLC transitions occur primarily near local SS, highlight the unique relationship between the EET and the formation of HSLC environments.

In order to characterize the low-level accelerations potentially associated with the NLLJ, Fig. 3.3 displays 0-1 km SRH and shear patterns (SRH1 and SHR1, respectively) following the same approach as Fig. 3.2. As is expected, both of these quantities show relatively similar patterns, with SRH1/SHR1 values steadily increasing through and past local SS. As with SHR6, HSLC pre-transition and EET conditions correspond to uniformly higher SRH1/SHR1 values than HSHC patterns. Though representing a different portion of the atmosphere, effective layer SRH (Eff SRH) was also considered, and showed similarly favorable SRH trends associated with HSLC pre-transition conditions (Appendix Fig. C.2a). Interestingly, HSLC pre-transition patterns show a decrease in SRH1/SHR1 during the EET before rapid post-transition increases, perhaps related to changes in boundary layer mixing and/or stabilization. Regardless, these observations suggest that at least some portion of these storm environments coincide with the strengthening flow and helicity associated with an intensifying LLJ, which may play a compensating role in buoyancy-deficient environments.

Given studies such as Mead and Thompson (2011) and Given studies such as Mead and Thompson (2011) and Gropp and Davenport (2018) relating CIN to nocturnal supercell maintenance, Fig. 3.4 shows time series of SB, ML, and MUCIN following the same environment-time classification of Fig. 3.2. Regardless of the period used for classification, HSHC CIN values generally increase in absolute magnitude with time. The same can be said of several HSLC CIN patterns, particularly those conditioned on the post-transition environment (column 3 in Fig. 3.4). Though these patterns are largely indistinct from HSHC post patterns, uniformly lower downdraft CAPE (DCAPE) values (Appendix Fig. C.3c) may contribute to weaker (e.g., less negatively buoyant) outflow such that storm updrafts are able to persist despite lower CAPE and increasing CIN. In contrast to these HSLC Post patterns, CIN patterns associated with pre-transition or EET HSLC conditions (Fig. 3.4a,b,e,h) exhibit *destabilization* (or more gradual stabilization) as the evening progresses, with statistically smaller nighttime CIN magnitudes relative to HSHC patterns. These decreases in CIN magnitude develop in tandem with increases in low-level lapse rates (Appendix Fig. C.1b), presumably driven by warm-air advection (or differential advection) often associated with NLLJs.

Clearly the near-storm environments of SE storms evolve differently as a function of CAPE/shear characteristics, so it should stand to reason that the frequency and convective modes of their tornadoes do so too. To test this, we consider both the fraction of storm reports in each period that are tornadic, as well as the modal breakdown of those tornadoes, following the same period classification as Figs. 3.2-3.4. Normalizing by climatological fractions in each period[3], we diagnose the percentage change in the frequency and mode of tornadoes, as shown in Fig. 3.5. For instance, if climatologically 5% of all reports in the pre-transition produce tornadoes, and some subset of those reports associated with one of our environmental classifications is comprised of 7.5% tornadoes,

---

[3] These climatological fractions were computed across all days in which convection persisted across all three periods.

Fig. 3.5 would display a 50% increase in the fraction of pre-transition storms (for that classification) that produce tornadoes.

Interestingly, HSHC conditions have a limited influence on tornado fraction, though HSHC post-transition conditions (red bars in Fig. 3.5c) correspond to slightly increased EET and post-transition tornado fractions likely due to overall higher CAPE values. HSLC conditions in a given period lead to decreases in tornado fraction *during that period* (i.e., pre-transition HSLC bar in Fig. 3.5a, post-transition HSLC bar in Fig. 3.5c), likely due to their inherently limited instability. However, pre-transition HSLC conditions progress with large pre- to post-transition swing towards increased tornado fraction in association with overall higher and increasing SRH1/SHR1 values (Fig. 3.3a,d) and post-sunset decrease in SBCIN magnitude (Fig. 3.4a). If we condition based on the high-shear, moderate-CAPE environment discussed earlier (not shown), we see large, uniform increases in tornado (and sigtor) fraction regardless of the threshold period, which could imply there exists an ideal combination of the ample instability of HSHC environments and invigorated low-level dynamic support of HSLC environments.

Regarding mode, HSHC conditions tend to have a small, but generally positive effect on the prevalence of supercellular tornadoes, particularly when the post-transition has HSHC conditions (Fig. 3.5f). HSLC conditions in any period, as with tornado fraction, facilitate a decrease in supercellular tornadoes in that and subsequent periods (Fig. 3.5d-f). Conversely, these HSLC conditions correspond to an increase in the prevalence of QLCS tornadoes (Fig. 3.5g-i). If we were to consider raw changes relative to climatology (not shown) rather than normalized changes, we would see that these shifts in the prevalence of supercell and QLCS tornadoes are nearly equal and opposite, implying a direct trade-off between these modes as a function of environment. It is worth noting that the relative magnitudes of the HSHC and HSLC trends may be influenced by differing sample sizes (also shown in Table 3.1), but these results still highlight the noticeable influence that the daytime storm environment can have on storm characteristics later that evening.

Given the modal exchanges shown in Fig. 3.5d-i, Figs. 3.6-3.8 present the patterns of Figs. 3.2-3.4, respectively, separated by mode. Given reduced sample size in portions of this modal subset, median values and Mann Whitney tests are substituted for mean values and t tests in order to account for potential non-normality. Solid lines represent supercell patterns and dashed represent QLCS patterns, and statistical testing is performed across environments for each mode (e.g., data points on dotted lines represent statistical differences between HSHC and HSLC QLCS patterns). Figure 3.6a-i shows that CAPE patterns are generally consistent across mode, with slightly higher CAPE values for supercells. The same can be said of SHR6 (Fig. 3.6j-l), though the differences between HSHC and HSLC QLCS patterns is more pronounced than they are for supercells. This latter point is also true for SRH1/SHR1 (Fig. 3.7), particularly when conditioning on the pre-transition environment (Fig. 3.7a,d). Also peculiar in Fig. 3.7a is that the HSLC Pre pattern associated with supercells does *not* show the monotonic SRH1/SHR1 increase that the QLCS pattern does, suggesting diminished NLLJ influence and perhaps more influence of cyclone-induced LLJs (as with the strong synoptically forced HSLC environments in Sherburn et al. 2016). The HSLC nocturnal destabilization demonstrated in Fig. 3.4 is also apparent in the modal CIN patterns of Fig. 3.8, though post-transition CIN values are smaller in magnitude for supercells. Altogether, these modal patterns suggest that increased low-level shear/SRH associated with HSLC conditions can be primarily attributed to QLCS modes, which draws into question what environmental factors are compensating for a lack of instability in HSLC supercell environments. Perhaps the subtle destabilization shown in Figs. 3.6,3.8 coupled with overall high shear values is sufficient to sustain supercells in HSLC Pre environments.

As noted, however, it is far more likely for severe convection *not* to persist through all three periods. Thus, we also consider the evolution of environmental variables as a function of nocturnal persistence. For instance, do variables like CAPE evolve differently for storms occurring only in the pre-transition relative to those which persist into subsequent periods? Figure 3.9 shows the hourly-averaged variables examined in Figs. 3.2-3.4 along with three derived parameters associated with each temporal period combination. The sample sizes for each temporal category (summed over each of its constituent periods) are included in Table 3.2. The limiting factor for storms to persist past that pre-transition appears to be overall smaller values of SRH/SHR variables, as with storms occurring solely in the pre-transition period (red lines in Fig. 3.9d-f). Though convection clearly can form in these environments, the favorable dynamic forcing associated with increased shear and SRH nay be necessary for storms to survive the rapid CAPE decreases and CIN magnitude increases of the EET. The same can be said about storms that fail to persist past the EET (orange and yellow lines in Fig. 3.9d-f), which have noticeably lower EET SRH1/SHR1 values compared to patterns which persist into the post-transition (green and black lines in Fig. 3.9d-f). These EET-limited patterns also display more rapid decreases in MLCAPE and increases in MUCIN magnitude (Fig. 3.9b,i, respectively). Conversely, days in which convection spans all three periods (black lines) exhibit sustained higher values of shear and SRH paired with more gradual changes in CAPE and CIN. These differences manifest themselves in the evolution of common derived metrics, including supercell composite parameter (SCP; Thompson et al. 2012), the original STP formulation (STP-T03; Thompson et al. 2003) and effective layer STP (STP-E; Thompson et al. 2012), as shown in Fig. 3.9j-l. Of the derived metrics utilized in this study (as summarized later), STP-T03 shows the largest spread numerically between the different temporal periods for STP parameters, as does SCP for non-STP parameters.

Again we ask whether this environmental variability translates to We then ask whether the environmental variability in Fig. 3.9 influences the prevalence and characteristics of tornadoes among the analyzed temporal categories. To this end, Fig. 3.10 shows the period-wide tornado characteristics for the storms contributing to the patterns in Fig. 3.9, following the same color scheme. These include the fraction of all storms in each period (as indicated in Table 3.2) producing tornadoes (Fig. 3.10a) and sigtors (Fig. 3.10b), as well as the convective mode (Fig. 3.10c-d) and environment (Fig. 3.10e-f) of these tornadoes. This means, for example, that the yellow circle in Fig. 3.10a corresponds to the fraction of storms contributing to the yellow lines in Fig. 3.9 that produced a tornado. From Fig. 3.10a-b, we see that the highest tor and sigtor percentages occur in those categories involving the EET and/or the post-transition, possibly related to overall higher 0-1 km shear and SRH values maintained on these days. For storm mode (Fig. 3.10c-d), the majority of tornadoes occur in supercells, regardless of category or period. Regarding environment, Fig. 3.10e shows that the two categories spanning both the EET and post-transition (EET and Post, and All Periods) have noticeably higher HSHC fractions, consistent with the CAPE patterns presented thus far. Additionally, the prevalence of HSLC tornadoes gradually increases as the day progresses (Fig. 3.10f), along with an increase in QLCS tornado percentage, as suggested by the tornado diurnal cycles in Fig. 3.1. The same general trends hold true for sigtors (not shown), though understandably an increased skew towards HSHC and supercell classifications exist for this subset of tornadoes.

3.3.3 Storm environment and tornado predictability

The factors contributing to tornadogenesis in high-CAPE (particularly HSHC) environments have been thoroughly explored in the literature, but less in low-CAPE environments. As such, we seek to identify environmental variables that effectively discriminate between tornadic (or significantly tornadic) and nontornadic storms in HSLC environments and compare them to HSHC predictors. There are a number of potential physical pathways by which HSLC environments may be able to sustain robust low-level updrafts and support tornadogenesis. From a thermodynamic perspective, previous HSLC studies (e.g., Sherburn and Parker 2014; Sherburn et al. 2016) have demonstrated that increased low-level (e.g., 0-1, 0-3 km) lapse rates help sustain HSLC convection by invigorating low-level buoyant accelerations, and therefore contribute to their longevity and ability to develop intense near-surface vortices (Sherburn and Parker 2019). Similar consequences may result from an accumulation of low-level instability such as 0-3 km CAPE (Sherburn et al. 2016), or less negatively buoyant outflow (e.g., Markowski et al. 2002; Shabbott and Markowski 2006; Brown and Nowotarski 2019). Alternatively, increased low-level shear and SRH in the presence of a low-level mesocyclone can result in dynamically enhanced vertical accelerations (e.g., Coffer and Parker 2015; Sherburn and Parker 2019), which dominate the production of intense low-level vertical velocities in CAPE-deficient storms (Wade and Parker 2021). Also relevant for low-level updraft maintenance are the storm's effective inflow characteristics and low-level SR flow that could influence the thermodynamic and kinematic characteristics of these updrafts.

The raw variables used to characterize the near-storm environments of the analyzed storms are shown in Appendix Table C.2.[4] A number of preexisting derived metrics were also considered, including STP-T03, fixed-layer STP as defined in SHARPpy (STP-F; Blumberg et al. 2017), STP-F appended with an SBCIN scaling term (STP-FCIN), STP-E, and effective layer STP with 0-500 m SRH (STP500; Coffer et al. 2019). An alternate version of STP500 is also tested (denoted STP500*), in which the EIL base criteria is loosened such that the metric is only set to zero if the majority of the EIL lies outside the 0-500 m layer (i.e., effective inflow base, or Eff Base > 250 m). Also tested were the Craven-Brooks significant severe parameter (Sig-Sev; Craven et al. 2004), energy helicity index utilizing MLCAPE and SRH3 (EHI; Hart and Korotky 1991), enhanced stretching potential (ESP; Blumberg et al. 2017), SCP, CIN-scaled SCP (CSCP; Gropp and Davenport 2018), SHERBE and SHERBS3 (Sherburn and Parker 2014), and theta-E index (TEI) to diagnose potential instability (Blumberg et al. 2017). It is worth noting that the primary purpose of these non-STP parameters is not to distinguish between nontornadic and tornadic environments, so comparisons with STP parameters must be taken with that consideration in mind.

In order to assess the skill of each variable in distinguishing between tor/sigtor and nontor events, the true skill statistic (TSS; Wilks 2011) is computed over a range of thresholds, following

$$TSS = \frac{ad - bc}{(a+c)(b+d)} \tag{3.1}$$

where a represents the sum of correct tor/sigtor forecasts, b represents the sum of incorrect tor/sigtor forecasts, c where a represents the sum of correct tor/sigtor forecasts, b represents the sum of incorrect tor/sigtor forecasts, c represents the sum of correct nontor forecasts, and d represents the sum of incorrect nontor forecasts. A more detailed description of this process is shown in Fig. 3.11. Given that TSS calculations are prone to “hedging” when used to predict too rare of events (Doswell et al., 1990), categories are only considered if their non-event to event ratio (i.e., nontor to tor/sigtor) does not exceed 10:1. Heidke skill scores (Wilks 2011) were also computed,

---

[4] Storm-relative (SR) flow for categories including supercells are computed using Bunkers right mover storm motion vector (Bunkers et al. 2000), whereas QLCS-specific categories use Corfidi downshear vector (Corfidi 2003). SRH, however, is uniformly computed relative to the Bunkers RM vector.

and similar predictors were identified, albeit with lower skill scores.

Table 3.3 contains the highest raw and derived-variable TSS magnitudes associated with HSHC and HSLC tor environments and their predominant modes, and associated variable thresholds. Bolded values indicate a variable whose maximum TSS value was negative, implying that there is maximized skill for values *less* than the provided threshold. In general, HSLC TSS values are uniformly lower than HSHC values, consistent with previous studies (e.g., Anderson-Frey et al. 2019) noting the decreased predictability of HSLC tornadoes (relative to HSHC tornadoes). This lack of predictability is most evident for HSLC QLCS tornadoes. SRH1 shows the most skill of the tested SHR and SRH quantities across almost all categories, while SB/MLLCL shows the most consistent skill amongst thermodynamic variables. The remaining HSHC predictors mostly comprise other low-level dynamic variables, whereas HSLC categories contain a number of thermodynamic variables including precipitable water (PW) and DCAPE (and perhaps 700-500 hPa lapse rate, LR75, by extension) — consistent with earlier discussion regarding HSLC Post storm environments (Appendix Fig. C.3). HSLC supercells are specifically predicted by both SBCAPE and 0-3 km CAPE (3CAPE) as well as Eff Base, while HSLC QLCSs are predicted by Eff/MLCIN. Regarding derived variables, STP-T03 is the best tornadic discriminator across all HSHC categories, as well as for HSLC QLCS, with other STP parameters (namely STP-E and STP500) and SCP also showing consistent skill. Fixed-layer STP quantities, especially STP-FCIN, are useful HSLC predictors, perhaps due to the HSLC CIN patterns presented earlier (Fig. 3.4).

Table 3.4 contains the same information as Table 3.3, but instead distinguishing between sigtor and nontor environments. Nearly all categories, regardless of environment, show 0-500 m, 0-1 km, 0-3 km, and effective shear and SRH as valuable sigtor predictors. Deep-layer shear (SHR6) and 0-1 km SR flow only show predictive strength for HSHC environments, while SBCAPE, Eff Base, and PW show unique skill across both HSLC categories. In terms of modal patterns, 0-500 m quantities take on greater relative importance for supercells (compared to overall categories) and increased 0-1 km lapse rate (LR1) shows specific skill for HSLC supercells. Similar to the tor results, STP-T03 is generally the most skillful derived metric, with STP-F also providing skill for HSLC supercells. These results highlight that traditional STP metrics still have forecasting value for the Southeast, even in HSLC environments. That being said, their most skillful values are below standard guidance (i.e., STP ~ 1), as previously noted in Sherburn and Parker (2014). For both tor and sigtor (particularly HSLC categories), STP500* outscores the original STP500 formulation, possibly due to the fact that while lower Eff Base is a tornadic predictor, this within itself implies Eff Base values greater than zero. Furthermore, while SHERBE and SHERBS3 have superior skill discriminating between significant severe and non-severe HSLC environments (their intended purpose), they do not improve on STP metrics in distinguishing between HSLC tor/sigtor and nontor environments.

Comparing Tables 3.3 and 3.4, we see a shift from more thermodynamic tor predictors to more kinematic sigtor predictors, with HSHC sigtor predictors comprised entirely of deep-layer and low-level shear and SRH quantities. HSLC sigtor categories still maintain some of the thermodynamic predictors from Table 3.3, such as PW, SBCAPE, and Eff Base, but low-level shear and SRH quantities have now superseded these variables in predictive skill. Overall, TSS scores for sigtor predictors are higher than those of the tor predictors, as expected given that the tor category includes environments of weak (i.e., F/EF0-1) tornadoes, which have been shown to more strongly resemble nontornadic environments (Thompson et al. 2003). Both the HSHC and HSLC subsets of QLCS sigtors are not shown since they violate the event ratio criteria discussed earlier, but they share the same general predictors as the QLCS results in Table 3.3 with a skew towards SRH quantities (especially SRH3 and Eff SRH). Despite the overall improvements in sigtor prediction using SRH500 in Coffer et al. (2019), only HSLC supercell shows SRH500 as the highest ranked SRH variable. Moreover, the original formulation of STP500 only shows enhanced skill in HSHC environments, and is outperformed by the alternate formulation in every presented tor/sigtor category. If we consider the thresholds of the presented variables, we see that for both tor and sigtor environments nearly all shear and SRH quantities show noticeably higher thresholds for HSLC categories (relative to HSHC categories), again highlighting the importance of low-level dynamic support for HSLC tornadogenesis. This is particularly intriguing for Eff SRH, given that the low

CAPE constraint corresponds to shallower EILs and lower equilibrium level heights, which would act to reduce Eff SRH (all else held constant).

We also considered the TSS results for a given mode and/or environment across each temporal period (Appendix Tables C.3-C.7), in order to see if the variables relevant to tornadogenesis change as a function of time (e.g., thermodynamic variables become more relevant as environmental CAPE decreases). However, the interpretation of these results is made difficult by the diurnal CAPE and shear trends shown earlier (Figs. 3.2-3.9) and associated changes in environment and mode (Figs. 3.10c-f). For instance, if we consider the evolution of predictors, they resemble supercell/HSHC predictors in the pre-transition, but look increasingly like HSLC/QLCS predictors by the post-transition. Classifying further by time, environment, and mode, though scientifically interesting, limits sample size such that TSS results become dubious. Therefore, it is best to only consider the environment-mode combinations presented, with the foreknowledge that they inherently carry some temporal information.

The final question that remains is whether the prediction of SE tornadoes can be advanced by way of these TSS results. To this end, we construct a number of new STP parameters for each of the four categories shown in Table 3.4, as well as QLCS tornado parameters (since no QLCS sigtor categories met our event ratio criteria). As we are not partitioning our data into separate training and verification subsets, 5-fold cross validation[5] is performed to ensure that the initial TSS results are not simply a byproduct of this particular dataset, and can instead generalize to other tested datasets (in this case, subsamples of the original data). This process is accomplished by randomly sampling 80% of the reports for a given category, computing associated TSS and threshold values, and constructing the parameter using the most skillful variables. Correlation analysis is performed on the variables considered for each parameter to ensure they are independent, with the exception of low-level SRH and deep-layer shear. Note that CAPE variables largely do not appear in these new parameters as a result of already partitioning between low and high CAPE. If the top ranked

---

[5] 10-fold cross validation was also tested. The resulting variable rankings were virtually identical to those identified with 5 folds, but the limited size of the testing dataset led to large variability in the performance of the metrics constructed with these rankings.

variables change between folds (i.e., a different SRH quantity ranks highest), they are also tested, and the more skillful variable is retained. These variables are then normalized using optimal thresholds motivated by the TSS analysis, such that parameter values ≥ 1 represent increased likelihood of their associated hazard. This parameter is then tested on the remaining 20% of the reports for each fold to determine its performance metrics. Both the training and testing report subsets associated with each fold are required to meet the established event ratio criteria.

Following the design of previous STP metrics, such as STP-T03 and STP-E, all deep-layer shear terms (e.g. SHR6, Eff SHR) in the resultant parameters are capped at a value of 1.5[6]. Also following the treatment of LCL and CIN terms in previous STP metrics, all thermodynamic terms are capped at a value of 1 and negative values are set to 0 (unless otherwise stated). The HSHC parameter is as follows:

$$\text{STP (HSHC)} = \frac{\text{SRH1}}{250\ m^2\ s^{-2}} \times \frac{\text{SHR6}}{27.5\ m\ s^{-1}} \times \frac{1500 - \text{SBLCL}}{1000\ m} \times \frac{1500 - \text{DCAPE}}{750\ J\ kg^{-1}} \tag{3.2}$$

The HSHC supercell (SC) version of this STP is similar, except the DCAPE term is removed and the SRH1 and SHR6 thresholds are adjusted to 225 $m^2 s^{-2}$ and 30 ms^{-1}, respectively. The HSLC STP parameter substitutes Eff SHR for SHR6 and adds SBCAPE and PW terms, as follows[7]:

$$\text{STP (HSLC)} = \frac{\text{SRH1}}{325\ m^2\ s^{-2}} \times \frac{\text{Eff SHR}}{25\ ms^{-1}} \times \frac{\text{SBCAPE}}{150\ J\ kg^{-1}} \times \frac{\text{PW}}{1.4\ g\ kg^{-1}} \tag{3.3}$$

The HSLC SC STP substitutes SRH500 for SRH1 and replaces SBCAPE with Eff Base, simplifying as follows [8]:

$$\text{STP (HSLC SC)} = \frac{\text{SRH500}}{200\ m^2\ s^{-2}} \times \frac{500 - \text{Eff Base}}{250\ m} \times \frac{\text{PW}}{1.4\ g\ kg^{-1}} \tag{3.4}$$

---

[6] Note that there is no explicit lower bound for this shear term, since our CAPE/shear classification implicitly sets a lower bound.

[7] The SBCAPE term is capped at 2.

[8] The Eff Base term is set to zero for Eff Base > 250 m, as in our formulation of STP500*.

The construction of the HSHC and HSLC QLCS tor parameters (HSHC-Q and HSLC-Q, respectively) was less straightforward, given the inherently decreased predictability of these phenomena, with few variables providing consistently high skill. For HSHC-Q, a simple combination of SRH1 and and MLLCL proved most skillful, as follows:

$$\text{HSHC-Q} = \frac{\text{SRH1}}{275\ m^2\ s^{-2}} \times \frac{2000 - \text{MLLCL}}{1400\ m} \tag{3.5}$$

HSLC-Q retains the LCL term (with adjusted thresholds), but adds PW and DCAPE[9], as follows:

$$\text{HSLC-Q} = \frac{1600 - \text{MLLCL}}{1000\ m} \times \frac{1200 - \text{DCAPE}}{800\ J\ kg^{-1}} \times \frac{\text{PW}}{1.4\ g\ kg^{-1}} \tag{3.6}$$

Figure 3.12 shows the performance diagram (Roebber 2009) containing the POD and success ratio (1-FAR) corresponding to these new metrics, as well as the top pre-existing metrics for each of the analyzed categories (as shown in Tables 3.3-3.4). Comparisons between the TSS values, area under curve (AUC) values associated with the receiver operating characteristic (ROC; Mason 1982) curves, and probability of false detection (POFD) for these metrics are also included. The new HSHC STP metrics show minimal improvement over STP-T03, which is not entirely surprising given that most existing STP metrics have been formulated with this sort of environment (e.g., ample instability and shear) in mind. HSLC STP shows marked improvement, with both increases in POD, success ratio and TSS, and decreases in POFD. Both QLCS parameters show increases in POD (and by extension, TSS), though no appreciable change in success ratio.

3.4 Discussion and conclusions

3.4.1 Summary of results

Now that we have examined the evolution of SE nocturnal storm environments and the predictability of their tornadoes, we will revisit the questions we set out to address within the context

---

[9] All thermodynamic terms in both HSHC-Q and HSLC-Q are capped at a value of 1.

of the literature. The first of these was simply: how do storm environments evolve across the EET? When severe convection persists across the EET, its associated environment typically displays a gradual decrease in CAPE (Fig. 3.2a-i) and an increase in static stability (Fig. 3.4), accompanied by increases in low-level shear and SRH (Fig. 3.3). However, the shape and magnitude of these trends can vary as a function of the average CAPE/shear characteristics in the near-storm environment. When the pre-transition or EET environments exhibit HSLC conditions, associated storm environments tend to exhibit larger deep-layer shear and low-level shear/SRH values for the remainder of the day relative to HSHC environments. Furthermore, many of these HSLC environments actually destabilize as the evening progresses, which along with associated CAPE increases resemble the evolution detailed in King et al. (2017). These CAPE increases and CIN magnitude decreases are strongly correlated with increases in low-level θ_e and LR1 (Appendix Fig. C.1), respectively, which underscore the importance of low-level warm air and/or differential advection (as in King et al. 2017) and steepened low-level lapse rates (as in Sherburn and Parker 2014) for HSLC storm maintenance. The sum total of these factors likely play a compensatory role given reduced instability, allowing HSLC convection to persist and produce hazards well into the evening. However, some of these compensating factors were primarily attributed to QLCS modes (Fig. 3.6-3.8), such that the factors contributing to HSLC supercell maintenance are less clear.

We also explored how environmental variables evolve when severe convection fails to persist into and past the EET to determine what factors potentially govern nocturnal storm maintenance. Days in which severe convection persisted into and through the EET show initially larger shear and SRH values (Figs. 3.9d-f), as well as slower decreases in CAPE (Figs. 3.9a-c) and slower increases in CIN magnitude (Figs. 3.9g-i, particularly ML/MUCIN) across the EET. These results share some similarities with the findings of Gropp and Davenport (2018) (cf. their Fig. 9), suggesting that these observations regarding nocturnal storm maintenance may hold true in broader sense for different storm modes and geographical regions.

Our next question asked whether the presented environmental evolution can influence the prevalence and convective mode of tornadoes. HSLC pre-transition conditions were found to initially suppress tornadoes, but increase the prevalence of tornadoes later in the day (Fig. 3.5a), possibly in response to associated SRH and CIN patterns. With respect to mode, HSHC conditions generally favor supercellular tornadoes, while HSLC conditions in a given period increasingly favor the prevalence of QLCS tornadoes later that day (Fig. 3.5d-f). Similar results hold true even when severe convection fails to persist through the EET, with an uptick in HSLC and QLCS tornadoes into the evening hours (Fig. 3.10c-f). These findings highlight that CAPE/shear characteristics in a given period can influence the tornado characteristics not only then, but also during subsequent periods.

We then examined which near-storm environment variables most effectively discriminate between tor/sigtor and nontor storm environments. Regardless of environment or mode, low-level shear/SRH quantities (and by extension, SR flow) are consistently skillful predictors for tor/sigtor (Tables 3.3-3.4, respectively), as expected. HSLC tornadoes are specifically predicted by moisture-related variables, including increased PW and decreased DCAPE. The former indicates an increase in local moisture, which has been shown in studies such as Mead and Thompson (2011) to preclude the formation of near-surface stable layers via advection of higher θ_e air by the LLJ (as in Maddox 1983). This slowed CIN development — perhaps related to the presented destabilization of HSLC environments (Fig. 3.4a-b) — would facilitate storm maintenance into evening hours (Gropp and Davenport 2018), thus increasing the likelihood of nocturnal tornadogenesis (Mead and Thompson 2011).

Interpretation of the latter, DCAPE, is less straightforward. Decreased DCAPE may be related to reduced evaporation (perhaps aided by the local moisture enhancements discussed earlier) and less negatively buoyant outflow, though we must be careful drawing direct comparison between the two due to entrainment effects (Gilmore and Wicker 1998). Such a relationship would be physically plausible, given the favorable influence of less negatively buoyant outflow on supercell tornadogenesis (e.g., Markowski et al. 2002; Shabbott and Markowski 2006), primarily by making it easier for near-surface parcels to be dynamically lifted. Furthermore, this prevents outflow from undercutting low-level circulations and reducing the ability of their associated dynamic pressure accelerations to stretch and converge near-surface rotation (Markowski and Richardson 2014; Brown and Nowotarski 2019). Even for non-supercellular tornadoes, less negatively buoyant outflow may allow QLCS updrafts to remain upright rather than sloping back over their attendant cold pools (Rotunno et al. 1988), a crucial ingredient for QLCS tornadogenesis (e.g., Schaumann and Przybylinski 2012; Williams et al. 2018). That being said, the exact relationship between observed HSLC cold pool deficits and tornadogenesis remains unclear (McDonald and Weiss 2021). In addition to the aforementioned variables, HSLC tornadic supercells also exhibit increased LR1 consistent with previous HSLC studies (e.g., Sherburn and Parker 2014; Sherburn et al. 2016), along with lowered Eff Base and increased SBCAPE and 3CAPE. These findings imply that with reduced environmental instability, SE tornadogenesis becomes particularly sensitive to low-level thermodynamic characteristics and the ability for storms to remain more surface-based.

In terms of existing forecasting metrics, STP-T03 shows the highest skill for both tor and sigtor across nearly every environment-mode combination. This is somewhat surprising, given that more recent iterations of STP incorporating effective-layer quantities and SRH500 are generally thought to be improvements upon this original STP formulation. That said, Table 3.4 in Coffer et al. (2019) indicated that the second lowest skill for STP500 was across the lower MS Valley (LVM), so this insight is consistent with past work. For HSLC supercells, STP-F and STP-FCIN are effective predictors, due perhaps to their inclusion of more surface-based quantities (SBLCL and SBCAPE). Finally, a number of new STP and QLCS tor metrics were also developed. Admittedly, there is minimal room for such improvement with HSHC categories, since most STP parameters are designed for prototypical convective environments with appreciable shear and instability. Noticeable improvements can be made, however, for HSLC/HSLC SC sigtor categories with the addition of predictors such as PW and Eff Base. Note that these parameters have only been constructed and evaluated numerically. More in depth analysis, including a 2D spatial assessment of these new parameters relative to traditional STP parameters and observed storm reports, is necessary before such parameters can reliably be put into practice. In particular, one needs to consider that these new parameters are conditioned on the occurrence of storms within specific

CAPE regimes, and therefore could incur large false alarm rates if applied blindly.

3.4.2 Considerations and limitations

As with any study using near-storm model soundings as a proxy for observations, there are a number of limitations that must be considered. First is the potential for error in the sounding-derived data ascribed to each severe convective report. These errors could stem from the underlying model output, such as the near-surface cool and dry biases of the RUC model, which can lead to underestimates of CAPE on the order of 100-250 J kg^{-1} (e.g., Thompson et al. 2003, their Fig. 3). Similar magnitude variability in CAPE calculations can also result from the method used to lift parcels and compute their θ_e upon saturation. For instance, Coffer et al. (2019) noted that CAPE values computed with NSHARP/SHARPpy — like those used in this study — tend to be higher than most other computational methods, particularly for high CAPE soundings. Both sources could introduce uncertainty into the CAPE/shear classification of individual reports, as well as our characterization of CAPE and CIN evolution. Overestimates of CAPE would lend confidence to our characterization of low-CAPE environments but bring into question our high-CAPE classification (and visa versa with underestimates). Though worth consideration, the design of our two environmental categories helps limit this uncertainty. For instance, if we perturb our calculated CAPE values by the maximum error bound in the above literature (250 J kg^{-1}), less than 1% of the cases in either category switch classification (e.g, HSHC switching to HSLC, or visa versa).

There are also potential spatiotemporal errors associated with the mesoanalyses utilized. The 40-km spacing and hourly time step could ascribe inaccurate data to reports occurring near tight gradients (e.g., baroclinic zones), and also smooth out relevant small scale features like the narrow bands of moist instability shown in King et al. (2017) to be important for sustaining HSLC convection. For studies like this compositing environments across large report samples, the net impact of the discussed biases may ultimately be small (e.g., Thompson et al. 2003; Thompson et al. 2012), but it is important to understand that the statistic robustness afforded by larger datasets does not always translate to practical relevance for forecasting, as noted in Anderson-Frey et al. (2016).

From a methodology standpoint, there is a great deal of subjectivity when applying fixed CAPE/shear environmental thresholds. Though physically motivated, the HSHC/HSLC definitions developed herein (and in the literature) are somewhat arbitrary constructs used to isolate and analyze unique subsets of the storm climatology. Both represent only portions of a much broader CAPE/shear parameter space in which Southeast severe convection and tornadoes can exist (e.g., Anderson-Frey et al. 2019, their Fig. 2a), as demonstrated by the uniformly favorable impact of high-shear, moderate-CAPE conditions for tor/sigtor prevalence noted in Section 3b. Furthermore, the CAPE values which qualify as "high" or "low" vary by (and even within) geographical regions (Thompson et al., 2013). Also worth consideration is our EF2+ cutoff for significant tornadoes. Though largely consistent with previous observational tornado studies, its utility for the SE tornado climatology is debatable. Thompson et al. (2017), particularly their Fig. 14, demonstrated that low-level rotational velocities are approximately 10 kt lower in MS/AL for the same EF-scale ratings compared to the Great Plains, perhaps due to the relative lack of potential damage indicators in much of the Great Plains, with some accompanying potential for tornadoes to be under-rated by the EF-scale (away from urban areas). As such, a stricter significant tornado criteria of EF3+ might be warranted for the SE to help avoid the conflation of some weak and significant tornadoes. For instance, roughly 93% of the QLCS sigtors identified by our original criteria have an EF-2 rating. This helps to explain their inherent lack of predictability, but it also suggests that QLCS tornadoes may be a less impactful portion of the overall SE tornado climatology than commonly thought, particularly given the aforementioned potential for biases in damage ratings in this region.

3.4.3 Future work

There are numerous avenues for future research that would build upon and contextualize the results presented in this study. For instance, it might prove useful to repeat similar analyses for other geographical regions in order to gauge the uniqueness of our SE results, and help advance a unified theory regarding the storm maintenance and tornadogenesis potential of storms persisting across the EET. Breaking the presented analyses down by season may also reveal additional findings, given the seasonal variability of SE storm environments shown in Anderson-Frey et al. (2019). Furthermore, numerical simulations could help determine the net impact of the increased low-level SRH and nocturnal destabilization on low-level updraft forcing in HSLC storm environments in spite of overall limited buoyancy. Paired with the base-state substitution (BSS) technique of Davenport et al. (2019), such simulations could provide storm-scale insight into how environmental evolution across the EET influences the dynamical processes relevant for HSLC tornadogenesis.

Table 3.1: Storm report counts for days with severe convection across all three temporal periods, broken down by environmental classification; total counts are provided along with counts attributed to supercell (SC) and QLCS modes. Reprinted from Brown et al. (2021), with permission from American Meteorological Society.

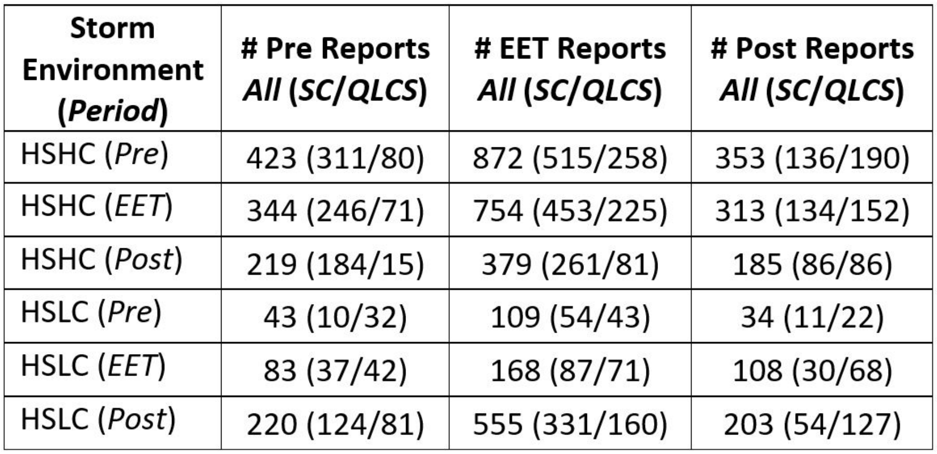

Storm Environment (*Period*)	**# Pre Reports *All* (*SC/QLCS*)**	**# EET Reports *All* (*SC/QLCS*)**	**# Post Reports *All* (*SC/QLCS*)**
HSHC (*Pre*)	423 (311/80)	872 (515/258)	353 (136/190)
HSHC (*EET*)	344 (246/71)	754 (453/225)	313 (134/152)
HSHC (*Post*)	219 (184/15)	379 (261/81)	185 (86/86)
HSLC (*Pre*)	43 (10/32)	109 (54/43)	34 (11/22)
HSLC (*EET*)	83 (37/42)	168 (87/71)	108 (30/68)
HSLC (*Post*)	220 (124/81)	555 (331/160)	203 (54/127)

Table 3.2: Storm report counts for each mutually exclusive temporal category (e.g., Pre, EET, Post, and combinations thereof) in each of their associated periods. Reprinted from Brown et al. (2021), with permission from American Meteorological Society.

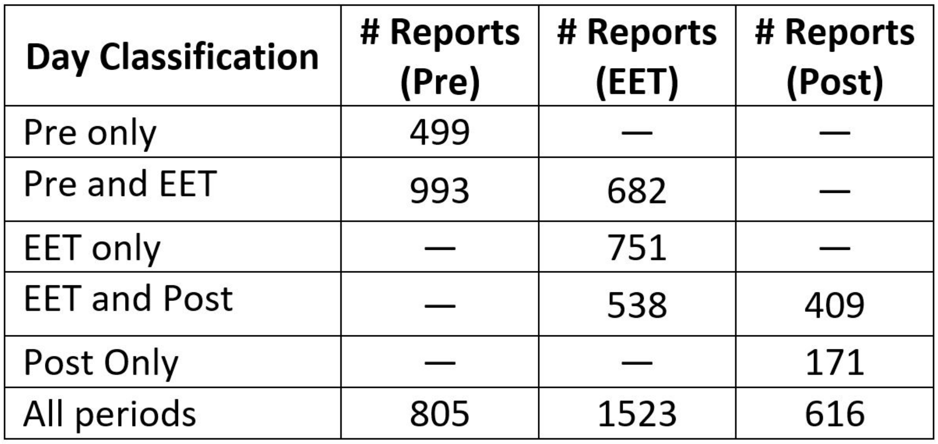

Day Classification	**# Reports (Pre)**	**# Reports (EET)**	**# Reports (Post)**
Pre only	499	—	—
Pre and EET	993	682	—
EET only	—	751	—
EET and Post	—	538	409
Post Only	—	—	171
All periods	805	1523	616

Table 3.3: Environmental (top portion) and derived (bottom portion) tor predictors ranked by maximum TSS magnitude (with associated variable threshold shown in parentheses); bolded values indicate a maximum TSS value whose sign was negative. The variables (and their associated units) are as follows - shear/SR-flow quantities (m s^{-1}), SRH quantities (m^2 s^{-2}), CAPE/CIN quantities (J kg^{-1}), lapse rates (K km^{-1}), LCL/LFC/Eff Base quantities (meters AGL), PW (inches), RH (%), and derived variables (dimensionless). Reprinted from Brown et al. (2021), with permission from American Meteorological Society.

HSHC		HSLC		HSHC Supercell		HSLC Supercell		HSHC QLCS		HSLC QLCS	
SRH1	0.44 (244.9)	**PW**	0.236 (1.4)	**SRH1**	0.439 (201.1)	**PW**	0.264 (1.4)	**SRH1**	0.471 (271)	**PW**	0.227 (1.4)
SHR1	0.414 (13.5)	**DCAPE**	**0.171 (372)**	**SHR1**	0.419 (13.5)	**DCAPE**	**0.212 (511.1)**	**SHR1**	0.471 (15.7)	**MLLCL**	**0.201 (689.8)**
SRH3	0.408 (284.1)	**SRH1**	0.163 (294.3)	**SRH500**	0.378 (132.2)	**SRH1**	0.21 (294.4)	**SRH3**	0.459 (324.2)	**DCAPE**	**0.183 (362)**
Eff SRH	0.389 (242.3)	**SBCAPE**	0.16 (146.1)	**SRH3**	0.373 (284.3)	**LR1**	0.21 (3.8)	**Eff SRH**	0.425 (290.7)	**LR75**	**0.166 (6.2)**
SRH500	0.38 (137.7)	**Eff Base**	**0.158 (15.9)**	**Eff SRH**	0.363 (242.8)	**SBCAPE**	0.202 (15.8)	**MLLCL**	**0.419 (660.7)**	**Eff CIN**	0.144 (-10.6)
SHR500	0.346 (10)	**LR75**	**0.158 (6.2)**	**SHR500**	0.362 (9.6)	**SRH500**	0.197 (164.1)	**SRH500**	0.393 (137.9)	**RH SFC**	0.14 (85.4)
MLLCL	**0.3 (757.3)**	**Eff SRH**	0.158 (285.2)	**SBLCL**	**0.324 (512.1)**	**3CAPE**	0.191 (5.6)	**SHR3**	0.391 (19.9)	**MLCIN**	0.135 (-65.8)
SHR3	0.298 (19.8)	**SRH3**	0.156 (371.3)	**RH SFC**	0.315 (77.8)	**Eff Base**	**0.187 (170.3)**	**SHR500**	0.367 (10.2)	**SBLCL**	**0.133 (434.9)**
SBLCL	**0.284 (512.3)**	**MLLCL**	**0.152 (669.8)**	**MLLCL**	**0.299 (785.3)**	**SHR1**	0.169 (16.4)	**RH SFC**	0.359 (84.1)	**LR85**	**0.128 (6)**
SR500	0.281 (16)	**MLCIN**	0.144 (-62.9)	**LR1**	**0.282 (7.9)**	**SHR500**	0.163 (8.7)	**SBLCL**	**0.32 (456.9)**	**SRH3**	0.124 (384.5)
STP-T03	0.419 (3.6)	**STP-FCIN**	0.233 (0.1)	**STP-T03**	0.398 (3.6)	**STP-FCIN**	0.281 (0.1)	**STP-T03**	0.438 (4.8)	**STP-T03**	0.176 (0.6)
STP-E	0.336 (2.5)	**STP-F**	0.214 (0.1)	**STP500***	0.327 (2.4)	**STP-F**	0.275 (0.2)	**EHI**	0.391 (2.8)	**STP-FCIN**	0.146 (0.1)
STP500*	0.336 (2.6)	**STP-T03**	0.205 (0.8)	**STP500**	0.315 (2.4)	**STP500***	0.202 (0.4)	**SCP**	0.372 (10.8)	**STP500***	0.135 (0.2)
STP500	0.331 (2.6)	**STP500***	0.189 (0.3)	**STP-E**	0.286 (1.9)	**STP-T03**	0.181 (0.8)	**STP-E**	0.355 (2.4)	**STP-F**	0.122 (0.1)
SCP	0.33 (11.6)	**EHI**	0.162 (0.4)	**SCP**	0.284 (13.2)	**EHI**	0.18 (0.6)	**CSCP**	0.353 (10.8)	**CSCP**	0.106 (1.8)

Table 3.4: As in Table 3.3, but for sigtor predictors. Reprinted from Brown et al. (2021), with permission from American Meteorological Society.

HSHC		HSLC		HSHC Supercell		HSLC Supercell		HSHC QLCS		HSLC QLCS	
SRH1	0.44 (244.9)	**PW**	0.236 (1.4)	**SRH1**	0.439 (201.1)	**PW**	0.264 (1.4)	**SRH1**	0.471 (271)	**PW**	0.227 (1.4)
SHR1	0.414 (13.5)	**DCAPE**	**0.171 (372)**	**SHR1**	0.419 (13.5)	**DCAPE**	**0.212 (511.1)**	**SHR1**	0.471 (15.7)	**MLLCL**	**0.201 (689.8)**
SRH3	0.408 (284.1)	**SRH1**	0.163 (294.3)	**SRH500**	0.378 (132.2)	**SRH1**	0.21 (294.4)	**SRH3**	0.459 (324.2)	**DCAPE**	**0.183 (362)**
Eff SRH	0.389 (242.3)	**SBCAPE**	0.16 (146.1)	**SRH3**	0.373 (284.3)	**LR1**	0.21 (3.8)	**Eff SRH**	0.425 (290.7)	**LR75**	**0.166 (6.2)**
SRH500	0.38 (137.7)	**Eff Base**	**0.158 (15.9)**	**Eff SRH**	0.363 (242.8)	**SBCAPE**	0.202 (15.8)	**MLLCL**	**0.419 (660.7)**	**Eff CIN**	0.144 (-10.6)
SHR500	0.346 (10)	**LR75**	**0.158 (6.2)**	**SHR500**	0.362 (9.6)	**SRH500**	0.197 (164.1)	**SRH500**	0.393 (137.9)	**RH SFC**	0.14 (85.4)
MLLCL	**0.3 (757.3)**	**Eff SRH**	0.158 (285.2)	**SBLCL**	**0.324 (512.1)**	**3CAPE**	0.191 (5.6)	**SHR3**	0.391 (19.9)	**MLCIN**	0.135 (-65.8)
SHR3	0.298 (19.8)	**SRH3**	0.156 (371.3)	**RH SFC**	0.315 (77.8)	**Eff Base**	**0.187 (170.3)**	**SHR500**	0.367 (10.2)	**SBLCL**	**0.133 (434.9)**
SBLCL	**0.284 (512.3)**	**MLLCL**	**0.152 (669.8)**	**MLLCL**	**0.299 (785.3)**	**SHR1**	0.169 (16.4)	**RH SFC**	0.359 (84.1)	**LR85**	**0.128 (6)**
SR500	0.281 (16)	**MLCIN**	0.144 (-62.9)	**LR1**	**0.282 (7.9)**	**SHR500**	0.163 (8.7)	**SBLCL**	**0.32 (456.9)**	**SRH3**	0.124 (384.5)
STP-T03	0.419 (3.6)	**STP-FCIN**	0.233 (0.1)	**STP-T03**	0.398 (3.6)	**STP-FCIN**	0.281 (0.1)	**STP-T03**	0.438 (4.8)	**STP-T03**	0.176 (0.6)
STP-E	0.336 (2.5)	**STP-F**	0.214 (0.1)	**STP500***	0.327 (2.4)	**STP-F**	0.275 (0.2)	**EHI**	0.391 (2.8)	**STP-FCIN**	0.146 (0.1)
STP500*	0.336 (2.6)	**STP-T03**	0.205 (0.8)	**STP500**	0.315 (2.4)	**STP500***	0.202 (0.4)	**SCP**	0.372 (10.8)	**STP500***	0.135 (0.2)
STP500	0.331 (2.6)	**STP500***	0.189 (0.3)	**STP-E**	0.286 (1.9)	**STP-T03**	0.181 (0.8)	**STP-E**	0.355 (2.4)	**STP-F**	0.122 (0.1)
SCP	0.33 (11.6)	**EHI**	0.162 (0.4)	**SCP**	0.284 (13.2)	**EHI**	0.18 (0.6)	**CSCP**	0.353 (10.8)	**CSCP**	0.106 (1.8)

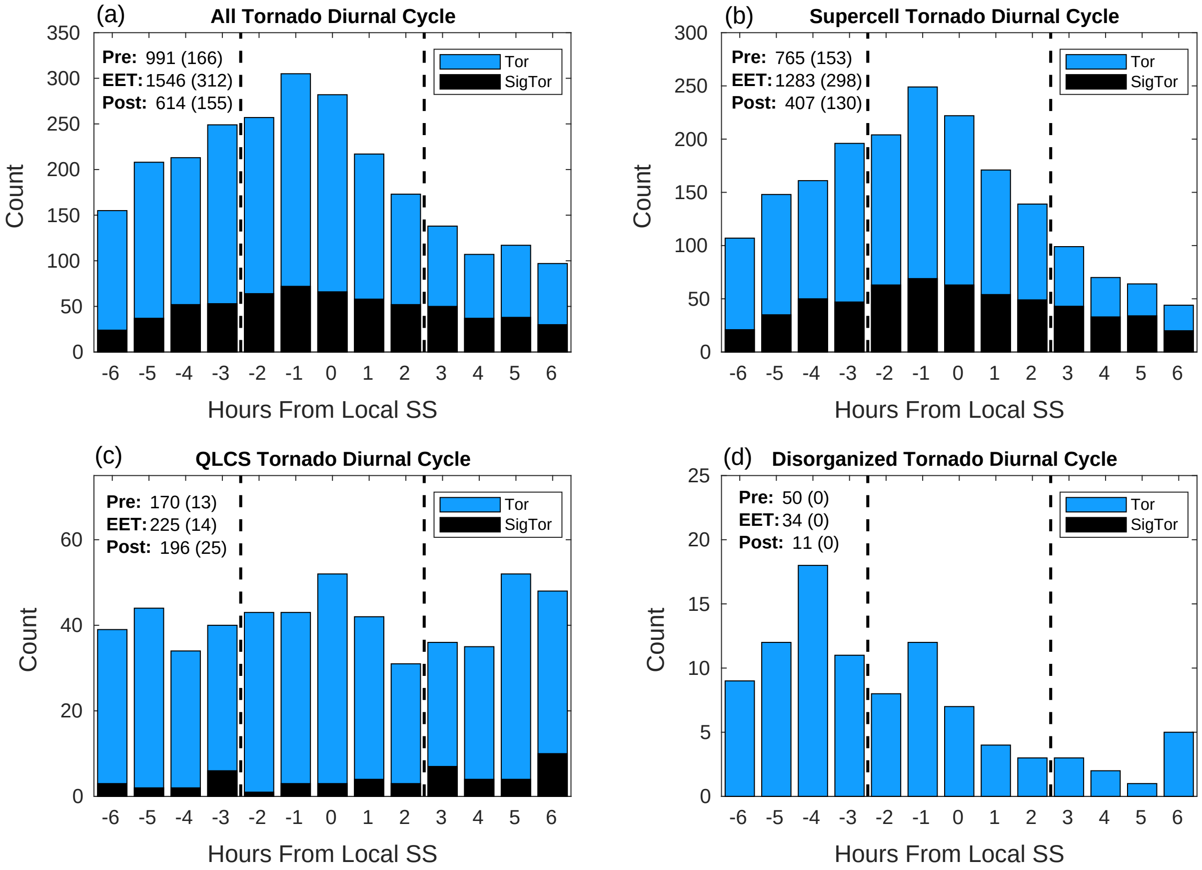

Figure 3.1: Diurnal cycle of tornadoes (in light blue) and sigtors (in black) during the pre-transition, EET, and post-transition for (a) all , (b) supercell, (c) QLCS, and (d) disorganized tornadoes, with the EET bounds delineated by black dotted lines; the number of tornadoes in each period is shown in the top left with and number of sigtors in parentheses. Reprinted from Brown et al. (2021), with permission from American Meteorological Society.

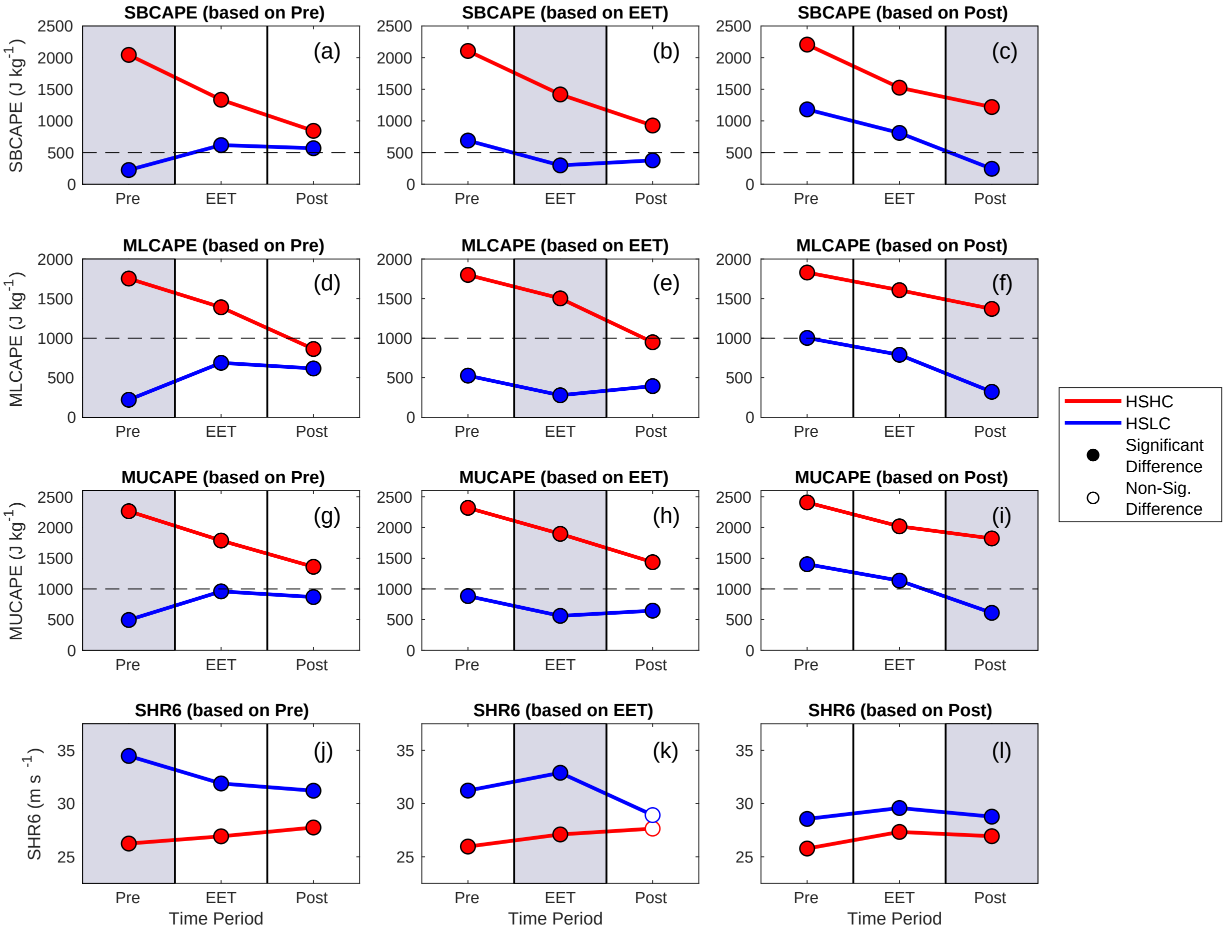

Figure 3.2: Time series of average (a)-(c) SBCAPE (in J kg^{-1}), (d)-(f) MLCAPE (in J kg^{-1}), (g)-(i) MUCAPE (in J kg^{-1}), and (j)-(l) 0-6 km shear (in m s^{-1}) based on environment in the pre-transition (Pre, column 1), early evening transition (EET, column 2), and post-transition (Post, column 3). Gray shading corresponds with the period on which each pattern is predicated, and red and blue lines correspond to HSHC and HSLC environmental classifications, respectively; black dotted lines mark thresholds corresponding to our CAPE classification scheme. Filled (unfilled) data points represent statistically significant (insignificant) differences between HSHC and HSLC patterns in each period, following two-sample *t* tests (at the 95% confidence level). Reprinted from Brown et al. (2021), with permission from American Meteorological Society.

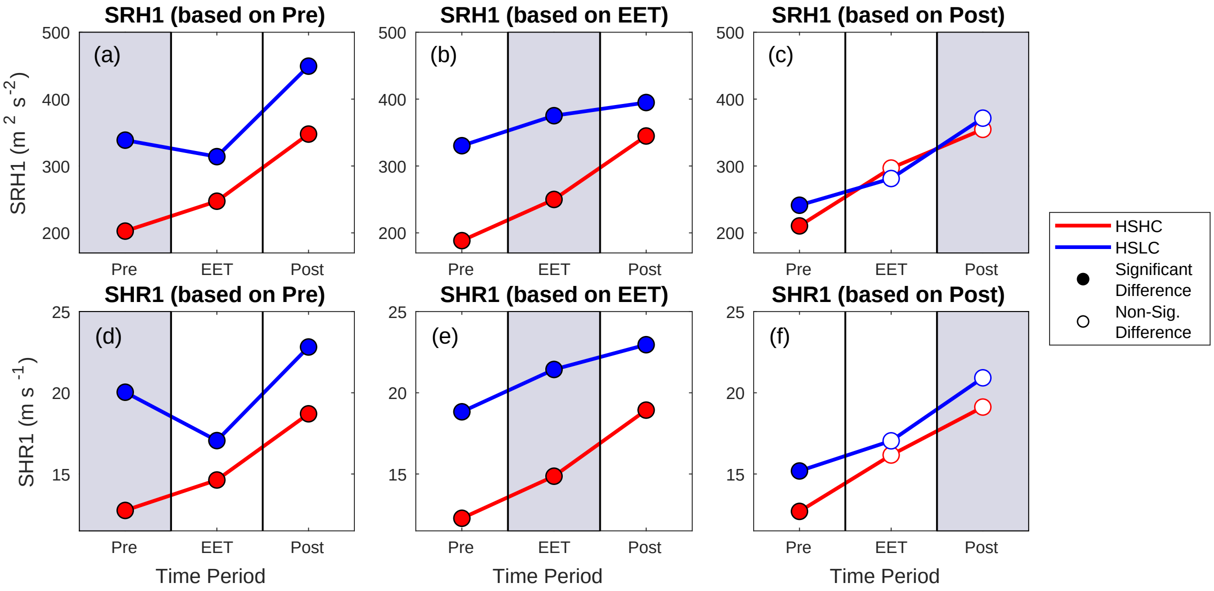

Figure 3.3: Time series of average (a)-(c) SRH1 (in m^2 s^{-2}) and (d)-(f) SHR1 (in m s^{-1}), with the same line/color scheme as Fig. 3.2. Reprinted from Brown et al. (2021), with permission from American Meteorological Society.

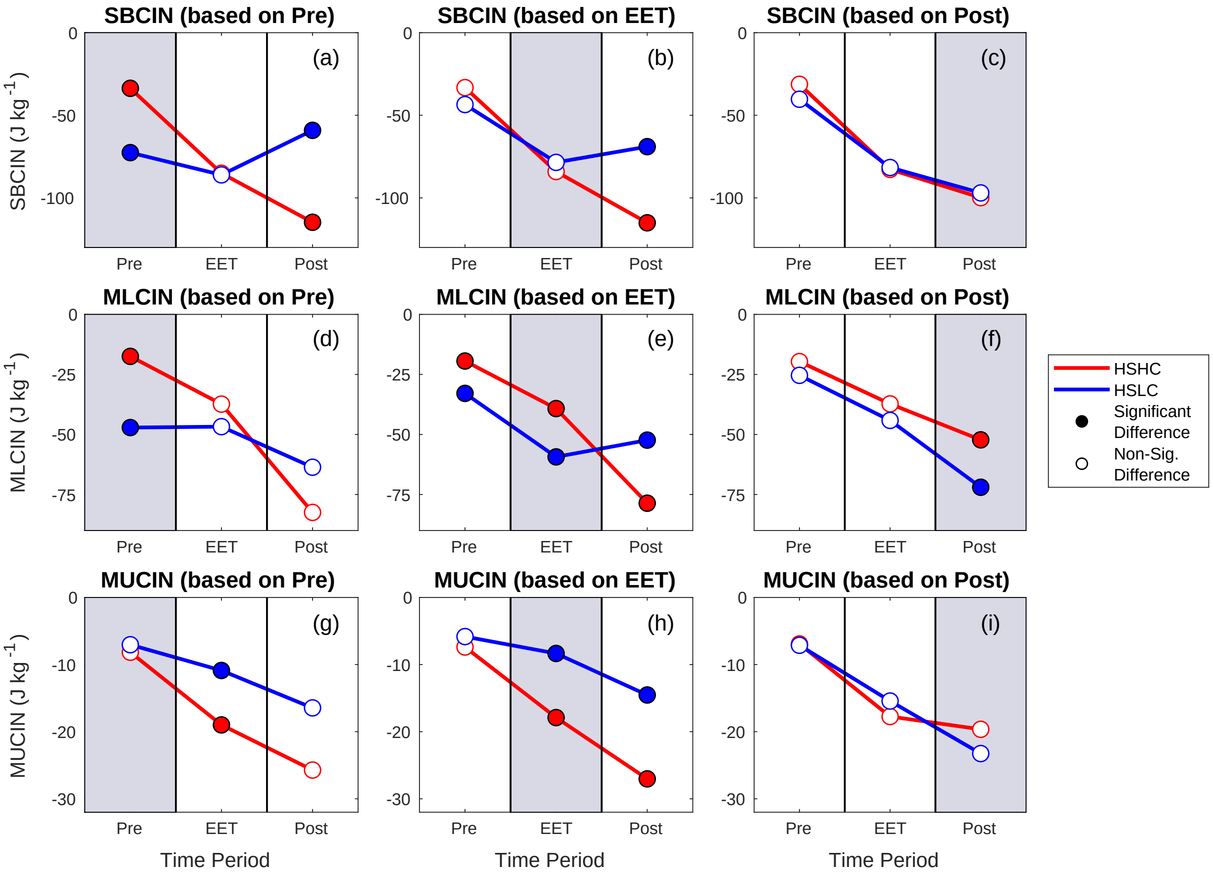

Figure 3.4: Time series of average (a)-(c) SBCIN, (d)-(f) MLCIN, and (g)-(i) MUCIN (all in J kg^{-1}), with the same line/color scheme as Fig. 3.2. Reprinted from Brown et al. (2021), with permission from American Meteorological Society.

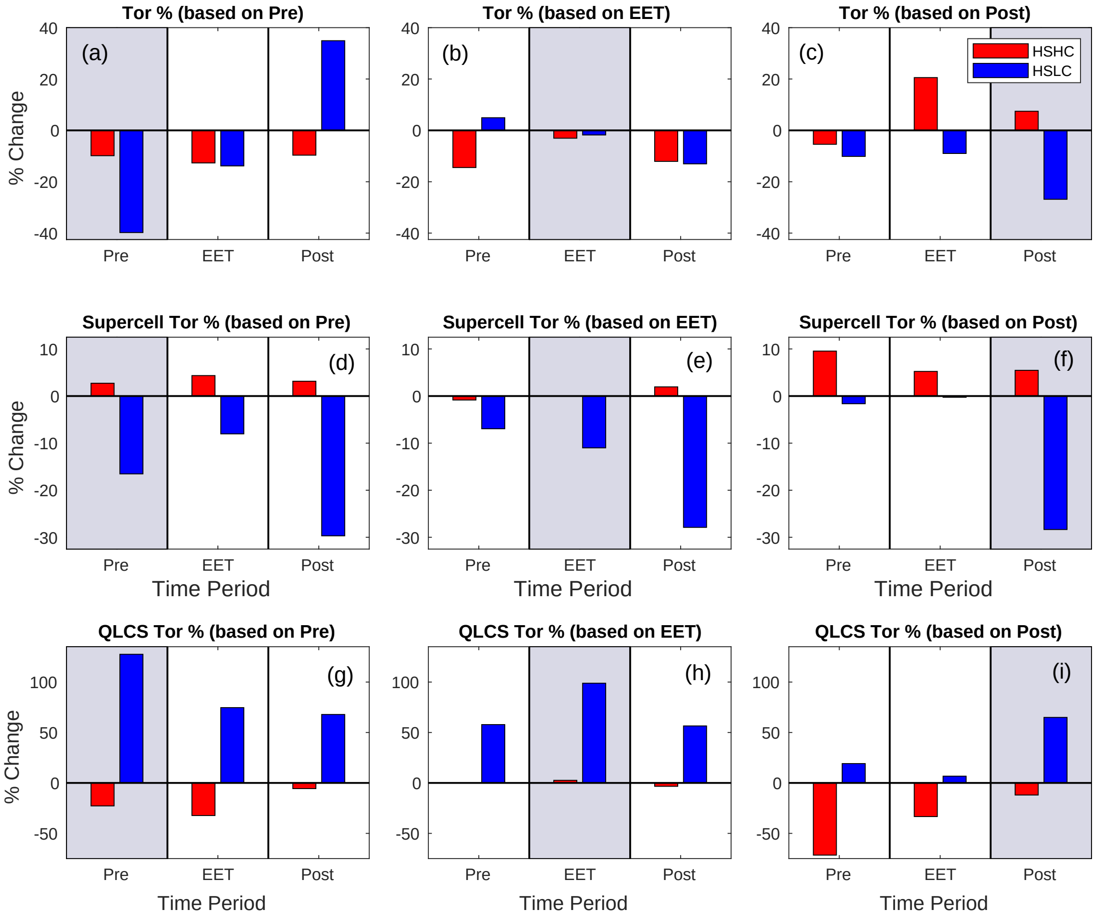

Figure 3.5: Bar plots displaying the percent change (relative to climatological average fraction in each period) of (a)-(c) fraction of storms producing tornadoes and the fraction of those tornadoes occurring within (d)-(f) supercells and (g)-(i) QLCS modes, with the same time classification and color scheme as Fig. 3.2. Reprinted from Brown et al. (2021), with permission from American Meteorological Society.

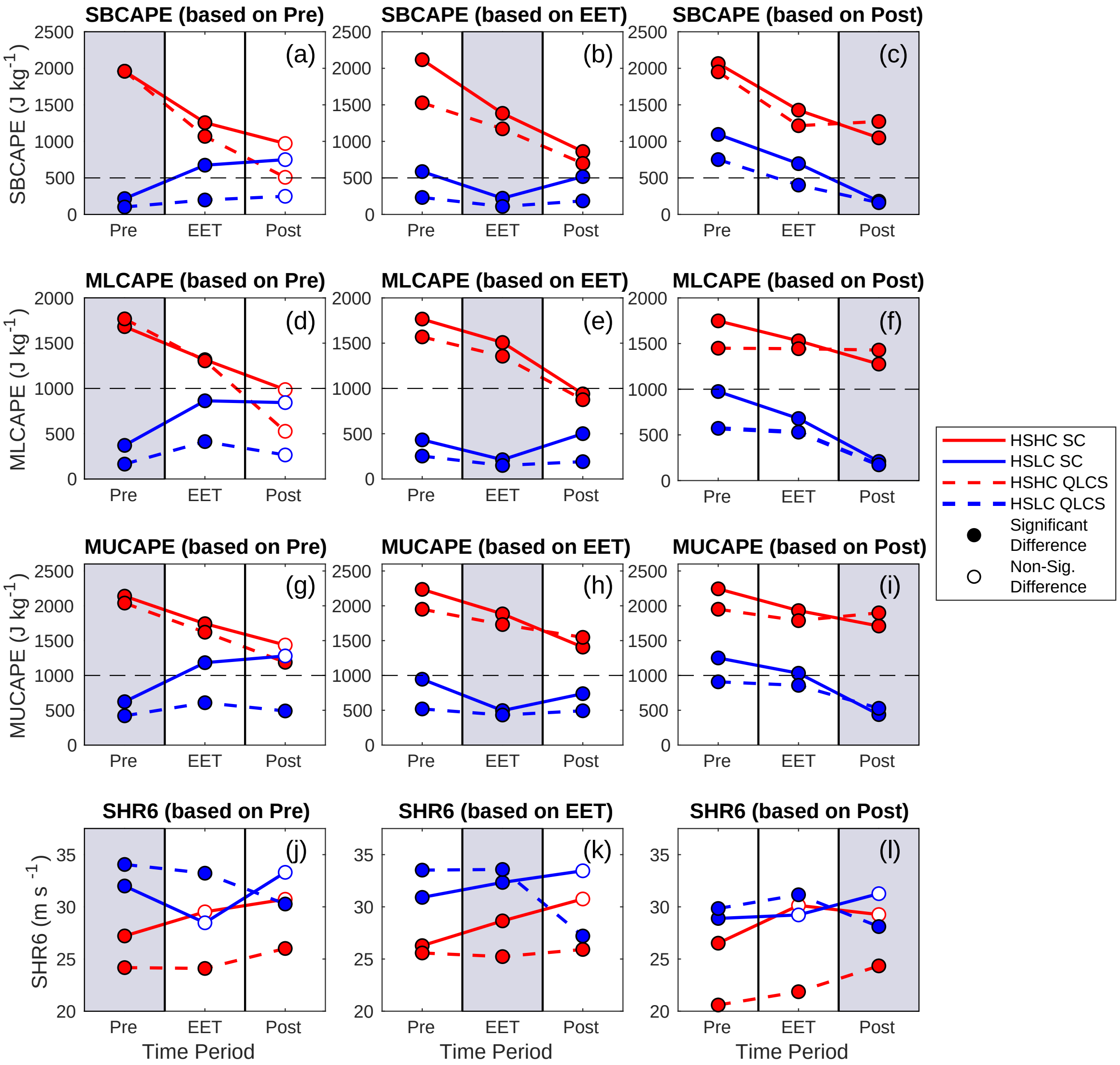

Figure 3.6: Time series of median (a)-(c) SBCAPE (in J kg^{-1}), (d)-(f) MLCAPE (in J kg^{-1}), (g)-(i) MUCAPE (in J kg^{-1}), and (j)-(l) 0-6 km shear (in m s^{-1}), with the same time classification and color scheme as Fig. 3.2, but now broken down by convective mode (solid lines for supercell, or SC, patterns and dotted lines for QLCS patterns). Filled (unfilled) data points represent statistically significant (insignificant) differences between modal HSHC and HSLC patterns in each period, following Mann-Whitney U tests (at the 95% confidence level). Reprinted from Brown et al. (2021), with permission from American Meteorological Society.

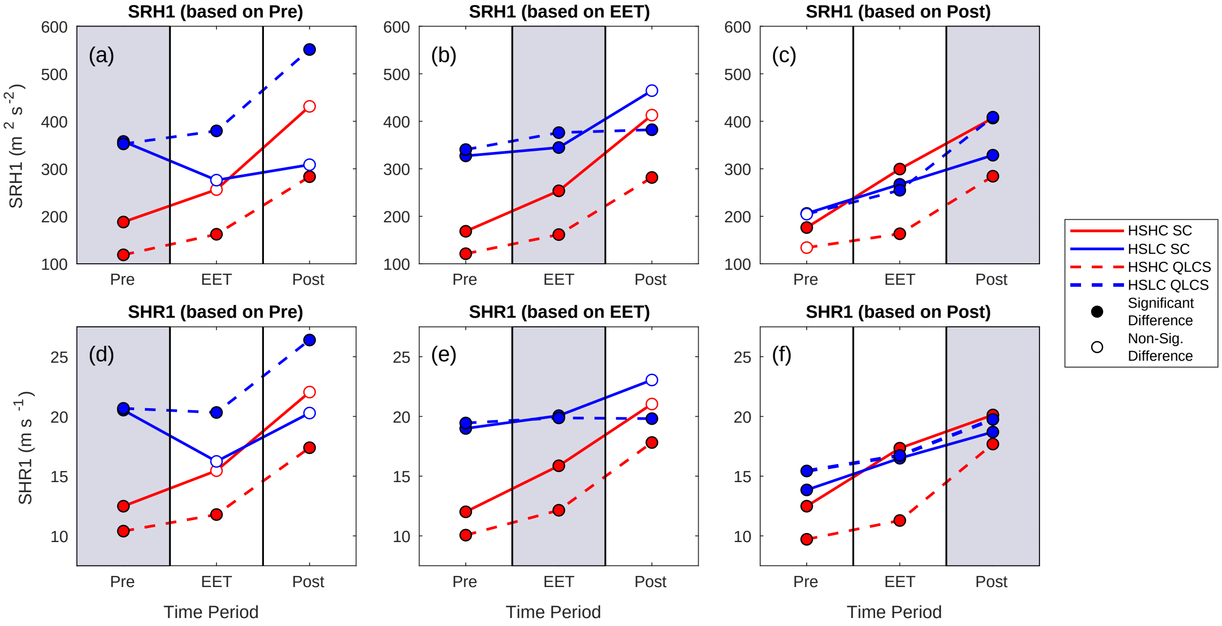

Figure 3.7: Time series of median (a)-(c) SRH1 (in m^2 s^{-2}) and (d)-(f) SHR1 (in m s^{-1}), with the same line/color scheme as Fig. 3.6. Reprinted from Brown et al. (2021), with permission from American Meteorological Society.

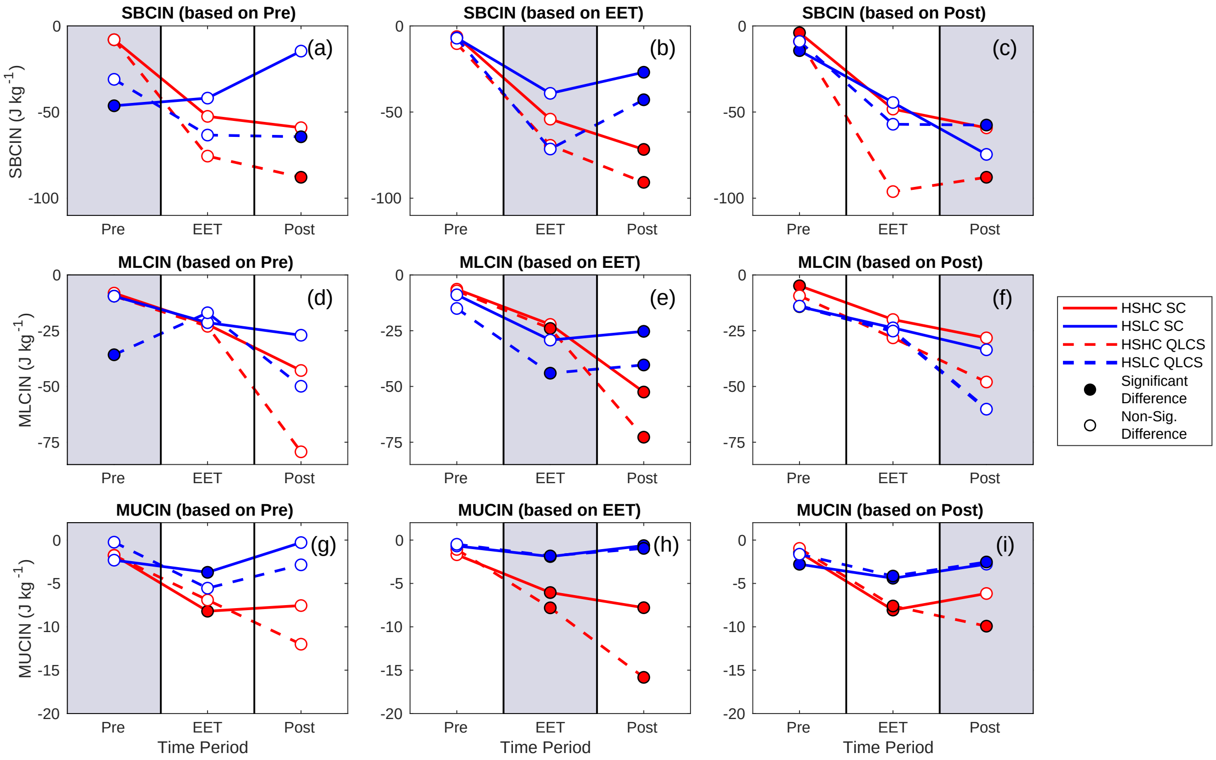

Figure 3.8: Time series of median (a)-(c) SBCIN, (d)-(f) MLCIN, and (g)-(i) MUCIN (all in J kg^{-1}), with the same line/color scheme as Fig. 3.6. Reprinted from Brown et al. (2021), with permission from American Meteorological Society.

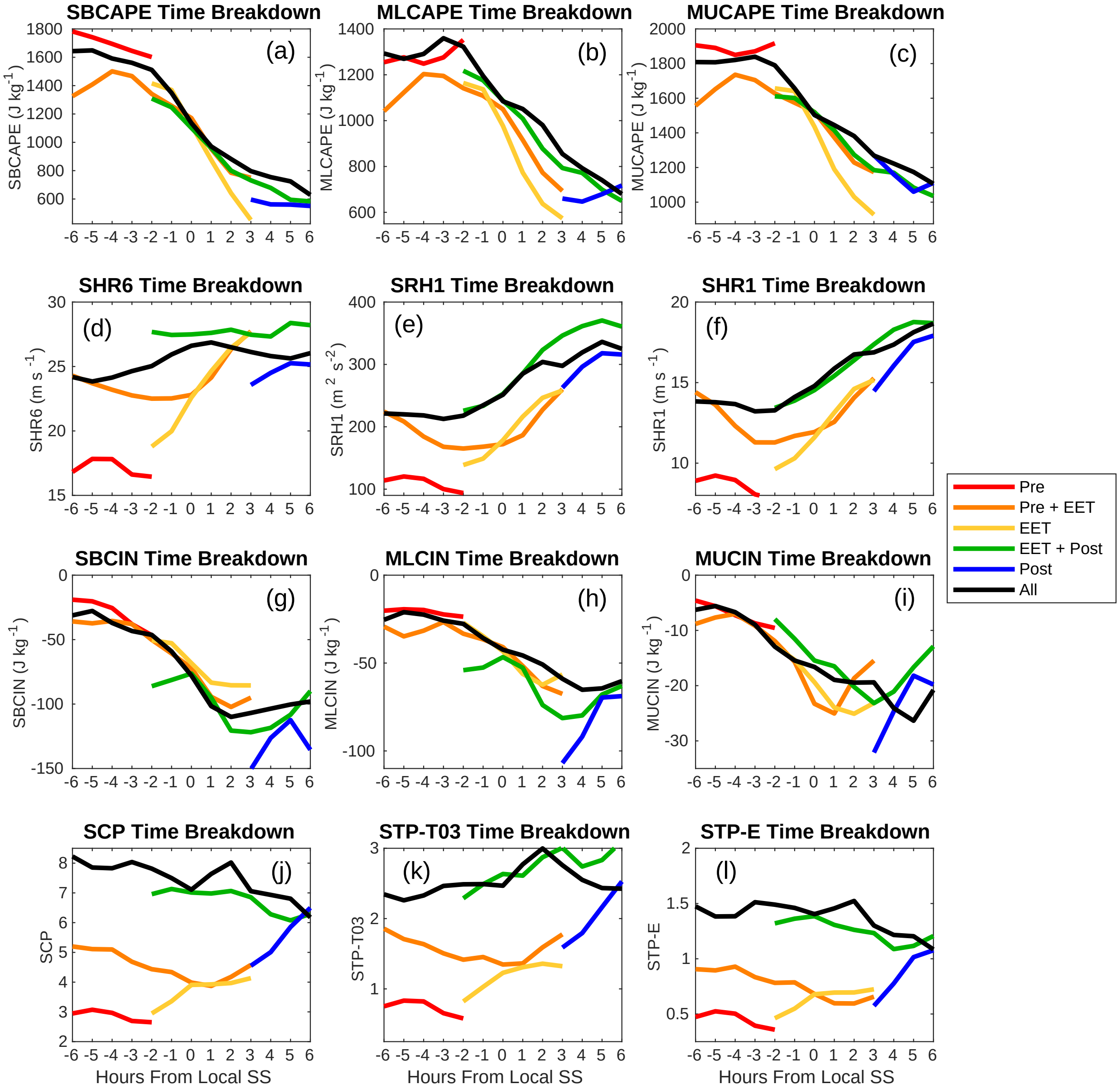

Figure 3.9: Time series of average hourly (a)-(c) SB/ML/MUCAPE (in J kg^{-1}), (d) 0-6 km SHR (in m s^{-1}), (e) 0-1 km SRH (in m^2 s^{-2}), (f) 0-1 km SHR (in m s^{-1}), (g)-(i) SB/ML/MUCIN (in J kg^{-1}), (j)-(k) SCP, STP-T03, and STP-E (all unitless), respectively, corresponding to each of the analyzed temporal categories. A 2-hr moving average is applied to smooth the hourly mean data. Reprinted from Brown et al. (2021), with permission from American Meteorological Society.

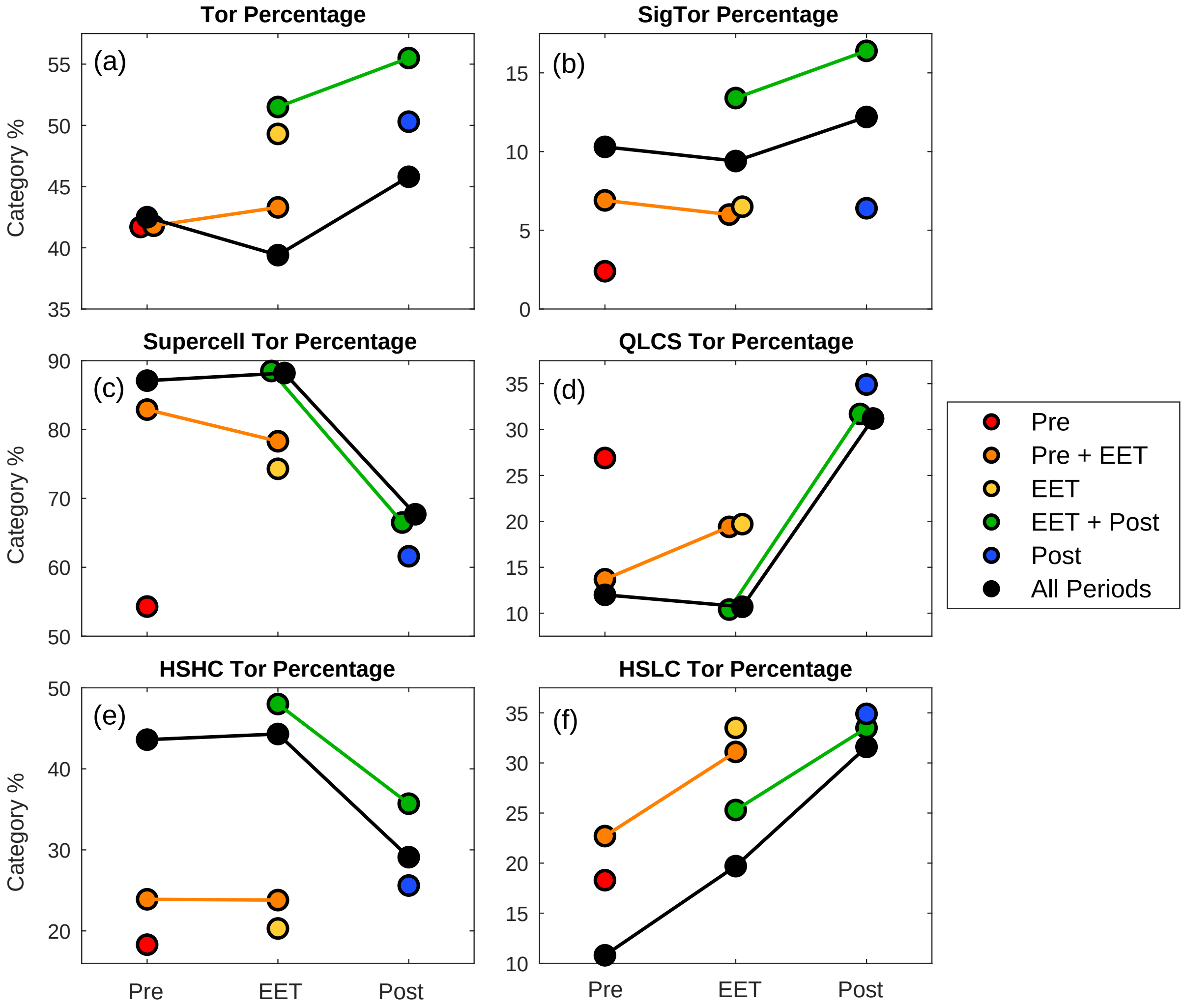

Figure 3.10: Breakdown of (a)-(b) tornado and significant tornado report percentages, as well as the fraction of those tornadoes that were (c) supercellular, (d), QLCS, (e) HSHC, or (f) HSLC in each of the temporal categories in Fig. 3.9; the overall report counts associated with each temporal category (and associated periods) can be found in Table 3.1. Reprinted from Brown et al. (2021), with permission from American Meteorological Society.

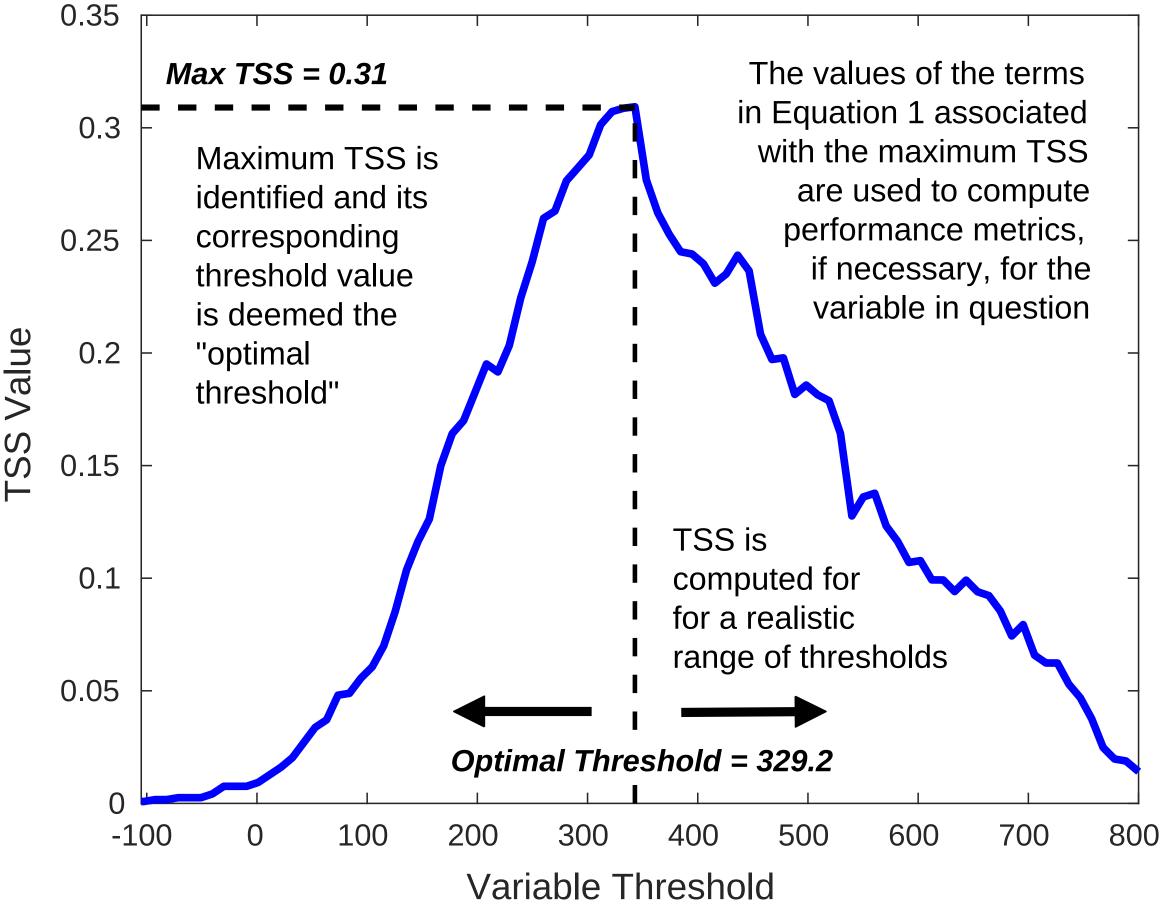

Figure 3.11: Sample TSS curve (corresponding to SRH1 for HSLC sigtors, with threshold values in $m^2\ s^{-2}$), with explanation of the procedure used to determine the optimal variable threshold and associated metrics. Note, the performance metrics discussed are computed using the terms in Equation 3.1 corresponding to the maximum TSS. Reprinted from Brown et al. (2021), with permission from American Meteorological Society.

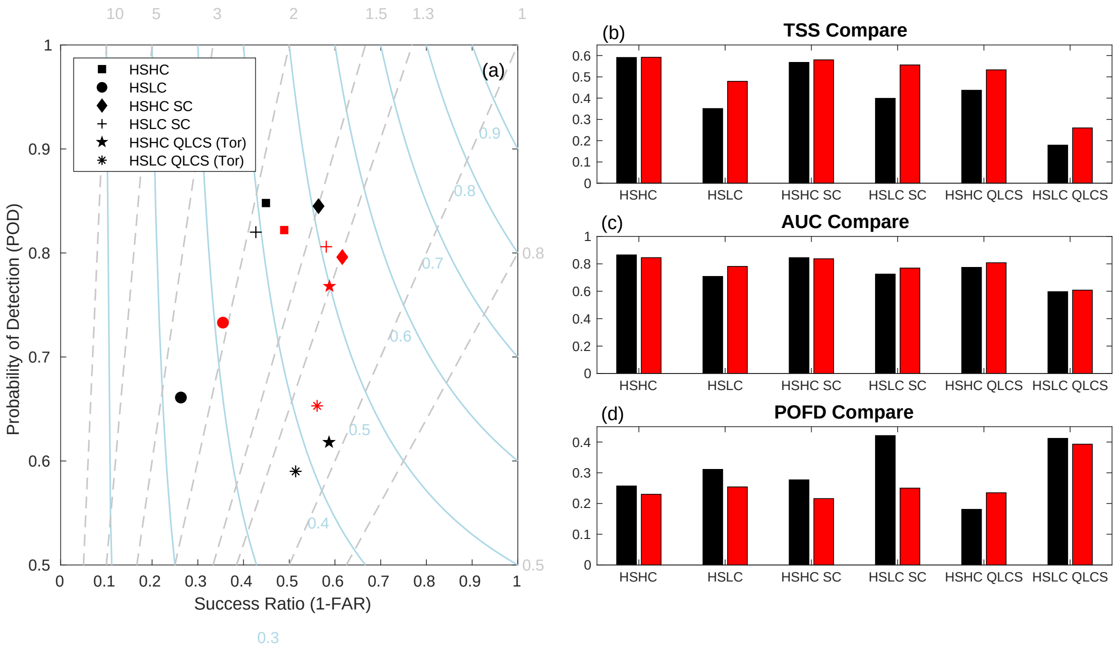

Figure 3.12: (a) Performance diagram for the most skillful pre-existing metrics for each analyzed category from Tables 3.3-3.4 (in black) and the new STP and QLCS Tor metrics (in red). The displayed values of probability of detection (POD) and success ratio are those associated with the maximum TSS values for each metric. Forecast bias is shown in dashed gray lines, and critical success index (CSI) is shown in light blue lines. Note that the y-axis begins at a POD of 0.5 to highlight differences between metrics; also shown are comparisons of (b) true skill statistic (TSS), (c) area under curve (AUC), and (d) probability of false detection (POFD) for the presented metrics. Reprinted from Brown et al. (2021), with permission from American Meteorological Society.

4. IMPACTS OF THE EARLY EVENING TRANSITION ON UPDRAFT FORCING AND EVOLUTION IN IDEALIZED SIMULATIONS OF HIGH-SHEAR, LOW-CAPE SUPERCELLS

4.1 Introduction

Supercell updrafts support some of the strongest vertical velocities realized in the atmosphere (Lehmiller et al. 2001), giving way to a plethora of severe hazards posing risk to life and property. As our understanding of how the environmental characteristics of supercell thunderstorms dictate the maintenance and forcing of their updrafts continues to progress, so should our ability to accurately predict these hazards. Decades of observational and modeling efforts have identified factors which contribute to both low- and mid-level accelerations in supercell updrafts. Some are related to characteristics of the ambient wind profiles - such as deep-layer shear (e.g., Weisman and Klemp 1982; Weisman and Klemp 1984; Rasmussen and Blanchard 1998; Thompson et al. 2003; Warren et al. 2017; Peters et al. 2019), low-level shear magnitude (e.g., Coffer and Parker 2015; Peters et al. 2019) and direction (e.g., Esterheld and Giuliano 2008; Guarriello et al. 2018), storm-relative helicity (SRH; e.g., Davies-Jones 1984; Rasmussen 2003; Markowski et al. 2003; Coffer et al. 2019), and storm-relative (SR) flow (e.g., Warren et al. 2017; Peters et al. 2020b). Other factors are related to thermodynamic characteristics of the near-storm environment - including convective available potential energy (CAPE; e.g., Weisman and Klemp 1982; Rasmussen and Blanchard 1998; Thompson et al. 2003), convective inhibition (CIN; e.g., Mead and Thompson 2011; Gropp and Davenport 2018), and lifting condensation level (LCL; e.g., Rasmussen and Blanchard 1998; Thompson et al. 2003; Craven et al. 2004). When combined into metrics like the significant tornado parameter (STP; Thompson et al. 2003; Thompson et al. 2012), these variables can help us predict whether supercells will persist and if they are capable of producing tornadoes.

However, the parameter space relevant to supercell maintenance and tornadogenesis potential is not uniform across all geographical regions. Though most supercells occur in environments with ample instability (e.g., Thompson et al. 2013), climatological studies have indicated the ability for supercells (and other convective modes) to form and produce severe hazards in environments with limited instability (e.g., Dean and Schneider 2008; Guyer and Dean 2010; Sherburn and Parker 2014). These environments are often accompanied by increases in deep-layer shear, hence their being termed high-shear, low-CAPE (HSLC). Though not confined to one region, these HSLC storms (particularly those producing tornadoes) constitute an important subset of the southeastern US storm climatology (Sherburn and Parker 2014) and pose a unique forecasting challenge (Dean and Schneider 2008; Dean and Schneider 2012; Anderson-Frey et al. 2019). On larger scales, Southeast HSLC storms have been shown to occur in moist, strongly forced synoptic regimes (e.g., Guyer et al. 2006; Sherburn et al. 2016) which, in some circumstances, can interact with nearby features (e.g. Gulf of Mexico) to invigorate regional HSLC conditions (Brown and Nowotarski 2020). On the regional scale, destabilization in association with increased low-level (0-1, 0-3 km) lapse rates and release of potential instability, as well as increased low-level shear/SRH have been shown to play a crucial role in sustaining HSLC convection and its ability to produce severe hazards (Sherburn and Parker 2014; Sherburn et al. 2016; King et al. 2017; Brown et al. 2021). Recent modeling studies such as Sherburn and Parker (2019) have clarified the contribution of these factors to HSLC supercell updraft accelerations, with increased low-level lapse rates providing stronger initial buoyant forcing for supercell updrafts, while shear contributes to low and mid-level rotation via tilting of horizontal vorticity by these updrafts. The latter dictates the nonlinear dynamic pressure accelerations characteristic of supercell updrafts (NDPA; Rotunno and Klemp 1982; Rotunno and Klemp 1985), which the simulations of Wade and Parker (2021) have shown to dominate the forcing of low-CAPE supercell updrafts.

While the severe storms literature discussed thus far has provided valuable insight, the vast majority of these studies rely on singular realizations of the near-storm environment – data retrieved from observations or reanalyses used as time-invariant base states to initialize numerical models, with the characteristics of subsequent convection being attributed to this artificially steady environment. In reality, however, near-storm environments evolve with time, actively influencing the characteristics of their attendant convection (and vice versa, in some circumstances). This is particularly true during the hours surrounding local sunset, a period referred to as the early evening transition (EET) often marked by increasing static stability and CIN, as well as the onset of nocturnal low-level jets (NLLJ; Blackadar 1957; Shapiro et al. 2016). Supercell updrafts have been shown to persist in spite of boundary layer stabilization (Ziegler et al. 2010; Nowotarski et al. 2011; MacIntosh and Parker 2017), owing to the NDPA effects discussed earlier. These effects may be augmented, particularly in the lower portions of updrafts, by increases in low-level shear and SRH associated with the NLLJ as demonstrated in Coffer and Parker (2015). These increases in low-level shear also increase the magnitude of SR flow (e.g., Warren et al. 2017; Peters et al. 2019; Peters et al. 2020b), contributing to wider and less diluted updrafts. It remains to be seen, however, how the sum of these near-sunset factors influence the temporal evolution of storm updrafts. Explicitly examining the response of supercellular updrafts to these numerous environmental changes is crucial to understanding how storms are able to persist across the EET and continue producing severe hazards.

To this end, Gropp and Davenport (2018) utilized radar data and RUC/RAP proximity soundings to examine the evolution of Great Plains supercells as a function of near-storm environmental evolution across the EET. The authors found that the persistence of supercell updrafts past sunset was related to large increases in SRH coupled with minimal increases in most unstable (MU)CIN, consistent with previous studies examining nocturnal supercell tornadoes (e.g., Davies and Fischer 2009; Mead and Thompson 2011). Brown et al. (2021) extended this approach to the Southeast storm climatology, examining how the near-storm environment and subsequent storm characteristics evolve through the EET, and whether this evolution changes as a function of pre-transition CAPE and shear (e.g., high-shear, high-CAPE, or HSHC, vs. HSLC). That study found that HSLC storms lasting through the EET exhibit similar CIN trends as Gropp and Davenport (2018), but post-sunset SRH increases are largely attributed to non-supercellular modes. HSLC supercells, on the other hand, coincide with higher pre-transition SRH values (relative to HSHC supercells) that decrease into the EET, paired with increases in CAPE similar to the rapid destabilization of HSLC storms shown in King et al. (2017). Ample moisture and lower values of downdraft CAPE (DCAPE) are also present in HSLC environments, consistent with the abundantly moist HSLC environments of Sherburn et al. (2016). This moisture may act to inhibit low-level stabilization (as in Mead and Thompson 2011) and limit the development of excessively cold outflow that can be detrimental to updraft maintenance and alignment, and subsequent tornadogenesis (e.g., Markowski et al. 2002; Brown and Nowotarski 2019).

Presumably, these features collectively modulate the low and mid-level updraft accelerations of HSLC supercells in such a way that allows them to persist despite minimal instability. These could include an optimal trade-off of low-level buoyant and dynamic accelerations during the described CAPE/SRH changes, increased updraft width and buoyancy associated with initially higher SRH values (following the SR flow arguments presented earlier), or less negatively buoyant outflow due to ample environmental moisture and reduced evaporative cooling. The exact nature and relative importance of these compensating factors is unclear, however, and serves as the impetus for this study. Using the continuous base state substitution (BSS) technique (Davenport and Parker 2015; Davenport et al. 2019), we will model the response of idealized supercell thunderstorm updrafts to the HSHC and HSLC environmental evolution pathways identified in Brown et al. (2021), establishing a theoretical model of how low-CAPE supercell updrafts respond to and survive the EET. With this goal in mind, our study sets out to address the following questions:

1. As storm environments realistically evolve across the EET for various pre-transition values of CAPE and shear, how do the characteristics of supercell updrafts – including strength, vertical extent, and width – change, and can these characteristics be related to the relative magnitudes of dynamic and buoyant accelerations contributing to these updrafts?

2. Are these changes in updraft accelerations related to other storm attributes that may evolve independent of the prescribed base states, such as storm propagation or SR flow?

The next section details the model configuration and BSS methodology implemented in this study, as well as the soundings that serve as the evolving base states for our simulations. Section 3 reports on the results of these simulations, including evolution of updraft structure and forcing, and other relevant storm features. Finally, section 4 discusses the broader implications of these findings for our understanding of HSLC storm dynamics, and presents relevant directions for future HSLC research.

4.2 Data and methods

4.2.1 Model configuration

This simulations for this study are carried out using CM1 version 20.2 (Cloud Model 1; Bryan and Fritsch 2002). Horizontal grid spacing is 500 m, with a stretched vertical grid spacing of 50-m below 4 km, increasing to 500–m spacing above 15 km. Though this resolution cannot resolve tornado-scale vortices, it is sufficient for resolving the storm updraft features that constitute the focus of this study. The model domain is 175 × 175 km in the horizontal, and spans vertical depth of 20 km. Sub-grid scale turbulence is parameterized with 1.5-order closure (Deardorff 1980). The NSSL double-moment microphysics scheme of (Mansell et al. 2010) was used, with both graupel and hail densities predicted and an initial cloud condensation nuclei (CCN) concentration of 2E9 cm$^-$3, following previous HSLC modeling studies (Sherburn and Parker 2019; Wade and Parker 2021). The Coriolis force, radiation, and surface fluxes of heat, moisture, and momentum are not included in these simulations. A free-slip lower boundary condition is employed. Wade and Parker (2021) discuss the implications of this choice for low-CAPE convection. Convection is initiated using the updraft nudging technique of Naylor and Gilmore (2012), with a horizontal nudging radius of 10 km and a 1 km vertical radius centered at z = 1.5 km AGL. In order to generate convection in our low-CAPE environments, a slightly higher maximum nudging magnitude of 15 m s^{-1} is employed. This nudging is imposed for the first 900 s of model integration, and then gradually diminished until it ceases at 1200 s.

4.2.2 Base state design

The base states used to initialize the simulations presented herein are derived using the pre-transition to EET supercell environmental evolution presented in Brown et al. (2021) (solid lines in their Figs. 6-8)[1]. Specifically, we are focusing on evolution conditioned on the pre-transition environment (HSHC or HSLC). The thermodynamic profiles and hodographs contributing to those patterns were interpolated onto regularly-spaced vertical grids and composited. For hodographs, wind profiles were rotated to align their storm motion vector (as approximated by Bunkers right-mover, or RM; Bunkers et al. 2000) with a common reference angle before compositing and then rotated back by the average storm motion direction across all composited cases. The HSLC Pre CAPE values were not sufficient to sustain quasi-steady updrafts in CM1 – a limitation noted in previous HSLC modeling efforts such as Wade and Parker (2021). Composite soundings across all environments were modified, using a combination of subtle mid-level cooling and low-level warming/moistening, in order to uniformly increase CAPE by ~500 J kg^{-1}, such that the relative differences between HSHC and HSLC patterns remain unchanged. CAPE was increased in such a way that any changes in other thermodynamic quantities, such as 0-3 km CAPE and effective layer quantities, were uniform across environments. This change does compromise the stricter HSLC classification implemented in Brown et al. (2021), but remains within the broader definition of "low CAPE" found in the HSLC literature (i.e., MLCAPE less than 1000 J kg^{-1}; Anderson-Frey et al. 2019). Stratospheric data (i.e., data above 15 km) are approximated following the methodology of Coffer and Parker (2015).

The resultant soundings/hodographs are shown in Figure 4.1. Associated thermodynamic and dynamic parameters are displayed in Tables 4.1-4.2, respectively, for reference. The HSHC composite profiles display the gradual cooling and near-surface stabilization (Fig. 4.1a,c) and early LLJ onset (Fig. 4.1b,d) normally associated with the EET. In contrast, the HSLC composites show a more moist low-level thermodynamic profile with limited near-surface stabilization paired with mid-level cooling (Fig. 4.1a,c), allowing for increases in base-state CAPE values. The HSLC hodographs, though similar in character to the HSHC hodographs, are longer, with greater low-level

---

[1] The decision to only model environmental evolution across two temporal periods, as opposed to a full pre- to post-transition evolution spanning approximately 9-12 hours, was made for both realism and efficiency. Imposing 9-12 hours of environmental evolution in 3-4 hours of model integration for a single storm would be unphysical, and running a simulation for 9+ hours would be computationally expensive. Instead, we opted for a more realistic pre-transition to EET evolution which could realistically occur in the 4 hour window chosen for model integration.

curvature (Fig. 4.1b,d) resulting in higher SRH values, though these values decrease slightly with time.

4.2.3 Base state substitution

The continuous BSS method of Davenport et al. (2019) is implemented to gradually introduce the temporally evolving thermodynamic and wind profiles described above. Each simulation is integrated for a total of four hours, with a constant model integration time step of 1 second. The first 1.5 hours (5400 s) are used for storms to initiate and develop a quasi-steady updraft, as well as allow any remnant numerical effects of the updraft nudging to dissipate. Afterwards, the base state is continually nudged from the original pre-transition base state (BSS1) towards two new base states corresponding to the soundings described above - a linear combination of the Pre and EET soundings (BSS2), and then EET (BSS3). The two new base states are realized at 9000 and 12600 s into model integration, respectively. This process is carried out for both the HSHC and HSLC environmental pathways, along with two additional HSLC simulations varying the thermodynamic and wind profiles separately (i.e., holding the thermodynamic profile constant at pre-transition values and allowing the wind profile to evolve, and vice versa) in order to assess their separate impacts on HSLC storm updraft characteristics. The HSLC simulation with wind evolution only is herein referred to as HSLC-W, and the simulation with thermodynamic evolution only as HSLC-T.

4.2.4 Updraft identification

Updraft identification is performed similar to the methodology of Nowotarski et al. (2020), where the 95th percentile of vertical velocities greater than 0.1 m s^{-1} at each vertical level are used to approximate the extent of the storm updraft core. These statistical updraft thresholds are saved for each model output timestep, and averaged both temporally and across the two primary simulations (HSHC and HSLC) to give a fixed *w*-profile to identify and compare characteristics of simulated updrafts across all four modeled storms. This updraft threshold profile (and its constituent HSHC and HSLC profiles) are included in Figure 4.2 for reference. An additional filter is applied to remove small transient updraft objects, such that only large and spatially coherent updraft volumes are retained. This delineation is based on a subjective minimum threshold for adjacent updraft points. Multiple thresholds were tested, and a minimum of 15 updraft points was sufficient to isolate primary updrafts at 500 m horizontal grid resolution. This corresponds to a updraft with an effective radius of ~1 km. Updraft outlines displayed in later figures correspond to this filtered updraft identification.

4.3 Results

4.3.1 Overview of simulations

All four simulations produce discrete storms that persist and maintain supercell-like characteristics throughout all four hours of model integration. Figures 4.3-4.4 display the evolution of the modeled reflectivity and cold pool/near-surface buoyancy fields, respectively. HSHC storms largely match the supercell archetype established by Lemon and Doswell III (1979), displaying a horseshoe-shaped low-level updraft straddling a well-defined hook echo and forward-flank reflectivity gradient (Fig. 4.3a-c). The reflectivity field and updraft cycle and contract midway through the simulation, but expand once again at later time steps. The attendant HSHC cold pools (Fig. 4.4a-c) are initially expansive and negatively buoyant, but weaken and shrink in time coinciding with reflectivity/updraft changes described earlier. In contrast, the HSLC simulation shows an initially more compact reflectivity structure which gradually grows upscale with time (Fig. 4.3d-f). Though this north-south elongated reflectivity structure appears increasingly quasi-linear, the storm maintains a single robust updraft at the southern end of the structure consistent with supercellular characteristics, with this updraft growing wider with time. Additionally, the HSLC simulation contains a weaker and smaller cold pool in comparison to the HSHC storm (Fig 4.4d-f). The HSLC-W and HSLC-T simulations are largely similar to the HSLC simulation in terms of their reflectivity field evolution (Fig. 4.3g-i, j-l, respectively), but HSLC-T exhibits a markedly weaker cold pool (Fig. 4.4 j-l), more positively buoyant inflow, and a wider low-level updraft than HSLC-W.

4.3.2 Updraft structure

Next we examine how the vertical structure and accelerations of the modeled storm updrafts evolve with their associated base states, beginning with time-height profiles of maximum *w* within these updrafts (Fig. 4.5). Also included is the height at which the updraft acceleration profile ($\frac{dw}{dz}$) minimizes to give a rough approximation of the upper extent of the modeled updraft cores. The HSHC simulation updrafts (Fig. 4.5a) develop deep, robust updrafts (*w* well above 50 m s^{-1}) maximizing in the upper troposphere (≥10 km AGL), but with velocities exceeding 40 m s^{-1} extending as low as 2-3 km AGL. As time progresses, this updraft weakens (particularly below 4 km) with some intermittent restrengthening aloft before ultimately diminishing by the end of model integration. All of the HSLC updrafts (Fig. 4.5b-d) are substantially more shallow than the HSHC updraft, with their associated velocity maxima mostly confined to heights of 2-4 km AGL. This is not surprising given the differences in HSHC and HSLC updraft profiles in Figure 4.2, and corroborates previous modeling and observational studies examining the vertical structure of low-CAPE supercells (e.g., Davies 2006; Murphy and Knupp 2013; Wade and Parker 2021). Both the HSLC and HSLC-T simulations (Fig. 4.5b,d, respectively) exhibit a weak, transient low-level updraft between BSS1 and BSS2 that rapidly deepens and intensifies up through and past BSS3, though the HSLC-T updraft reaches higher maximum values and remains largely below 6 km AGL. HSLC-W (Fig. 4.5c) never develops a strong updraft comparable to the other HSLC simulations, with the upper extent of its updraft remaining below 3-4 km for the entirety of the simulation.

We also wish to characterize the width of the storm updrafts. Figure 4.6 displays time-height plots of effective updraft radius (R_{eff}), as approximated by the number of updraft grid points identified with the criteria discussed earlier[2]. Also included on these plots is base-state SR flow magnitude relative to modeled storm motion (i.e., base-state wind profiles with modeled storm motion subtracted off). Studies like Peters et al. (2019) demonstrated that increased SR flow in a given environment contributes to larger inflow, which in turn leads to wider and more buoyant

---

[2] This method is susceptible to over-counting of updraft grid points when more than one updraft feature is identified. However, the benefit of our updraft filtering method is that it generally identifies a single dominant updraft core. In the limited instances where more than one updraft area is identified, these updrafts tend to coalesce soon afterwards.

updrafts that are increasingly resistant to entrainment-driven dilution. Furthermore, SR flow with the effective inflow layer (EIL; Thompson et al. 2007) correlates with updraft width and maximum vertical velocity throughout the depth of the storm (Peters et al. 2020b). For reference, Figure 4.7 shows 0-2, 2-4, and 4-6 km AGL layer averages of the SR flow field shown in Fig. 4.6.

The HSHC modeled updraft width (Fig. 4.6a) is the most steady of the simulations, with consistently narrower updrafts (R_{eff} < 2 km) near the surface and increasingly wider updrafts at higher elevations. There is some updraft contraction below 4 km and expansion above 4 km in the last hour of model integration, but these changes are subtle compared to the changes in other simulations. Similarly, HSHC SR flow patterns (Fig. 4.7a) show largely indistinct patterns in each analyzed layer, except for a late decrease in 0-2 km SR flow and increase in 4-6 km SR flow perhaps responsible for the slight changes in updraft width described previously. The HSLC simulations show much more temporal heterogeneity in both their updraft width and SR flow evolution. All three HSLC simulations display moderate updraft widths (R_{eff} ~3-4 km) in the lowest 6 km during 1-2.5 hours (i.e., prior to BSS2) with some transient increases aloft (Fig. 4.6b-d). This coincides with gradual increases in 0-2 km SR flow, and gradual decreases in SR flow above 2 km (Fig. 4.7b-d). After BSS2, however, these simulations diverge, with HSLC and HSLC-T displaying sustained increases in 0-2 km SR flow paired with an uptick in 2-4 and 4-6 km SR flow after BSS3 (Fig. 4.7b,d). These SR flow trends correspond with rapidly increasing updraft width (particularly above 2 km) in the final hour of model integration (Fig. 4.6b,d). In contrast, HSLC-W shows slower increases in 0-2 km SR flow and continued decreases in 2-4 and 4-6 km SR flow (Fig. 4.7c). Though its associated updrafts show some slight widening after BSS3 (Fig. 4.6c), this widened updraft never reaches the size or vertical extent of those seen at the end of the HSLC and HSLC-T simulations. In fact, the width and vertical extent of the HSLC-related simulations appear to scale by the magnitude of their 0-2 km SR flow, consistent with the physical arguments of Peters et al. (2019). It is worth noting that these changes in SR flow are not a direct consequence of changes in the base-state winds. As these HSLC updrafts strengthen and grow, there are also likely changes in storm motion that modulate SR flow at different levels. This possibility will be addressed in later sections.

4.3.3 Updraft forcing

In addition to intensity, vertical extent and width, we also wish to characterize the accelerations contributing to the modeled storm updrafts. Previous studies examining low-CAPE storms, such as McCaul Jr and Weisman (1996) and Murphy and Knupp (2013), have noted that buoyant contributions to updraft speed in these storms are reduced relative to high-CAPE storms. Instead, low-level dynamic accelerations have been shown to play a sizeable role in determining the strength of low-CAPE supercellular updrafts (e.g., Wade and Parker 2021). However, it is unclear how temporal changes in the near-storm environment may affect these dynamic and buoyant accelerations and their relative contributions to updraft intensity. As such, we consider how buoyant and dynamic accelerations evolve with the imposed model base states and influence updraft characteristics.

In order to assess these updraft accelerations, we begin with the vertical momentum equation, which once we make the Boussinesq approximation and neglect frictional effects reduces to the following:

$$\frac{Dw}{Dt} = -\alpha_0 \frac{\partial p'}{\partial z} + B, \tag{4.1}$$

where w is vertical velocity, α_0 is a specific volume constant, p' is a perturbation pressure, and B is buoyancy. The first term on the right hand side of Eqn. 4.1 is the vertical perturbation pressure gradient acceleration (VPPGA) and the second term reprsents acceleration due to buoyancy. Following a similar approach as Rotunno and Klemp (1982) and Rotunno and Klemp (1985), the perturbation pressure field can be decomposed into its constituent parts – buoyancy (p'_B), linear dynamic (p'_{D_L}), and nonlinear dynamic ($p'_{D_{NL}}$) pressure perturbations. Substituting these perturbation pressures into Eqn. 4.1 gives:

$$\frac{Dw}{Dt} = \underbrace{B - \alpha_0 \frac{\partial p'_B}{\partial z}}_{B_{Eff}} \underbrace{- \alpha_0 \frac{\partial p'_{D_L}}{\partial z} - \alpha_0 \frac{\partial p'_{D_{NL}}}{\partial z}}_{ACCD}. \tag{4.2}$$

Buoyancy and the buoyant VPPGA can be grouped into a single acceleration know as effective buoyancy (B_{Eff}). Additionally, the linear and nonlinear dynamic VPPGA are grouped into a net dynamic acceleration (ACCD). In the case of supercells, the nonlinear dynamic VPPGA often exceeds the linear VPPGA within its updraft core, though linear forcing can be large on the flanks of this updraft and have a substantial influence on its propagation (e.g., Rotunno and Klemp 1982; Davies-Jones 2002). Pressure decomposition is computed inline with CM1, and the associated accelerations are output at every model time step.

Figure 4.8 shows the profiles of B_{Eff}, ACCD, and total forcing (the sum of B_{Eff} and ACCD) averaged within the storm updraft during the period ± 30 minutes from each BSS time (BSS1, BSS2, and BSS3). Vertical profiles of w_{max} averaged over the same time periods are included in Figure 4.9, for reference. For the HSHC simulations (Fig. 4.8a-c), the ACCD profiles maximize near the surface and diminish with height. B_{Eff} remains entirely positive and maximizes around 4-5 km AGL. These features lead to a total updraft acceleration profile dominated by ACCD below 1 km, but increasingly influenced by B_{Eff} above 1 km. These low-level ACCD and mid-level B_{Eff} maxima decrease with time, leading to a gradually weakening (though still robust) w_{max} profile (Fig. 4.9a-c).

The HSLC simulations (Fig. 4.8d-l) show similar initial near-surface maxima in ACCD, but these ACCD values increase more rapidly with time in HSLC (Fig. 4.8d-f) and HSLC-T (Fig. 4.8j-l), similar to the SR flow evolution in Fig. 4.7b,d. Interestingly, despite increasing CAPE values in their associated base states, both HSLC and HSLC-W (and also HSLC-T) display very small B_{Eff} values throughout the depth of their updrafts, though their mid-level B_{Eff} values become slightly positive by BSS3 whereas HSLC-W mid-level B_{Eff} (Fig. 4.8g-i) becomes slightly negative. Regardless, the lack of a prominent B_{Eff} maximum aloft like that in the HSHC simulation allows total mid-level updraft accelerations in the HSLC simulations to become negative, with the height of these minima increasing with time. Given that this height increases more dramatically in HSLC and HSLC-T, it is likely that it at least partially dictates the vertical extent of these HSLC storm updrafts (as in Fig. 4.5b-d). This assertion is also supported by the deepening HSLC and HSLC-T

w_{max} profiles in Fig. 4.9d-f, g-i, respectively. Perhaps most importantly, the uniformly small HSLC B_{Eff} values mean that ACCD dominates updraft accelerations in these simulations, consistent with previous low-CAPE modeling studies (McCaul Jr and Weisman 1996; Sherburn and Parker 2019; Wade and Parker 2021).

4.3.4 Updraft propagation

The HSLC updraft characteristics presented thus far tell a coherent physical story. Gradually increasing low-level SR flow widens and strengthens updraft cores, consistent with the physical arguments of Peters et al. (2019). Given the near-sunset timing of these storms, their updraft characteristics and the increasing contribution of ACCD to its low-level accelerations, one might assume that the HSLC environmental evolution coincide with the onset of a NLLJ. Such a feature would introduce additional SRH and stronger low-level dynamic updraft forcing, as in Coffer and Parker 2015). Recall, however, that the HSLC base-state hodograph evolution shows a *decrease* in shear/SRH at all heights through the EET, so the aforementioned updraft characteristics appear to be at odds with their underlying environmental evolution.

Calculations of SR-flow and SRH often depend on assumptions about storm motion in relation to the environmental wind profile. Given the contradictions described above, our modeled storm motion may deviate from estimates of storm motion like Bunkers RM. In order to assess this, Figure 4.10 shows the evolution of Bunkers RM, modeled storm motion[3], and the 0-6 km mean wind vectors in each simulation. The HSHC simulation (Fig. 4.10a) maintains storm motion with a slightly smaller u-component but generally close to Bunkers RM, as may be expected. Early in the BSS implementation, the HSLC simulations (Fig. 4.10b-d) exhibit storm motions to the left of Bunkers RM, closer to 0-6 km mean wind. As time progresses, these HSLC storm motion vectors move towards Bunkers RM, but HSLC and HSLC-T (Fig. 4.10b,d, respectively) show further deviation during the final hour of model integration right of Bunkers RM.

The question that follows is: how do these variations in modeled storm motion influence the

---

[3] Storm motion is approximated following the movement of the 2-5 km UH maximum, with some subjective adjustment in the rare instances where the UH maximum moves sporadically (e.g., when updrafts are weak and transient).

SRH experienced by these updrafts? As noted in Coniglio and Parker (2020) (their Fig. 11), off-hodograph propagation can to alter the SR flow (and SRH, by extension) in a given near-storm environment, though the sign and magnitude of this change may differ depending on the depth of SR flow/SRH being considered. Furthermore, the subtle lengthening of the modeled HSLC and HSLC-T storm motion vectors with time (Fig. 4.10b,d, respectively) likely contributes to increased SR flow as well. To answer this question, SRH is recomputed using our modeled storm motion evolution in place of Bunkers RM as used in the original calculations, both of which are shown in Figure 4.11. For the HSHC simulation (Fig. 4.11a), there are differences between SRH calculations depending on the storm motion vector used, with systematic under-representations as large as 100 m^2 s^{-2} when using Bunkers RM. That being said, the difference between Bunkers and model-derived SRH become lesser in layers extending above 1 km. Despite these differences in magnitude, the trend of HSHC SRH is consistent regardless of the storm motion vector used for calculation – meaning the differences between Bunkers and modeled SRH are relatively steady with time. For the HSLC-related simulations (Fig. 4.11b-d), SRH computed in layers of 0-1 km and deeper are slightly below Bunker RM SRH early in simulations, but increase steadily with time and exceed Bunkers RM SRH past the 3-h mark (contrary to their decreasing Bunkers-based SRH values). Similar to Figure 4.7, the HSLC and HSLC-T simulations (Fig. 4.11b-d) exhibit the largest departures from Bunkers RM SRH by the end of the simulations, consistent with their exceedingly deviant storm motion in Figure 4.10.

Though the storm motion and associated SRH patterns presented in Figures 4.10-4.11 likely explain the HSLC updraft characteristics presented thus far, there are two other factors worth considering that may add valuable context to these results. The first of these is the role of linear forcing in the propagation of the modeled HSLC storms. This forcing is the primary cause of lateral updraft propagation in the presence of curved hodographs (e.g., Rotunno and Klemp (1982); Klemp 1987), and the magnitude of this propagation component increases with larger initial shear/SRH values and stronger updrafts (Weisman and Rotunno 2000; Davies-Jones 2002). Given that all of the HSLC simulations exhibit storm motion that deviates rightward with time, it is possible that the overall higher shear/SRH values associated with these environments support a stronger linear forcing component relative to the HSHC simulation.

To this end, Figure 4.12 displays the 0-3 km and 0-6 km averaged maximum linear dynamic pressure accelerations (LDPA) during the period ± 30 minutes from each BSS time[4]. Both the 0-3 and 0-6 km HSHC maximum LDPA decreases with time, whereas the HSLC simulations show LDPA maxima that either remain generally constant or increase with time. These increases are most pronounced in the HSLC and HSLC-T simulations, and their larger LDPA maxima are realized at lower levels even with appreciable vertical velocities extending above 3 km (as in Fig. 4.5b,d). Physically, LDPA can be characterized as follows:

$$LDPA \propto \frac{\partial}{\partial z}(\vec{S} \cdot \nabla_h w), \tag{4.3}$$

where $\vec{S}$ is the vertical wind shear vector and second term represents the horizontal gradient of vertical velocity. Given the shear magnitude is decreasing at all heights in the HSLC base state (Table 4.2) and shear orientation only changes slightly (not shown), this suggests the primary driver of these later increases in LDPA are changes in updraft intensity in the final hour of model integration – though again, the initially large shear/SRH may drive lateral updraft propagation earlier in HSLC simulations.

The second consideration worth examining is whether the widening and strengthening of HSLC and HSLC-W updrafts with time is simply related to their increasing CAPE values. McCaul Jr and Weisman (2001) noted the vertical distribution of buoyancy modulates storm updraft intensity more strongly in low-CAPE environments, suggesting that destabilization of these HSLC environments (particularly at low levels) may strongly influence their associated updraft characteristics. In order to address this matter, we need to relate our maximum modeled updraft speeds to our base-state CAPE evolution. One common expression used to relate these factors is as follows:

$$w_{max} = \sqrt{2 \times CAPE}. \tag{4.4}$$

---

[4] This is computed in a 25 × 25 km box centered on the 2-5 km UH maximum used to track each simulated storm.

However, this is often viewed as the "thermodynamic limit" of updraft speed which most storms fail to realize due to the effects of mixing and entrainment on the peripheries of storm updrafts. As such, Peters et al. (2020a) set out to a derive a more accurate formula to predict maximum supercell updraft velocities by using entrainment CAPE (ECAPE) to factor in the updraft-diluting properties that the previous expression failed to capture. Figure 4.13 shows analytic curves for predicted w_{max} as a function of base state derived MUCAPE and ECAPE relative to modeled w_{max} values. Modeled updraft speeds lying closer to the ECAPE-derived w_{max} curve indicate updrafts experiencing more entrainment and dilution compared to those nearer to the MUCAPE curve. Furthermore, changes in modeled updraft speed as a function of CAPE parallel to these analytic expressions suggest modulation of updraft *primarily* driven by CAPE increases, whereas more abrupt changes in this w-CAPE parameter space may be related to external factors (e.g., changes in dynamic forcing).

All of the HSLC simulations show a $\sim$ 5 m s^{-1} increase in updraft speed to a value of 25 m s^{-1} in the 30 minutes prior to the beginning of BSS implementation, related to initially high shear and SRH values and subtle lengthening of storm motion vectors (white and light pink dots in Fig. 4.10b-d). HSLC-T updraft speeds (Fig. 4.13b) remain at this 25 m s^{-1} mark for the majority of the simulation, before increasing once again to $\sim$ 30 m s^{-1} between 3-3.5-h. In contrast, HSLC and HLSC-T updraft speeds (Fig. 4.13a,c, respectively) immediately begin to increase away from the ECAPE curve, presumably owing to increased SR flow and updraft width shown in Figs. 4.6-4.7b,d. These increases remain relatively parallel to the ECAPE and MUCAPE curves until substantial jumps during the final hour of model integration. The $\sim$ 20 m s^{-1} gap in between the final HSLC/HSLC-T and HSLC-W updraft speeds can be attributed to the rapid destabilization in the former. More specifically, 15 m s^{-1} or 75% of this difference is likely caused by off-hodograph propagation, given that changes in ECAPE/MUCAPE between hours 3-4 *at most* account for 5 m s^{-1} of w increases (following the analytic w-CAPE curves).

4.3.5 Summary and conclusions

Though our understanding of low-CAPE supercell updraft forcing and maintenance has grown considerably in recent years, the response of these updrafts to the near-storm environmental changes associated with the EET have been left largely unaddressed. Using base state substitution to impose the EET environmental pathways established in Brown et al. (2021), this study set out to determine how supercellular updrafts evolve into the evening given varying pre-sunset CAPE and shear values. In doing so, we reached the following conclusions:

- HSHC storms develop initially deep, robust updrafts which gradually weaken through the imposed EET evolution, likely due to its decreasing CAPE and increasing CIN magnitude. In contrast, HSLC storms develop initially more shallow updrafts (confined below ~4-5 km AGL), which gradually increase in depth, width, and strength with time in tandem with increasing CAPE, despite decreases in background shear/SRH.
- HSLC storms exhibit sustained lateral updraft propagation through the EET, with storm motion vector turning towards and/or right of Bunkers RM by the end of model integration. This deviant motion – which is largest for simulations with a destabilizing background environment – leads to enhanced SR flow and SRH, particularly in the lowest 2 km, which exceeds what is predicted by the base-state hodograph evolution alone.
- In addition to updraft width, these prolonged increases in SR flow and SRH contribute to HSLC updrafts whose forcing is dominated by dynamic pressure accelerations throughout its vertical extent, consistent with previous characterizations of low-CAPE updrafts. This differs from HSHC updrafts, which are more dynamically forced at low levels, yet buoyantly forced aloft.
- The primary impact of rapid destabilization on HSLC updraft enhancement is related to off-hodograph propagation and its subsequent SR flow influences, rather than the direct impact of increasing CAPE.

These results highlight several important and interconnected characteristics of HSLC supercell updrafts during the EET, the first of which is off-hodograph propagation. As described earlier, initial off-hodograph propagation is likely related to high pre-transition shear/SRH base-state values, while later deviations are related to updraft strengthening. This deviant motion suggests that sounding-derived attributes related to storm motion may be insufficient to fully characterize the propagation and storm-relative properties of low-CAPE storms, particularly those occurring in a rapidly evolving background environment. To this point, the second vital characteristic is the role that rapid destabilization plays in the development of strong vertical velocities in these HSLC storms, as suggested previously by King et al. (2017). In addition to the direct updraft enhancement related to increasing CAPE, its impact on updraft strength sets off a causal chain by which stronger updrafts obtain a larger lateral propagation component (via increased linear dynamic forcing), thus increasing SR flow and SRH as described above and further strengthening the low to mid-level updraft. Furthermore, this destabilization increases the vertical extent of HSLC updrafts, which (though not explicitly shown) puts the updrafts in contact with stronger steering flow aloft, potentially exacerbating its off-hodograph propagation. Altogether, rapid stabilization and its dynamic consequences may be a necessary feature for HSLC supercell updrafts to strengthen through the EET.

There are still numerous aspects of HSLC supercells and their response to changes in near-storm environments worth exploring. One such aspect is the effect of friction on HSLC storm dynamics. While studies such as Schenkman et al. (2014) have demonstrated the contribution of frictional generation to vortexgenesis in traditional high-CAPE environments, Wade and Parker (2021) noted that inclusion of friction tends to inhibit the formation of tornado-like vortices in low-CAPE storms. Though tornadogenesis extends beyond the scope of this study, understanding the role of friction for the maintenance of severe convection remains critical, particularly in the Southeast given more complex terrain and land cover relative to the Great Plains. Another important caveat for this study is the use of composite soundings and hodographs for our BSS implementation. Though, on average, HSLC supercells persisting through the EET exhibit the imposed environmental evolution, some storms may in fact experience decreases in CAPE and/or increases in shear or SRH (relative to Bunkers RM). It is also worth noting here that there are potential sources of error (meaning a misrepresentation of the convective environment) in the sounding-derived dataset used to determine this EET evolution, as described in Brown et al. (2021). Regardless, examining the updraft response to these other environmental pathways would foster a more robust characterization of nocturnal HSLC updrafts.

Also relevant is the importance of storm mode for HSLC storm maintenance. Quasi-linear convective systems constitute a large portion of the HSLC climatology (e.g., Smith et al. 2012; Davis and Parker 2014), and HSLC supercells persisting through the EET and producing severe convective hazards post-sunset typically grow upscale rather than remaining isolated (e.g., Brown et al. 2021). As such, similar simulations could be run using the storm initiation approach of Sherburn and Parker (2019) to develop HSLC supercells embedded within broader linear features. We could then compare the embedded supercell updraft evolution with that of the isolated HSLC supercells in this study, further advancing our understanding of the nocturnal persistence of low-CAPE storms.

Lastly, efforts must continue to sample the environments of low-CAPE storms at high spatiotemporal resolution. This can be accomplished in a variety of ways, whether that be the deployment of an array of probes to collect in-situ atmospheric measurements (as in McDonald and Weiss 2021), or perhaps the unmanned aerial vehicles (UAVs) to rapidly sample the vertical structure of developing storm environments (as in Frew et al. 2020). Of particular importance is the how the magnitude and vertical distribution of buoyancy changes in these environments and ultimately impacts the mode and longevity of their associated storms. Given the importance of rapid destabilization for HSLC updrafts, as demonstrated in this and previous studies, these fine-scale observations of how low-CAPE storm environments evolve will have innumerable benefits for both our physical model of low-CAPE storms and our ability to forecast their persistence and production of severe convective hazards past sunset.

Table 4.1: Sounding-derived CAPE and CIN evolution (in J kg^{-1}) for HSHC and HSLC values corresponding to the HSHC and HSLC thermodynamic and wind profiles in Figure 4.1.

	HSHC		**HSLC**	
	Pre	*EET*	*Pre*	*EET*
SBCAPE	2501	1750	755	1251
MLCAPE	2530	2057	814	1163
MUCAPE	2583	2123	1044	1490
SBCIN	-22	-53	-26	-16
MLCIN	-9	-15	-3	-2
MUCIN	-5	-15	-3	-3

Table 4.2: Sounding-derived shear (SHR; in m s^{-1}) and SRH (in m^2 s^{-2}) values corresponding to the HSHC and HSLC thermodynamic and wind profiles in Figure 4.1.

	HSHC		**HSLC**	
	Pre	*EET*	*Pre*	*EET*
SHR1	11.8	14.4	19.0	15.4
SHR3	20.1	22.6	24.7	23.7
SHR6	27.3	29.8	32.9	29.3
Eff SHR	18.0	20.1	23.7	22.1
SRH500	108	154	215	136
SRH1	198	255	357	282
SRH3	313	351	438	419
Eff SRH	292	331	425	397

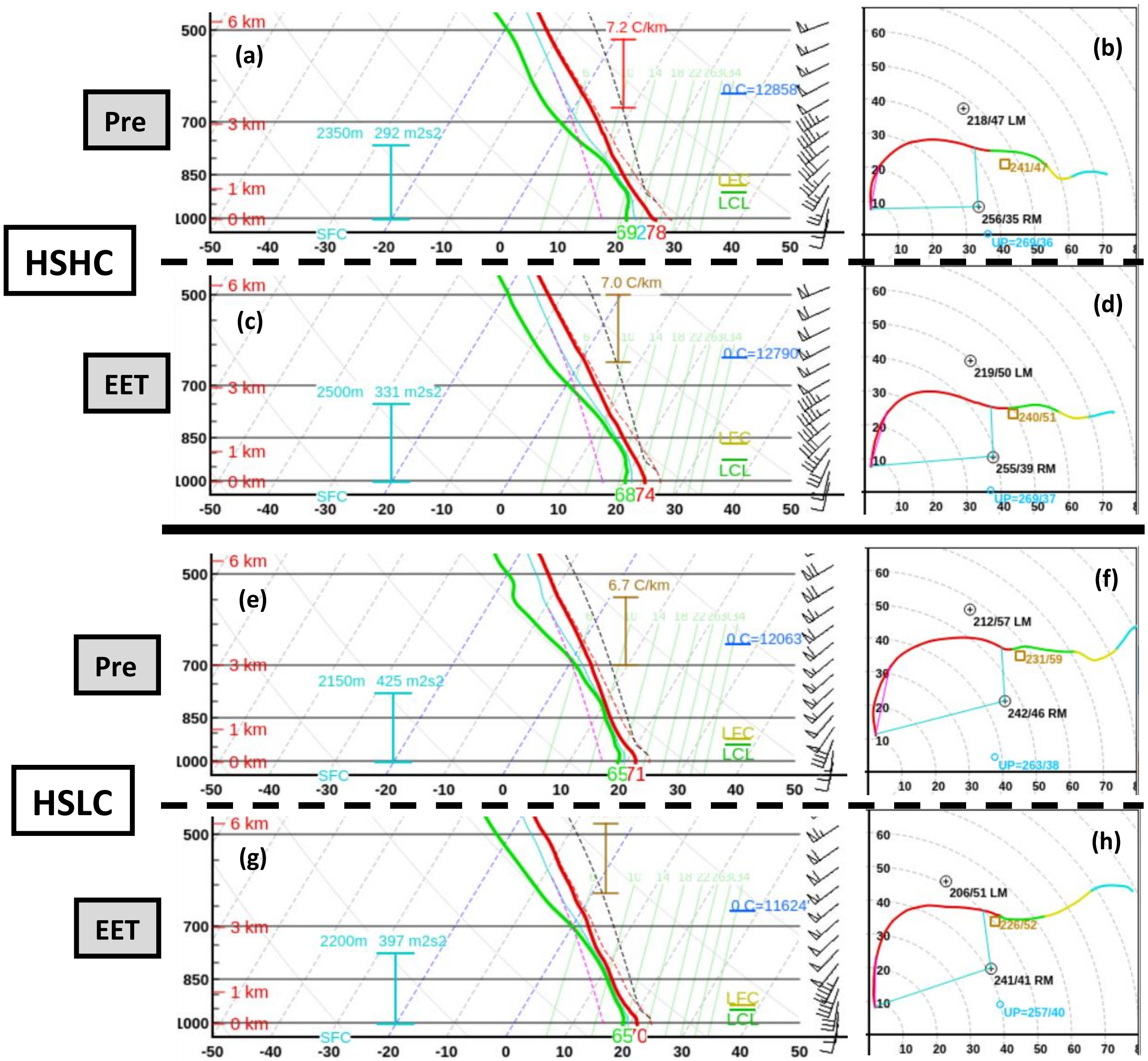

Figure 4.1: Composite low-level thermodynamic profiles and hodographs for the (a)-(d) HSHC and (e)-(h) HSLC evolution pathways as identified in Brown et al. (2021). The left panel in each row shows the thermodynamic profile below 6 km for each base state, with the red line representing environmental temperature and the green line representing environmental dewpoint temperature, and the blue bracket representing the depth of the effective inflow layer (EIL; Thompson et al. 2007). The right panel in each row represents the environmental hodograph, with the red, green, yellow and light blue segments representing the 0-3, 3-6, 6-9, and 9-12 km AGL layers, respectively. The blue lines bracketing the lower portion of the hodograph represent the EIL bounds shown in the thermodynamic plot, relative to the Bunker RM storm motion estimate (denoted with a black circle).

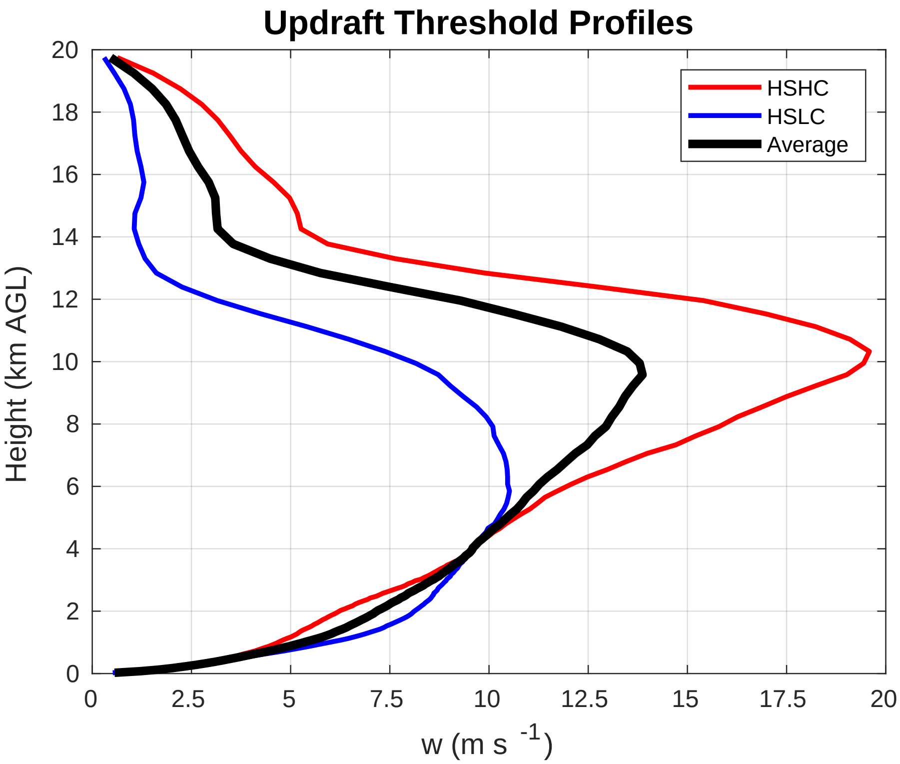

Figure 4.2: Time-averaged updraft threshold profiles for the HSHC (in red) and HSLC (in blue) simulations, and the average of the two (in black) used for updraft identification.

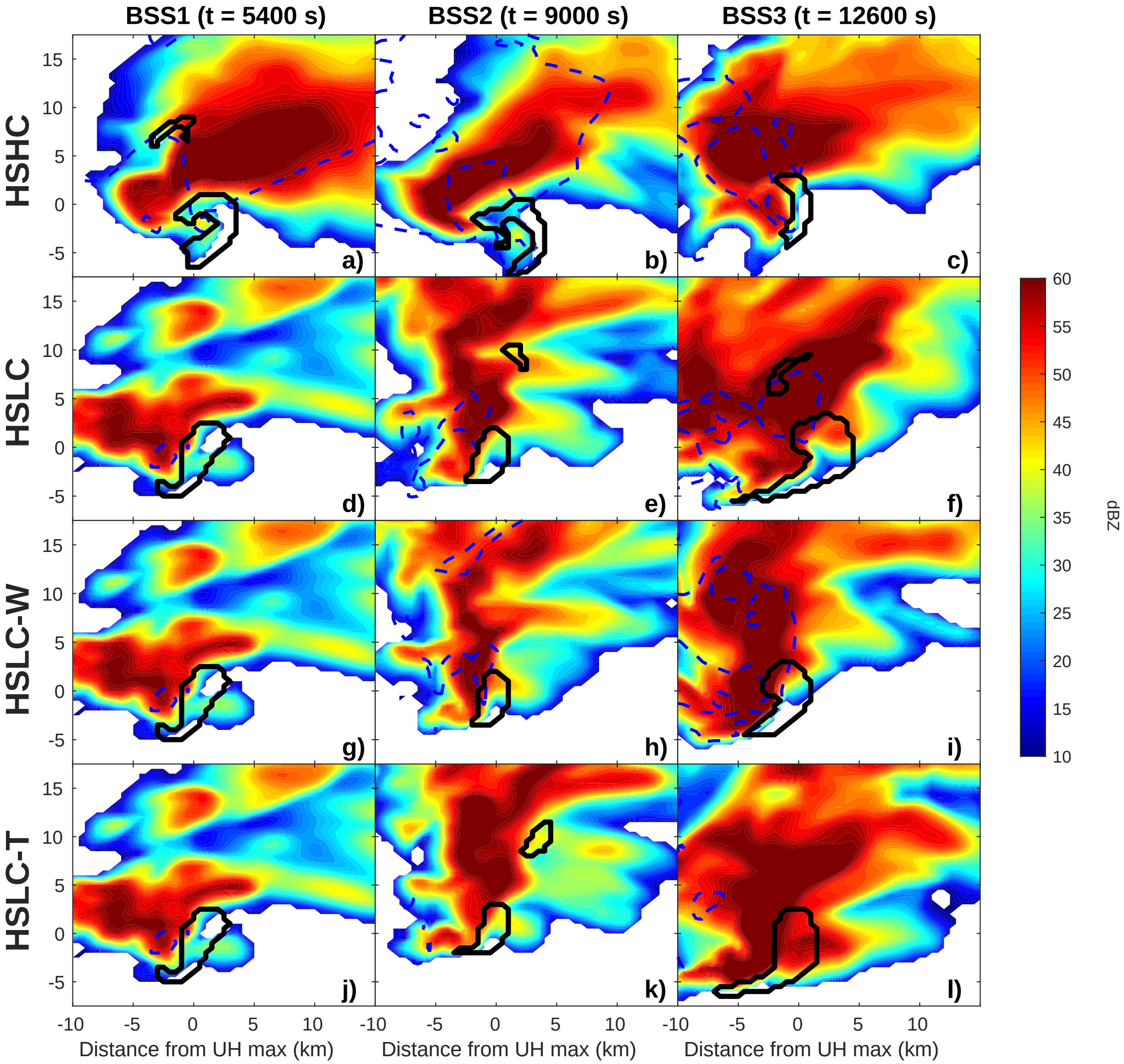

Figure 4.3: Plan views of near-surface reflectivity (shaded), storm updraft at 1 km AGL (black contour), and the -1 K near-surface potential temperature perturbation (blue dotted contour; used to approximate the cold pool leading edge) at BSS1, BSS2, and BSS3, corresponding to the (a)-(c) HSHC, (d)-(e) HSLC, (g)-(i) HSLC-W and (k)-(l) HSLC-T simulations. The x and y units are kilometers from the 2-5 km updraft helicity maximum (used to track the storms).

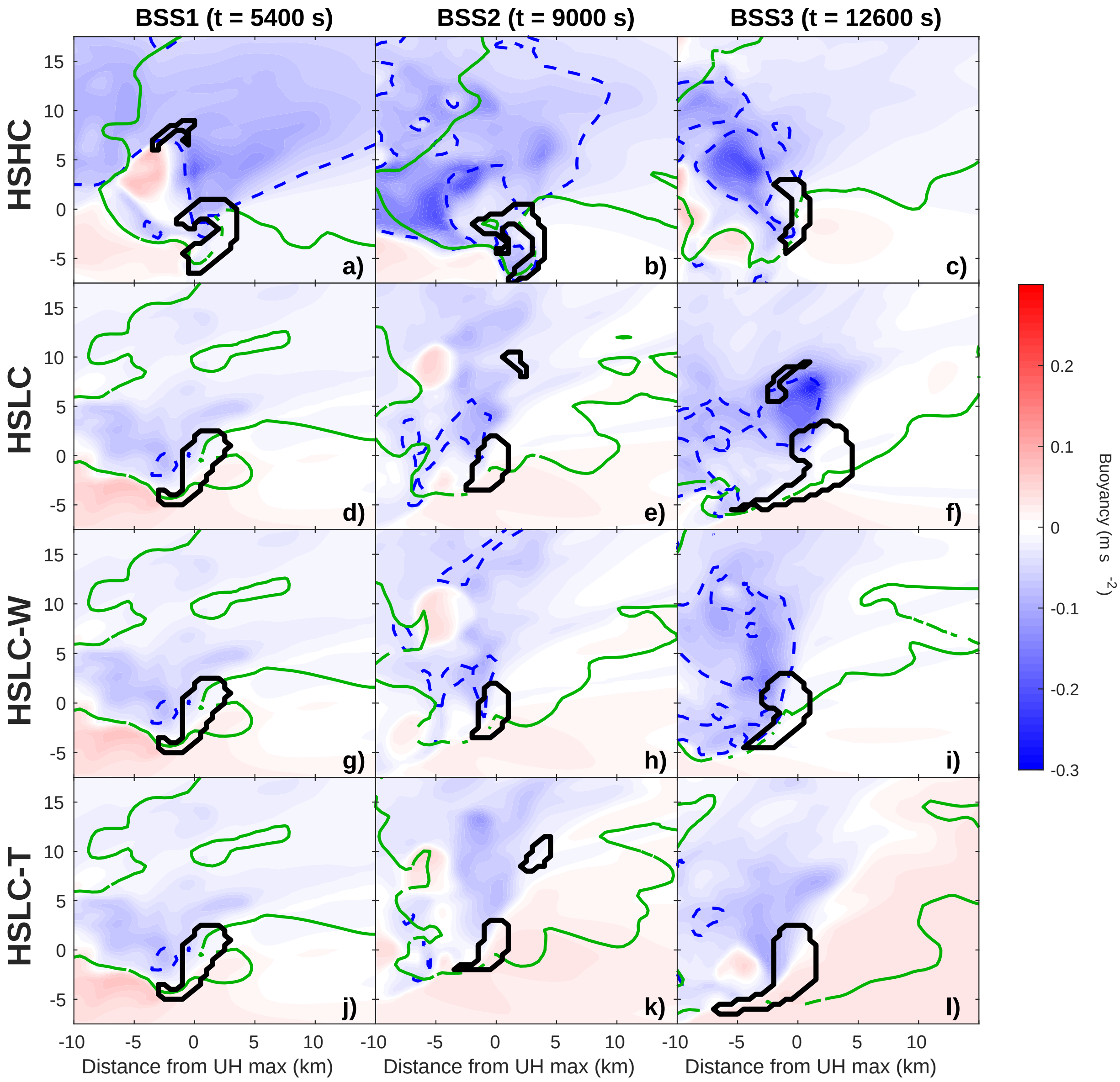

Figure 4.4: Plan views of near-surface buoyancy (shaded), storm updraft at 1 km AGL (black contour), the 20 dBZ near-surface reflectivity contour (green contour), and the -1 K near-surface potential temperature perturbation (blue dotted contour; used to approximate the cold pool leading edge) at BSS1, BSS2, and BSS3, corresponding to the (a)-(c) HSHC, (d)-(e) HSLC, (g)-(i) HSLC-W and (k)-(l) HSLC-T simulations. The x and y units are kilometers from the 2-5 km updraft helicity maximum (used to track the storms).

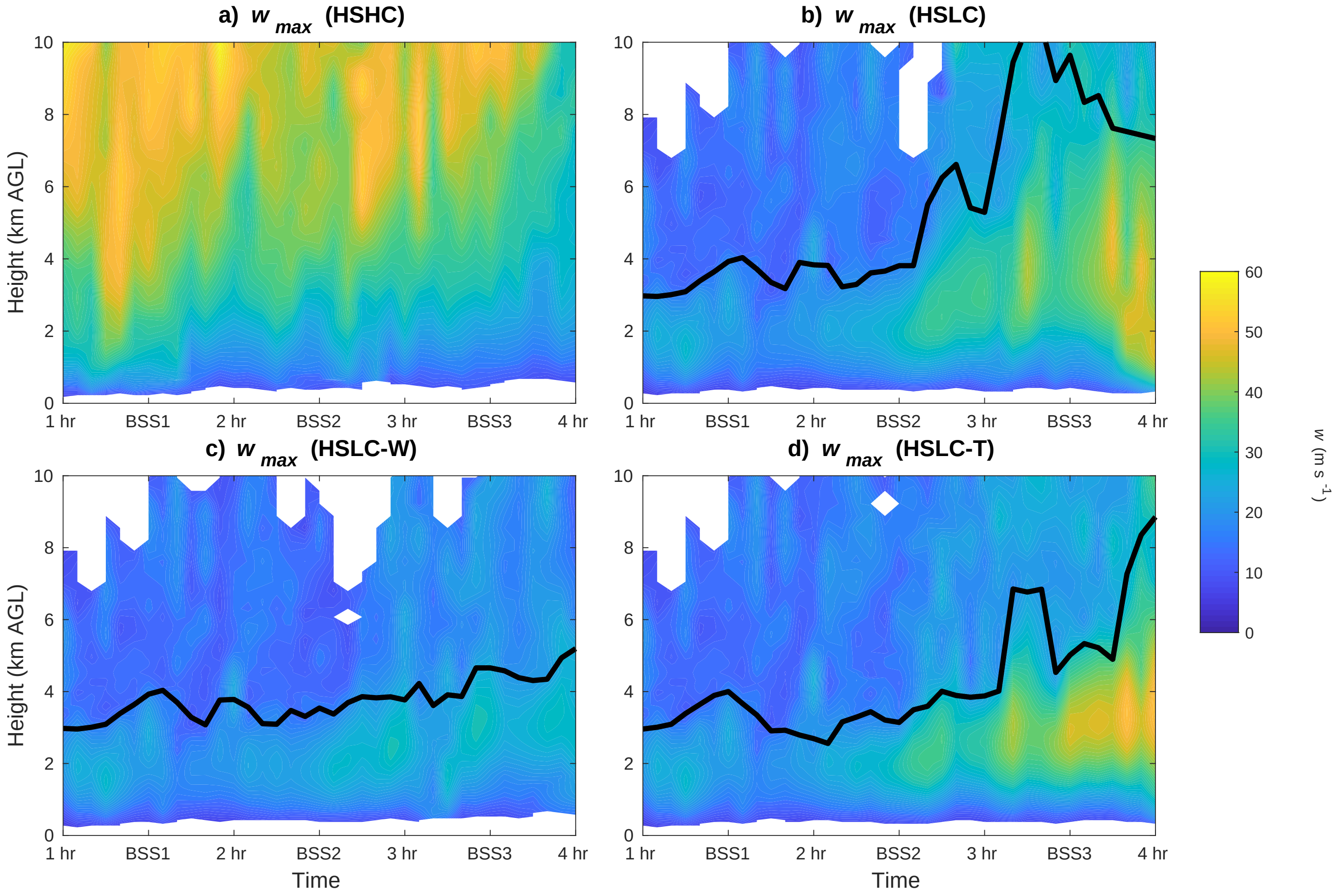

Figure 4.5: Time-height profiles of maximum vertical velocity (w_{max}; in m s^{-1}) within identified updrafts in the (a) HSHC, (b) HSLC, (c) HSLC-W and (d) HSLC-T simulations. The height at which the updraft acceleration profile $\frac{dw}{dz}$ is minimized is included (black line) to approximate the upper extent of the updraft core.

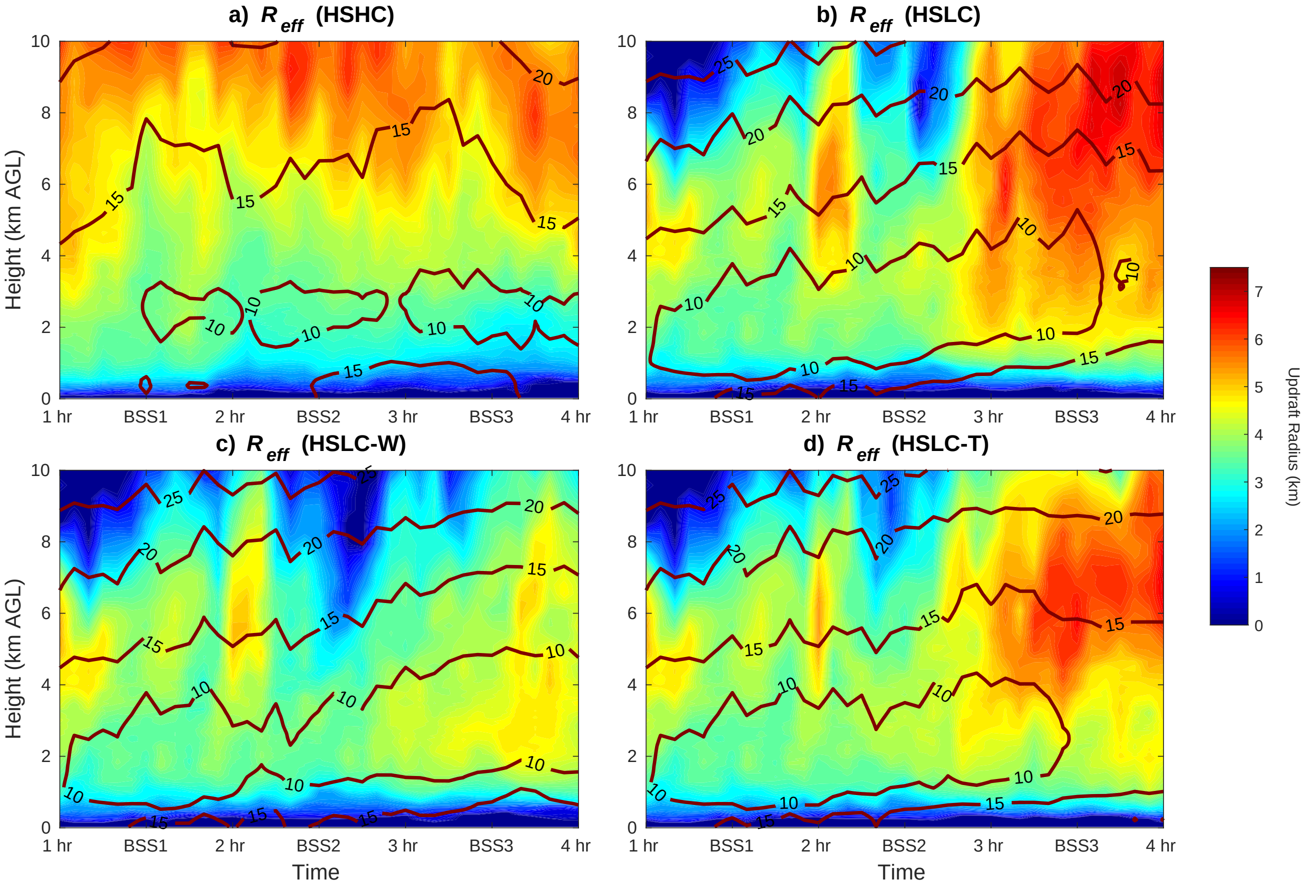

Figure 4.6: Time-height profiles of effective updraft radius (shaded; in km) and storm-relative flow (contoured; in m s^{-1}) with respect to modeled storm motion, corresponding to identified updrafts in the (a) HSHC, (b) HSLC, (c) HSLC-W and (d) HSLC-T simulations.

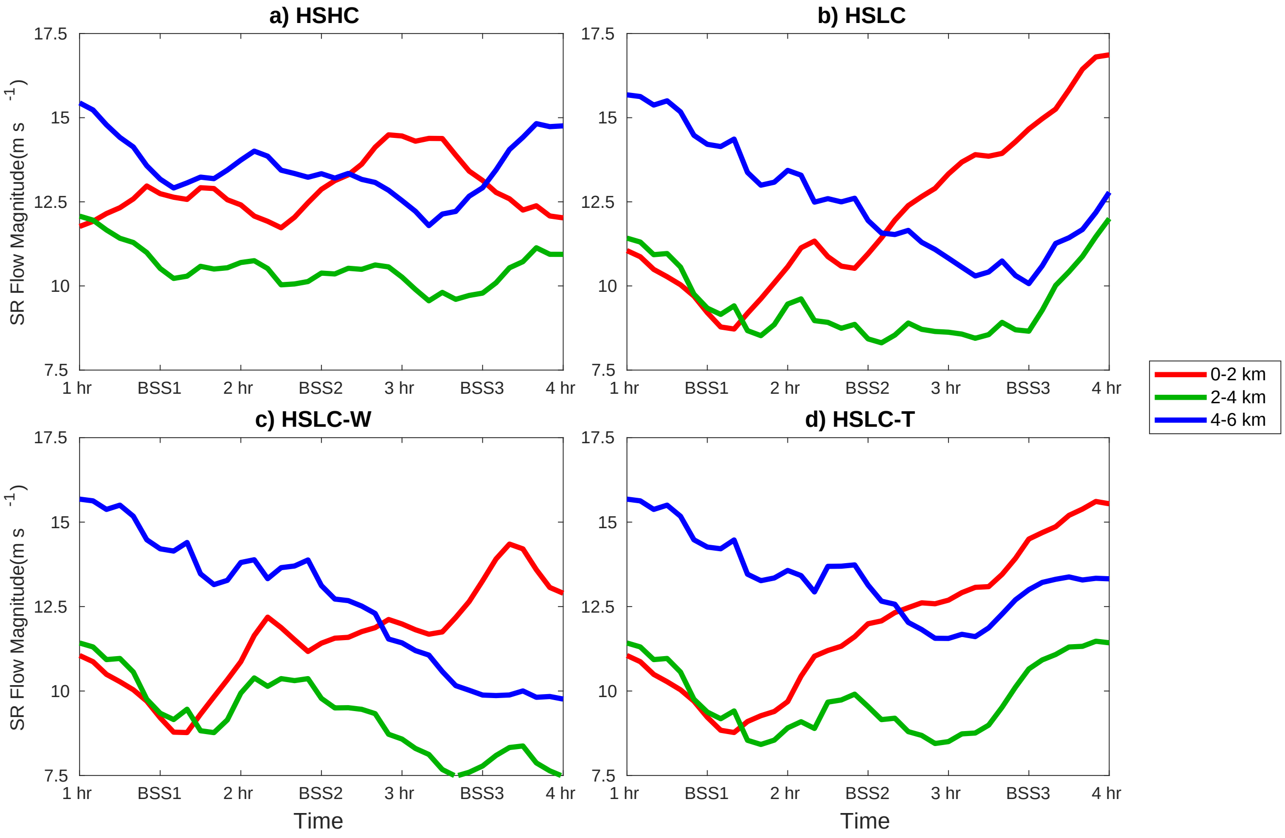

Figure 4.7: Time series of 0-2 (red), 2-4 (green) and 4-6 (blue) km AGL layer-averaged storm-relative flow in the (a) HSHC, (b) HSLC, (c) HSLC-W and (d) HSLC-T simulations.

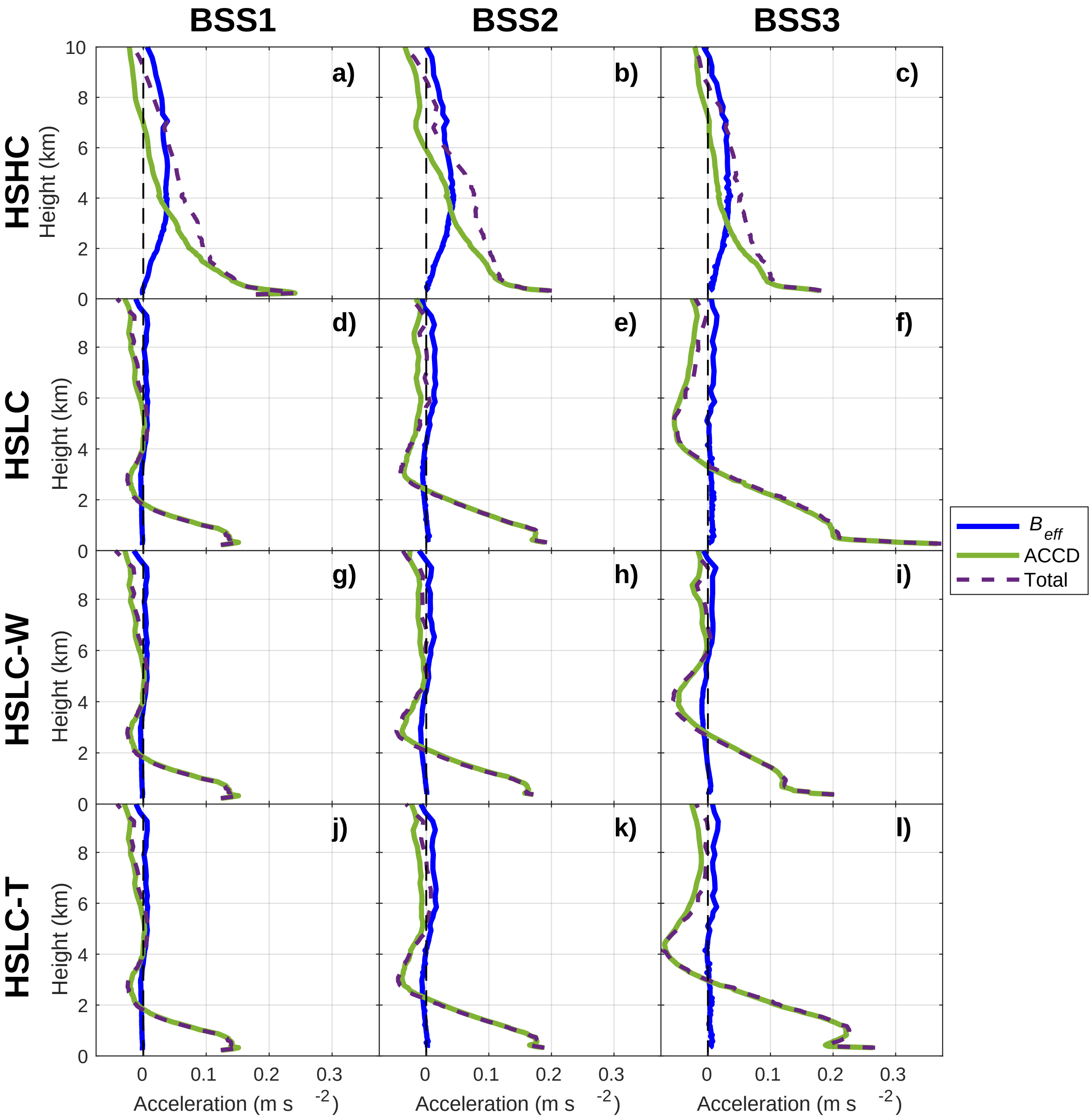

Figure 4.8: Vertical profiles of effective buoyancy (B_{Eff}, solid blue), net dynamic (ACCD, solid green), and total (dotted purple) updraft accelerations (all in m s^{-2}) ± 30 minutes from each BSS time in the (a)-(c) HSHC, (d)-(e) HSLC, (g)-(i) HSLC-W and (k)-(l) HSLC-T simulations. A zero line is included for reference (dotted black).

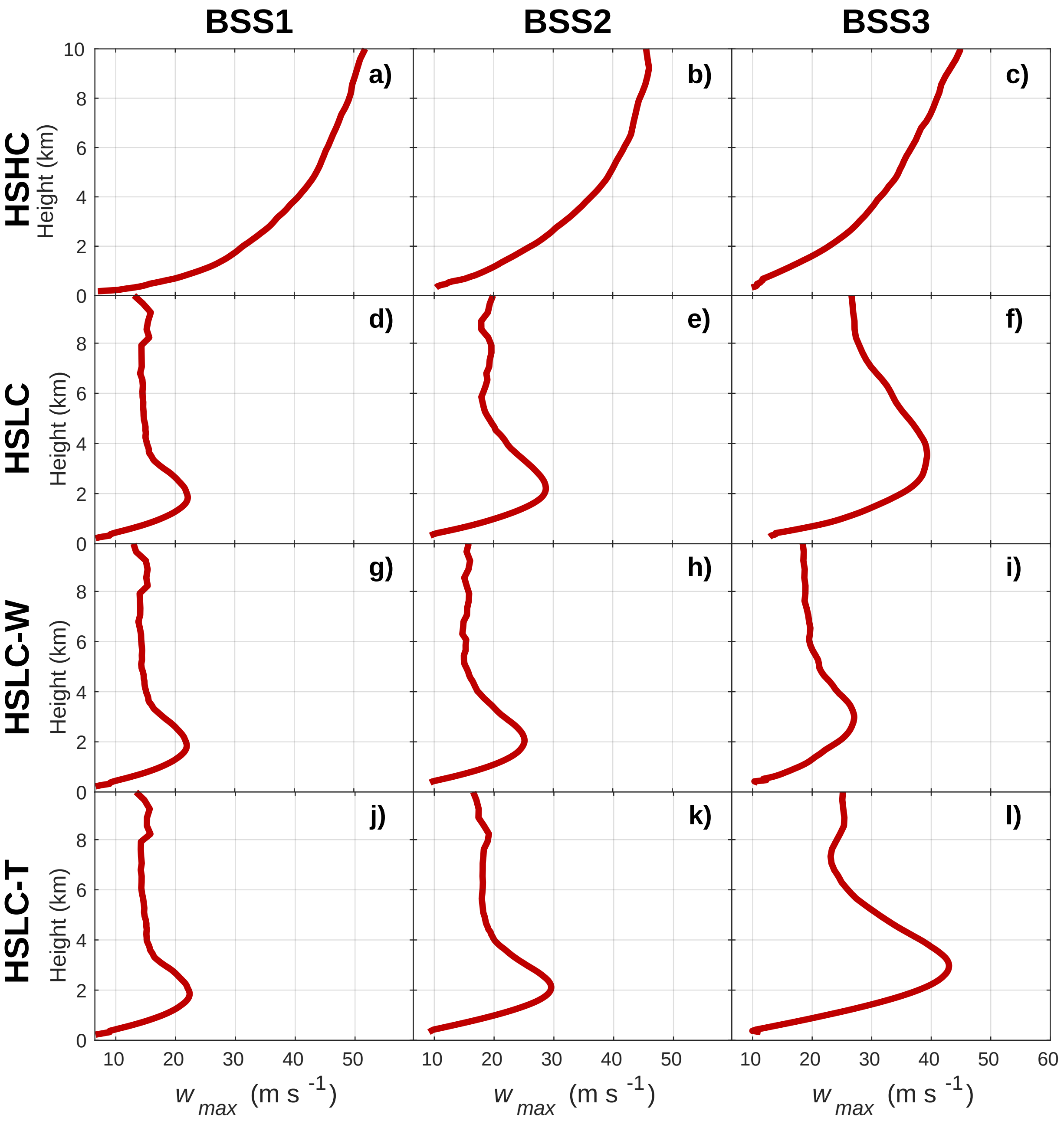

Figure 4.9: Vertical profiles of maximum updraft speed (w_{max}; in m s^{-1}) ± 30 minutes from each BSS time in the (a)-(c) HSHC, (d)-(e) HSLC, (g)-(i) HSLC-W and (k)-(l) HSLC-T simulations.

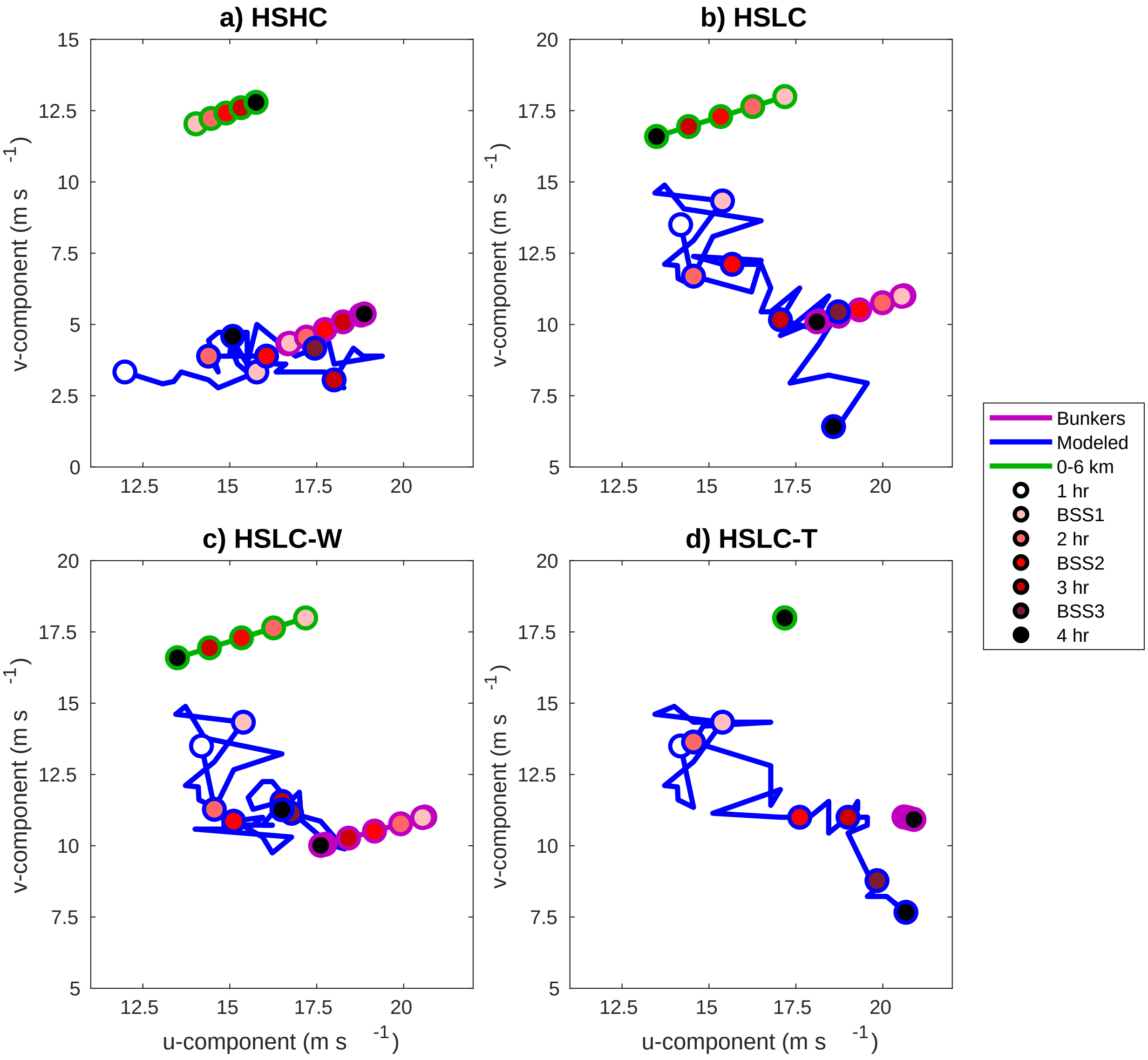

Figure 4.10: Plots of Bunker RM (in purple) and modeled storm motion (in blue) and 0-6 km mean wind (in green) vector components (in m s^{-1}), with markers shaded by model integration time (increasing darkness indicating later model times) for the (a) HSHC, (b) HSLC, (c) HSLC-W and (d) HSLC-T simulations. Note that the v-component axis for the HSLC-related simulation is shifted 5 m s^{-1} higher than the HSHC simulation, but the range of values spanned remains constant.

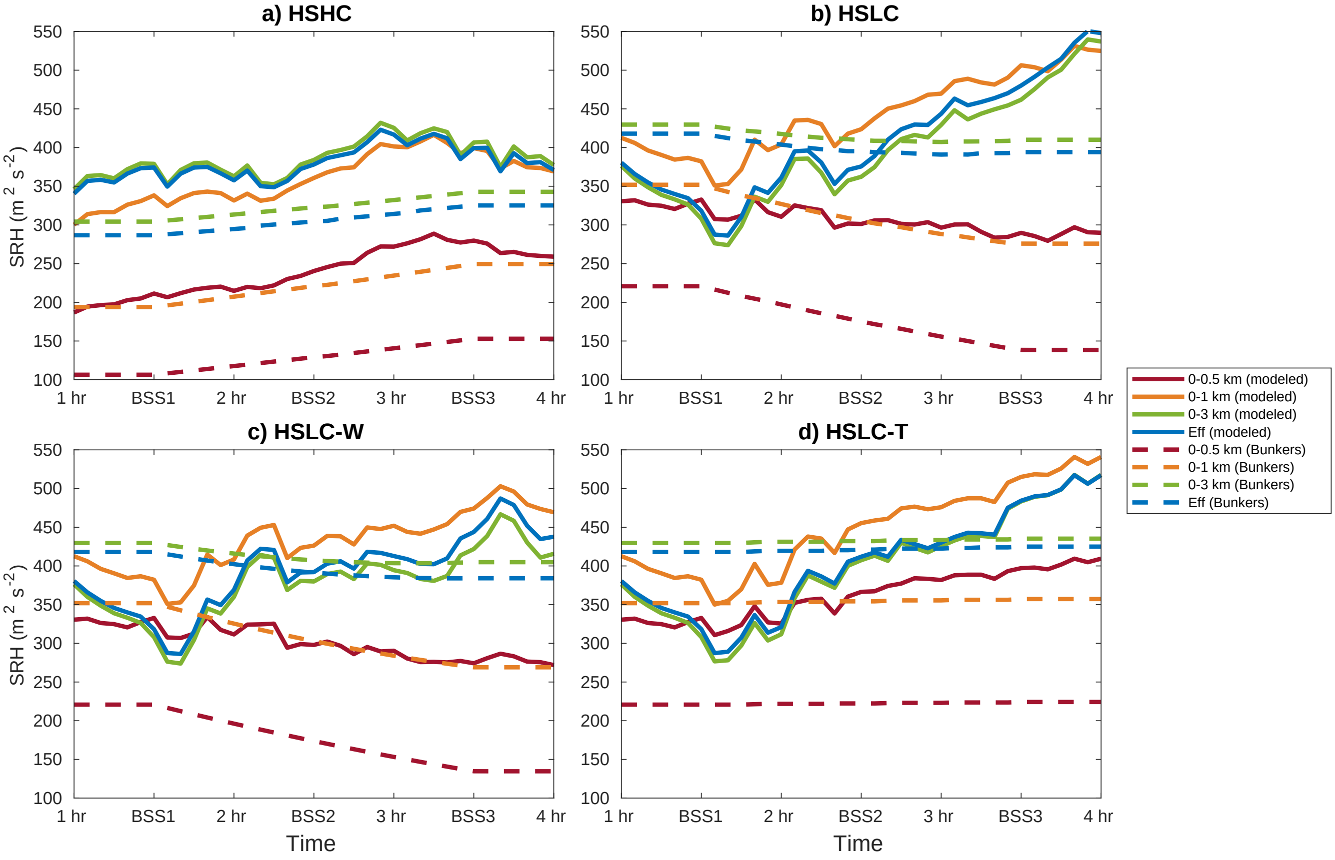

Figure 4.11: Time series of 0-0.5 km (in red), 0-1 km (in orange), 0-3 km (in green), and effective (in blue) SRH (in m^2 s^{-2}) relative to Bunker RM (dotted lines) and modeled storm motion (solid lines) for the (a) HSHC, (b) HSLC, (c) HSLC-W and (d) HSLC-T simulations.

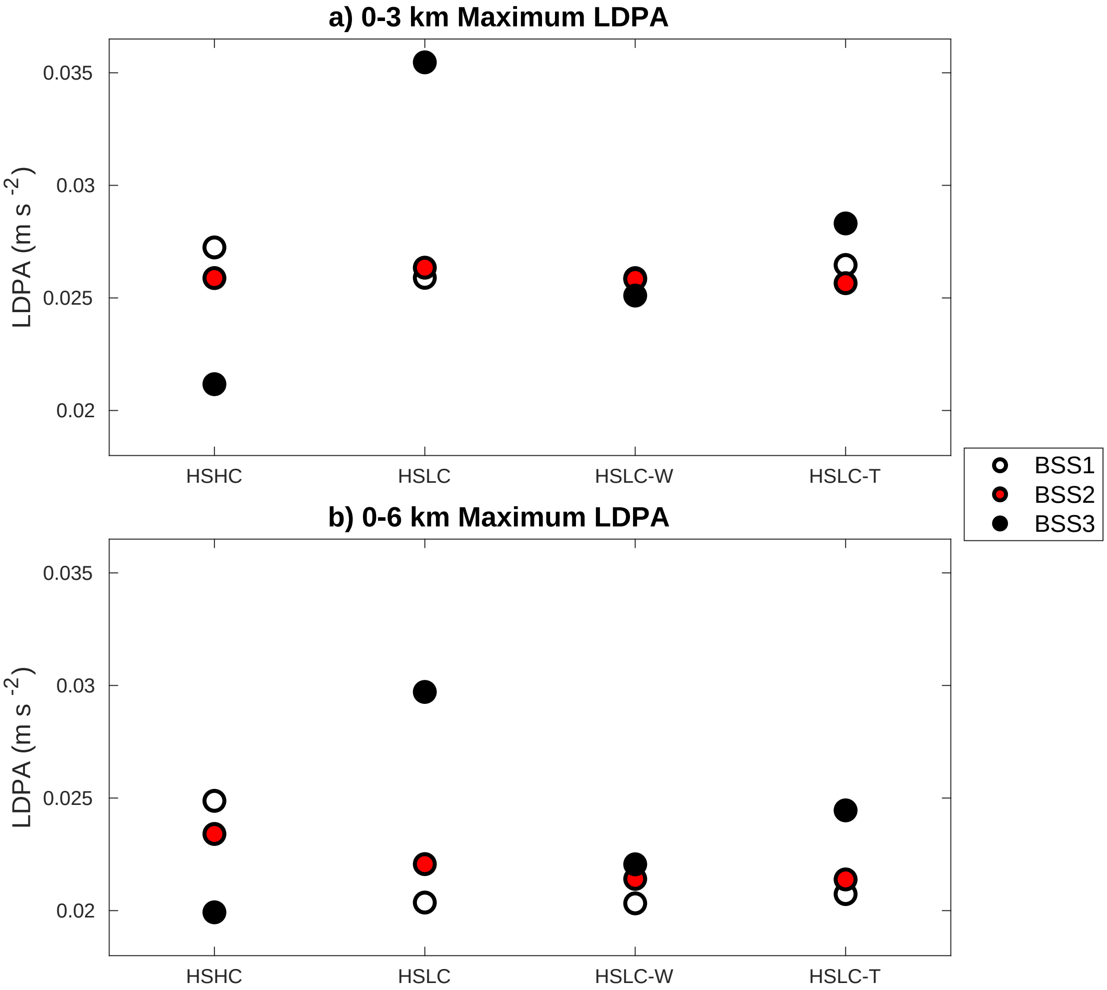

Figure 4.12: Scatter plot of (a) 0-3 km and (b) 0-6 km averaged maximum linear dynamic pressure acceleration, computed in a 25 x 25 km box centered on the 2-5 km UH maximum, ± 30 minutes from each BSS time (with darker colors representing the later BSS time) for each simulation.

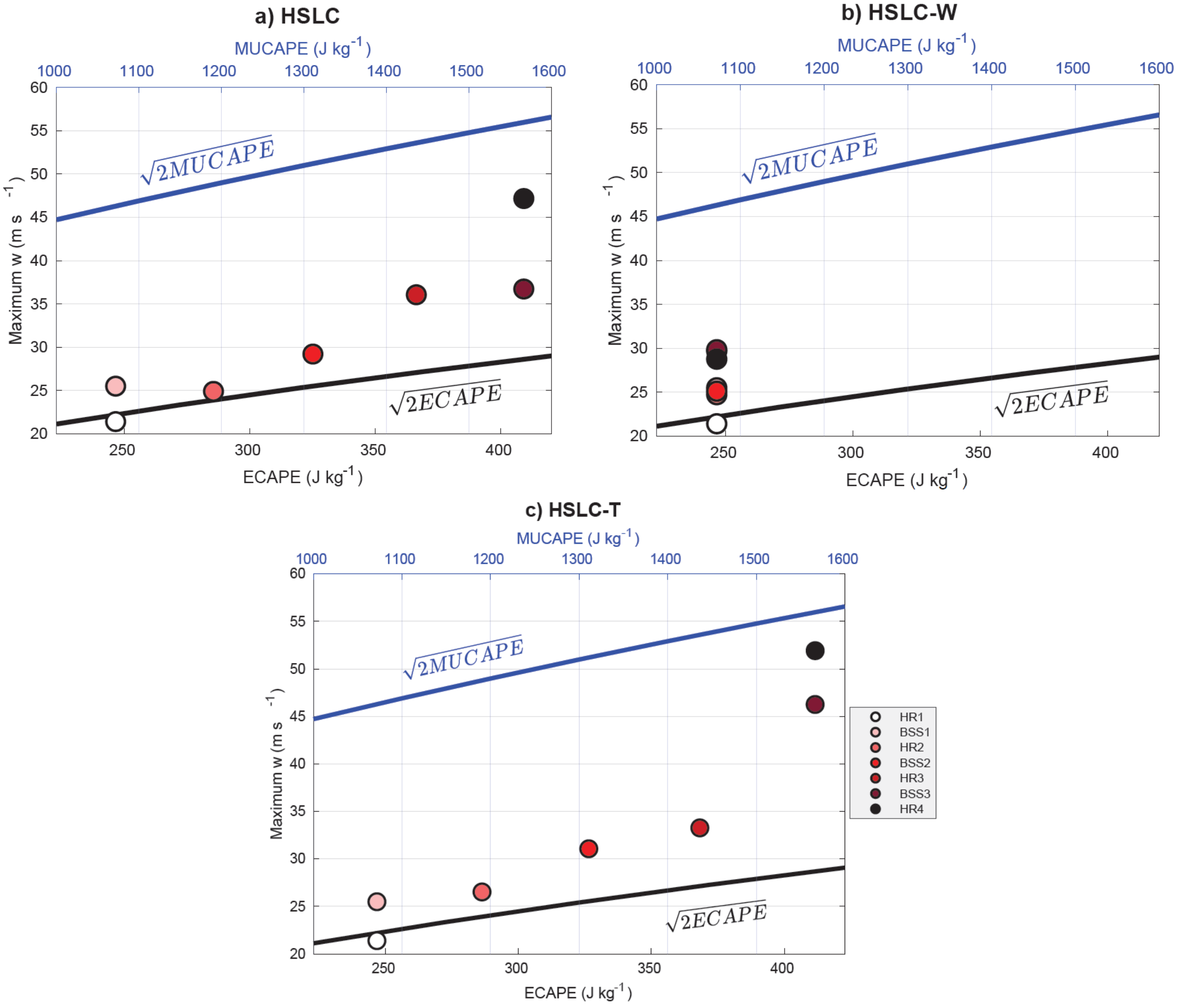

Figure 4.13: Scatter plot of base-state MUCAPE/ECAPE (in J kg^{-1}) and maximum modeled updraft speed (in m s^{-1}), with same color-timing scheme as Fig. 4.10, for the (a) HSLC, (b) HSLC-W and (c) HSLC-T simulations. The predicted updraft speeds based on the base-state MUCAPE (blue line) and ECAPE (black line) values are included for reference. Note, the ECAPE/MUCAPE analytic curves are still included on the HSLC-W plot for consistency, despite the constant CAPE values maintained in this simulation.

5. CONCLUSIONS

This work employed a variety of analysis techniques to assess how Southeast US tornado environments evolve across multiple spatiotemporal scales, and relate this evolution to subsequent storm characteristics. On the seasonal/sub-seasonal scale, teleconnection patterns were grouped using self-organizing maps to identify broad patterns of temperature, wind, and other factors uniquely related to Southeast tornado outbreaks across multiple seasons and lead times. On the regional scale, the evolution of Southeast near-storm environments and their production of severe convective hazards across the EET were considered as a function of pre-sunset CAPE and shear values. Lastly on the storm scale, these environmental pathways were incorporated into idealized simulations to characterize and compare the response of high and low-CAPE supercell updrafts to the EET. The primary findings from each of these efforts are described below.

5.1 Seasonal/sub-seasonal scale evolution

Self-organizing maps were able to identify physically relevant teleconnection patterns associated with Southeast tornado outbreaks. Large-scale modes of variability such as North Atlantic Oscillation (NAO) were related to outbreaks on longer timescales ($\sim$1-2 months) and across all analyzed seasons, whereas more localized variability like Gulf of Mexico SST anomalies were related to outbreaks on shorter timescales ($\leq$ 1 week) and specifically in cool season months. Alterations to overarching synoptic conditions – such as jet stream position and strength, trough/ridge placement, and changes in low level pressure and flow patterns – occur in tandem with these outbreak patterns. These alterations lead to a priming of the near-storm environment via increasing SRH, lowering environmental LCLs, and/or moistening the lower levels of the atmosphere. A subset of the cool season patterns contribute to the formation of HSLC tornado outbreaks (several of which span local sunset), meaning their associated large-scale environments act to limit CAPE and invigorate regional shear. This result provides a previously unexplored pathway for possible large-scale origins of CAPE deficits in widespread HSLC events, and also suggests that HSLC tornado outbreaks have more intrinsic predictability than perhaps thought before.

5.2 Regional-scale evolution

The evolution of Southeast storm environments across the EET was found to vary as a function of pre-transition CAPE and shear values. Environments with HSHC pre-transition environments exhibit the archetypal near-sunset evolution, characterized by gradually decreasing CAPE, increasing static stability, and increasing shear and SRH associated with the onset of a nocturnal low-level jet feature. In contrast, HSLC pre-transition environments tend to support overall higher shear and SRH values compared to HSHC environments (though subsequent trends vary by convective mode), paired with destabilization into the post-transition period via increasing CAPE and the removal of CIN. Pre-transition CAPE and shear values also influence the convective mode of subsequent tornadoes, with HSHC conditions favoring supercellular tornadoes while HSLC conditions favor linear mode tornadoes, particularly during the post-transition. Statistical analyses indicated that while traditional forecasting metrics such as STP retain skill for predicting HSLC tornadoes, this prediction can be advanced by incorporating additional thermodynamic information such as downdraft CAPE and precipitable water.

5.3 Storm-scale evolution

The simulated HSHC storm develops deep, strong updrafts which gradually weaken in response to the decreasing instability associated with its base-state EET evolution. HSLC storms develop noticeably shallower updrafts, but these tend to increase in depth, width, and strength with time when increases in base-state CAPE are present. These changes occur despite decreasing base-state shear and SRH, which would typically serve to weaken updraft accelerations. The primary explanation for this counterintuitive result is that the modeled HSLC storms exhibit updraft propagation that deviates rightward from Bunkers RM storm motion estimates by the end of model integration, leading to storm-relative flow and SRH values exceeding what is predicted by the base-state hodograph evolution alone. This deviant motion is supported by initially high shear and SRH pre-transition values associated with HSLC environments, paired with updraft invigoration in response to prescribed destabilization. These factors lead to HSLC updrafts whose forcing is dominated by dynamic pressure accelerations, in contrast with HSHC updrafts which are influenced heavily by dynamic accelerations near the surface and buoyancy forcing aloft. These results clarify the importance of rapid destabilization and off-hodograph propagation for HSLC updrafts, and suggest that sounding-derived quantities related to storm motion may be insufficient to predict the strength of HSLC supercell updrafts and whether they can persist through the EET.

5.4 Summary and future work

Altogether, these studies demonstrated that Southeast US environments can vary rapidly across multiple spatiotemporal scales, thus impacting the strength, persistence, convective mode, and severe convective hazards associated with their attendant convection. Perhaps more importantly, the evolution of HSLC environments and the subsequent response of convection was shown to differ relative to HSHC environments across multiple scales, highlighting the differing physical processes which govern low-CAPE storm maintenance and forcing. Each phase of this work sheds new light on these processes and advances our prediction of HSLC convective hazards – whether that be through anticipating the large-scale patterns which support cool season HSLC tornado outbreaks, understanding how HSLC environments and associated storms uniquely evolve into the evening, or clarifying the physical processes which support this nocturnal persistence of HSLC supercell updrafts.

Moving forward, there are numerous avenues for continued Southeast and HSLC storm research. Given that most severe convective research focuses on events (meaning occurrences of the hazard being studied) as opposed to non-events, it would be intriguing to consider the failure modes associated with Southeast storm environments. Within the context of this work, this could mean considering the large-scale evolution preceding instances of widespread Southeast severe convection that do not produce tornadoes, or modeling the environmental evolution of Southeast storms which only persist partway through the EET. Beyond this, high-resolution simulations determining the degree to which factors like friction or lack of strong cold pools potentially affect the development of tornado-like vortices in low-CAPE environments would provide valuable insight. These experiments would serve to further clarify what aspects of the results discussed in this dissertation and within the literature are the key discriminators for their associated phenomena (e.g., tornado outbreaks, long-lived nocturnal supercell thunderstorms, intense near-surface vortices, etc.).

Observations of Southeast US storms also need to improve. High-resolution observations of Southeast convection and their near-storm environments are few and far between, due in part to characteristically fast storm motion, complex terrain and land cover, and prevalence of nocturnal storm complexes. However, continued efforts to gather dense measurements of Southeast storms – utilizing arrays of both fixed and mobile sensors, unmanned aerial vehicles (UAVs), mobile Doppler radars when possible, and other innovative platforms – are necessary to advance our understanding of Southeast storm dynamics. In particular, three-dimensional wind retrievals would be beneficial in order to assess the validity of the updraft structures represented in this and other HSLC modeling studies. Also important are high density observations of Southeast supercell cold pools to clarify the role they play in storm maintenance and tornadogenesis, especially given the weak nature of modeled HSLC supercell cold pools. With these novel observations, we can continue to form a more complete physical model of the dynamics and maintenance of Southeast US storms across the full CAPE-shear parameter space.

REFERENCES

Agee, E., and S. Zurn-Birkhimer, 1998: Variations in USA tornado occurrences during El Niño and La Niña. *Preprints, 19th Conf. on Severe Local Storms, Minneapolis, MN, Amer. Meteor. Soc*, 287–290.

Allen, J. T., M. J. Molina, and V. A. Gensini, 2018: Modulation of annual cycle of tornadoes by El Niño–Southern Oscillation. *Geophys. Res. Lett.*, **45 (11)**, 5708–5717.

Allen, J. T., M. K. Tippett, and A. H. Sobel, 2015: Influence of the El Niño/Southern Oscillation on tornado and hail frequency in the united states. *Nature Geoscience*, **8 (4)**, 278.

Anderson-Frey, A. K., Y. P. Richardson, A. R. Dean, R. L. Thompson, and B. T. Smith, 2016: Investigation of near-storm environments for tornado events and warnings. *Wea. Forecasting*, **31 (6)**, 1771–1790.

Anderson-Frey, A. K., Y. P. Richardson, A. R. Dean, R. L. Thompson, and B. T. Smith, 2017: Self-organizing maps for the investigation of tornadic near-storm environments. *Wea. Forecasting*, **32 (4)**, 1467–1475.

Anderson-Frey, A. K., Y. P. Richardson, A. R. Dean, R. L. Thompson, and B. T. Smith, 2019: Characteristics of Tornado Events and Warnings in the Southeastern United States. *Wea. Forecasting*, **34 (4)**, 1017–1034.

Ashley, W. S., A. M. Haberlie, and J. Strohm, 2019: A climatology of quasi-linear convective systems and their hazards in the United States. *Wea. Forecasting*, **34 (6)**, 1605–1631.

Ashley, W. S., A. J. Krmenec, and R. Schwantes, 2008: Vulnerability due to nocturnal tornadoes. *Wea. Forecasting*, **23 (5)**, 795–807.

Atkins, N. T., M. L. Weisman, and L. J. Wicker, 1999: The influence of preexisting boundaries on supercell evolution. *Mon. Wea. Rev.*, **127 (12)**, 2910–2927.

Barnston, A. G., and R. E. Livezey, 1987: Classification, seasonality and persistence of low-frequency atmospheric circulation patterns. *Mon. Wea. Rev.*, **115 (6)**, 1083–1126.

Barrett, B. S., and V. A. Gensini, 2013: Variability of central United States April–May tornado day likelihood by phase of the Madden-Julian Oscillation. *Geophys. Res. Lett.*, **40 (11)**, 2790–2795.

Benjamin, S. G., and Coauthors, 2004: An hourly assimilation–forecast cycle: The RUC. *Mon. Wea. Rev.*, **132 (2)**, 495–518.

Benjamin, S. G., and Coauthors, 2016: A North American hourly assimilation and model forecast cycle: The Rapid Refresh. *Mon. Wea. Rev.*, **144 (4)**, 1669–1694.

Billings, J. M., and M. D. Parker, 2012: Evolution and maintenance of the 22–23 June 2003 nocturnal convection during BAMEX. *Wea. Forecasting*, **27 (2)**, 279–300.

Blackadar, A. K., 1957: Boundary layer wind maxima and their significance for the growth of nocturnal inversions. *Bull. Amer. Meteor. Soc*, **38 (5)**, 283–290.

Blumberg, W. G., K. T. Halbert, T. A. Supinie, P. T. Marsh, R. L. Thompson, and J. A. Hart, 2017: SHARPpy: An open-source sounding analysis toolkit for the atmospheric sciences. *Bull. Amer. Meteor. Soc*, **98 (8)**, 1625–1636.

Bothwell, P. D., J. A. Hart, and R. L. Thompson, 2002: An integrated three-dimensional objective analysis scheme in use at the Storm Prediction Center. *Preprints, 21st Conf. on Severe Local Storms, San Antonio, TX, Amer. Meteor. Soc.*, J117–J120.

Bove, M. C., 1998: Impacts of ENSO on united states tornadic activity. *Preprints, 19th Conf. on Severe Local Storms, Minneapolis, MN, Amer. Meteor. Soc. P*, 313316.

Brooks, H. E., G. W. Carbin, and P. T. Marsh, 2014: Increased variability of tornado occurrence in the United States. *Science*, **346 (6207)**, 349–352.

Brooks, H. E., C. A. Doswell III, and M. P. Kay, 2003: Climatological estimates of local daily tornado probability for the United States. *Wea. Forecasting*, **18 (4)**, 626–640.

Brotzge, J. A., S. E. Nelson, R. L. Thompson, and B. T. Smith, 2013: Tornado probability of detection and lead time as a function of convective mode and environmental parameters. *Wea. Forecasting*, **28 (5)**, 1261–1276.

Brown, M., and C. J. Nowotarski, 2019: The Influence of Lifting Condensation Level on Low-Level Outflow and Rotation in Simulated Supercell Thunderstorms. *J. Atmos. Sci.*, **76 (5)**, 1349–1372.

Brown, M. C., and C. J. Nowotarski, 2020: Southeastern US Tornado Outbreak Likelihood Using

Daily Climate Indices. *J. Climate*, **33 (8)**, 3229–3252, ©American Meteorological Society. Used with permission.

Brown, M. C., C. J. Nowotarski, A. R. Dean, B. T. Smith, R. L. Thompson, and J. M. Peters, 2021: The early evening transition in southeastern us tornado environments. *Wea. Forecasting*, **36 (4)**, 1431–1452, ©American Meteorological Society. Used with permission.

Bryan, G. H., and J. M. Fritsch, 2002: A benchmark simulation for moist nonhydrostatic numerical models. *Mon. Wea. Rev.*, **130 (12)**, 2917–2928.

Bunker, R. C., A. E. Cohen, J. A. Hart, A. E. Gerard, K. E. Klockow-McClain, and D. P. Nowicki, 2019: Examination of the predictability of nocturnal tornado events in the southeastern United States. *Wea. Forecasting*, **34 (2)**, 467–479.

Bunkers, M. J., B. A. Klimowski, J. W. Zeitler, R. L. Thompson, and M. L. Weisman, 2000: Predicting supercell motion using a new hodograph technique. *Wea. Forecasting*, **15 (1)**, 61–79.

CDC, 2012: Tornado-related fatalities–five states, Southeastern United States, April 25-28, 2011. *Morbidity Mortality Weekly Rep.*, **61 (28)**, 529.

Childs, S. J., R. S. Schumacher, and J. T. Allen, 2018: Cold-season tornadoes: Climatological and meteorological insights. *Wea. Forecasting*, **33 (3)**, 671–691.

Coffer, B. E., and M. D. Parker, 2015: Impacts of increasing low-level shear on supercells during the early evening transition. *Mon. Wea. Rev.*, **143 (5)**, 1945–1969.

Coffer, B. E., M. D. Parker, R. L. Thompson, B. T. Smith, and R. E. Jewell, 2019: Using near-ground storm relative helicity in supercell tornado forecasting. *Wea. Forecasting*, **34 (5)**, 1417–1435.

Coniglio, M. C., and M. D. Parker, 2020: Insights into supercells and their environments from three decades of targeted radiosonde observations. *Mon. Wea. Rev.*, **148 (12)**, 4893–4915.

Cook, A. R., L. M. Leslie, D. B. Parsons, and J. T. Schaefer, 2017: The impact of El Niño–Southern Oscillation (ENSO) on winter and early spring US tornado outbreaks. *J. Appl. Meteor. Climatol.*, **56 (9)**, 2455–2478.

Cook, A. R., and J. T. Schaefer, 2008: The relation of El Niño–Southern Oscillation (ENSO) to winter tornado outbreaks. *Mon. Wea. Rev.*, **136 (8)**, 3121–3137.

Corfidi, S. F., 2003: Cold pools and MCS propagation: Forecasting the motion of downwind-developing MCSs. *Wea. Forecasting*, **18 (6)**, 997–1017.

CPC, 2012: Climate Prediction Center: AAO, AO, NAO, PNA. http://www.cpc.ncep.noaa.gov/products/precip/CWlink/daily_ao_index/teleconnections.shtml.

Craven, J. P., H. E. Brooks, J. A. Hart, and Coauthors, 2004: Baseline climatology of sounding derived parameters associated with deep, moist convection. *Natl. Wea. Dig*, **28 (1)**, 13–24.

Davenport, C. E., and M. D. Parker, 2015: Impact of environmental heterogeneity on the dynamics of a dissipating supercell thunderstorm. *Mon. Wea. Rev.*, **143 (10)**, 4244–4277.

Davenport, C. E., C. L. Ziegler, and M. I. Biggerstaff, 2019: Creating a More Realistic Idealized Supercell Thunderstorm Evolution via Incorporation of Base-State Environmental Variability. *Mon. Wea. Rev.*, **147 (11)**, 4177–4198.

Davies, J. M., 2006: Tornadoes with cold core 500-mb lows. *Wea. Forecasting*, **21 (6)**, 1051–1062.

Davies, J. M., and A. Fischer, 2009: Environmental characteristics associated with nighttime tornadoes. *Electron. J. Oper. Meteor*, **10 (3)**, 1–29.

Davies, J. M., and R. H. Johns, 1993: Some wind and instability parameters associated with strong and violent tornadoes: 1. wind shear and helicity. *Washington DC American Geophysical Union Geophysical Monograph Series*, **79**, 573–582.

Davies-Jones, R., 1984: Streamwise vorticity: The origin of updraft rotation in supercell storms. *J. Atmos. Sci.*, **41 (20)**, 2991–3006.

Davies-Jones, R., 2002: Linear and nonlinear propagation of supercell storms. *J. Atmos. Sci.*, **59 (22)**, 3178–3205.

Davis, J. M., and M. D. Parker, 2014: Radar climatology of tornadic and nontornadic vortices in high-shear, low-CAPE environments in the mid-Atlantic and southeastern United States. *Wea. Forecasting*, **29 (4)**, 828–853.

Dean, A. R., and R. S. Schneider, 2008: 9a. 2 forecast challenges at the nws storm prediction center relating to the frequency of favorable severe storm environments.

Dean, A. R., and R. S. Schneider, 2012: An examination of tornado environments, events, and impacts from 2003–2012. *Preprints, 26th Conf. on Severe Local Storms, Nashville, TN, Amer. Meteor. Soc*, Vol. 60.

Doswell III, C. A., H. E. Brooks, and N. Dotzek, 2009: On the implementation of the enhanced Fujita scale in the usa. *Atmos. Res.*, **93 (1-3)**, 554–563.

Edwards, R., 2010: Tropical cyclone tornado records for the modernized NWS era. *Preprints, 25th Conf. on Severe Local Storms, Denver, CO, Amer. Meteor. Soc. P*, Vol. 3.

Edwards, R., and R. L. Thompson, 2000: RUC-2 supercell proximity soundings, Part II: An independent assessment of supercell forecast parameters. *Preprints, 20th Conf. on Severe Local Storms, Orlando, FL, Amer. Meteor. Soc*, 435–438.

Edwards, R., and S. J. Weiss, 1996: Comparisons between Gulf of Mexico sea surface temperature anomalies and southern US severe thunderstorm frequency in the cool season. *Preprints, 18th Conf. on Severe Local Storms, San Francisco, CA, Amer. Meteor. Soc*, 317–320.

Elsner, J. B., T. H. Jagger, and T. Fricker, 2016: Statistical models for tornado climatology: long and short-term views. *PloS one*, **11 (11)**, e0166 895.

ESRL: Physical Sciences Division, 2019: Forecasts of 500mb Height Teleconnection Indices, from ESRL/PSD GEFS Reforecast2 Data. https://www.esrl.noaa.gov/psd/forecasts/reforecast2/teleconn/.

Esterheld, J. M., and D. J. Giuliano, 2008: Discriminating between tornadic and non-tornadic supercells: A new hodograph technique. *EJSSM*, **3 (2)**.

Fike, P. C., 1993: A climatology of nocturnal severe local storm outbreaks. *Preprints, 17th Conf. on Severe Local Storms, St. Louis, MO, Amer. Meteor. Soc*, 10–14.

Frew, E. W., B. Argrow, S. Borenstein, S. Swenson, C. A. Hirst, H. Havenga, and A. Houston, 2020: Field observation of tornadic supercells by multiple autonomous fixed-wing unmanned aircraft. *J̇of Field Robotics*, **37 (6)**, 1077–1093.

Frye, J. D., and T. L. Mote, 2010: Convection initiation along soil moisture boundaries in the southern great plains. *Mon. Wea. Rev.*, **138 (4)**, 1140–1151.

Geerts, B., and Coauthors, 2017: The 2015 plains elevated convection at night field project. *Bull.*

Amer. Meteor. Soc., **98 (4)**, 767–786.

Gensini, V. A., and A. Marinaro, 2016: Tornado frequency in the United States related to global relative angular momentum. *Mon. Wea. Rev.*, **144 (2)**, 801–810.

Gilmore, M. S., and L. J. Wicker, 1998: The influence of midtropospheric dryness on supercell morphology and evolution. *Mon. Wea. Rev.*, **126 (4)**, 943–958.

Gray, K., and J. Frame, 2019: Investigating the Transition from Elevated Multicellular Convection to Surface-Based Supercells during the Tornado Outbreak of 24 August 2016 Using a WRF Model Simulation. *Wea. Forecasting*, **34 (4)**, 1051–1079.

Gropp, M. E., and C. E. Davenport, 2018: The impact of the nocturnal transition on the lifetime and evolution of supercell thunderstorms in the Great Plains. *Wea. Forecasting*, **33 (4)**, 1045–1061.

Guarriello, F., C. J. Nowotarski, and C. C. Epifanio, 2018: Effects of the low-level wind profile on outflow position and near-surface vertical vorticity in simulated supercell thunderstorms. *J. Atmos. Sci.*, **75 (3)**, 731–753.

Guyer, J. L., and A. R. Dean, 2010: Tornadoes Within Weak CAPE Environments Across The Continental United States. *Preprints, 25th Conf. on Severe Local Storms, Denver, CO, Amer. Meteor. Soc*, 1.5.

Guyer, J. L., D. A. Imy, A. Kis, and K. Venable, 2006: Cool Season Significant (F2-F5) Tornadoes in the Gulf Coast states. *Preprints, 23rd Conf. on Severe Local Storms, St. Louis, MO, Amer. Meteor. Soc*, 4.2.

Hart, J. A., and W. Korotky, 1991: The SHARP workstation v1. 50 users guide. *NOAA/NWS*.

Holton, J. R., 1967: The diurnal boundary layer wind oscillation above sloping terrain. *Tellus*, **19 (2)**, 200–205.

Johns, R. H., and C. A. Doswell III, 1992: Severe local storms forecasting. *Wea. Forecasting*, **7 (4)**, 588–612.

Jung, E., and B. P. Kirtman, 2016: Can we predict seasonal changes in high impact weather in the United States? *Environ. Res. Lett.*, **11 (7)**, 074 018.

Katsumata, M., R. H. Johnson, and P. E. Ciesielski, 2009: Observed synoptic-scale variability during the developing phase of an ISO over the Indian Ocean during MISMO. *J. Atmos. Sci.*, **66 (11)**, 3434–3448.

Kelly, D. L., J. T. Schaefer, R. P. McNulty, C. A. Doswell III, and R. F. Abbey Jr, 1978: An augmented tornado climatology. *Mon. Wea. Rev.*, **106 (8)**, 1172–1183.

King, J. R., M. D. Parker, K. D. Sherburn, and G. M. Lackmann, 2017: Rapid evolution of cool season, low-CAPE severe thunderstorm environments. *Wea. Forecasting*, **32 (2)**, 763–779.

Kis, A. K., and J. M. Straka, 2010: Nocturnal tornado climatology. *Wea. Forecasting*, **25 (2)**, 545–561.

Klemp, J. B., 1987: Dynamics of tornadic thunderstorms. *Annual review of fluid mechanics*, **19 (1)**, 369–402.

Kloth, C. M., and R. Davies-Jones, 1980: *The relationship of the 300-mb jet stream to tornado occurrence*. NOAA Tech. Memo. ERL NSSL-88, 62 pp.

Knowles, J. B., and R. A. Pielke, 2005: *The Southern Oscillation and its effect on tornadic activity in the United States*. Colorado State University Atmospheric Sciences Paper.

Knupp, K. R., and Coauthors, 2014: Meteorological overview of the devastating 27 April 2011 tornado outbreak. *Bull. Amer. Meteor. Soc.*, **95 (7)**, 1041–1062.

Kohonen, T., 1995: Self-Organizing Maps. Springer, 392 pp.

Lee, S. K., R. Atlas, D. Enfield, C. Wang, and H. Liu, 2013: Is there an optimal ENSO pattern that enhances large-scale atmospheric processes conducive to tornado outbreaks in the United States? *J. Climate*, **26 (5)**, 1626–1642.

Lehmiller, G. S., H. B. Bluestein, P. J. Neiman, F. M. Ralph, and W. F. Feltz, 2001: Wind structure in a supercell thunderstorm as measured by a UHF wind profiler. *Mon. Wea. Rev.*, **129 (8)**, 1968–1986.

Lemon, L. R., and C. A. Doswell III, 1979: Severe thunderstorm evolution and mesocyclone structure as related to tornadogenesis. *Mon. Wea. Rev.*, **107 (9)**, 1184–1197.

MacIntosh, C. W., and M. D. Parker, 2017: The 6 May 2010 elevated supercell during VORTEX2. *Mon. Wea. Rev.*, **145 (7)**, 2635–2657.

Maddox, R. A., 1983: Large-scale meteorological conditions associated with midlatitude, mesoscale convective complexes. *Mon. Wea. Rev.*, **111 (7)**, 1475–1493.

Maddox, R. A., 1993: Diurnal low-level wind oscillation and storm-relative helicity. *Washington DC American Geophysical Union Geophysical Monograph Series*, **79**, 591–598.

Maddox, R. A., and C. A. Doswell III, 1982: An examination of jet stream configurations, 500 mb vorticity advection and low-level thermal advection patterns during extended periods of intense convection. *Mon. Wea. Rev.*, **110 (3)**, 184–197.

Mansell, E. R., C. L. Ziegler, and E. C. Bruning, 2010: Simulated electrification of a small thunderstorm with two-moment bulk microphysics. *J. Atmos. Sci.*, **67 (1)**, 171–194.

Markowski, P., C. Hannon, J. Frame, E. Lancaster, A. Pietrycha, R. Edwards, and R. L. Thompson, 2003: Characteristics of vertical wind profiles near supercells obtained from the Rapid Update Cycle. *Wea. Forecasting*, **18 (6)**, 1262–1272.

Markowski, P., and Coauthors, 2012: The pretornadic phase of the Goshen County, Wyoming, supercell of 5 June 2009 intercepted by VORTEX2. Part II: Intensification of low-level rotation. *Mon. Wea. Rev.*, **140 (9)**, 2916–2938.

Markowski, P. M., E. N. Rasmussen, and J. M. Straka, 1998a: The occurrence of tornadoes in supercells interacting with boundaries during vortex-95. *Wea. Forecasting*, **13 (3)**, 852–859.

Markowski, P. M., and Y. P. Richardson, 2014: The influence of environmental low-level shear and cold pools on tornadogenesis: Insights from idealized simulations. *J. Atmos. Sci.*, **71 (1)**, 243–275.

Markowski, P. M., J. M. Straka, and E. N. Rasmussen, 2002: Direct surface thermodynamic observations within the rear-flank downdrafts of nontornadic and tornadic supercells. *Mon. Wea. Rev.*, **130 (7)**, 1692–1721.

Markowski, P. M., J. M. Straka, E. N. Rasmussen, and D. O. Blanchard, 1998b: Variability of storm-relative helicity during VORTEX. *Mon. Wea. Rev.*, **126 (11)**, 2959–2971.

Marzban, C., and J. T. Schaefer, 2001: The correlation between US tornadoes and Pacific sea surface temperatures. *Mon. Wea. Rev.*, **129 (4)**, 884–895.

Mason, I., 1982: A model for assessment of weather forecasts. *Aust. Meteor. Mag*, **30 (4)**, 291–303.

May, O. W., and A. B. Bigham, 2012: After the storm: Personal experiences following an EF4 tornado. *J. Pediatr. Nurs.*, **27 (4)**, 390–393.

McCaul Jr, E. W., and M. L. Weisman, 1996: Simulations of shallow supercell storms in landfalling hurricane environments. *Mon. Wea. Rev.*, **124 (3)**, 408–429.

McCaul Jr, E. W., and M. L. Weisman, 2001: The sensitivity of simulated supercell structure and intensity to variations in the shapes of environmental buoyancy and shear profiles. *Mon. Wea. Rev.*, **129 (4)**, 664–687.

McDonald, J. M., and C. C. Weiss, 2021: Cold Pool Characteristics of Tornadic Quasi-Linear Convective Systems and Other Convective Modes Observed during VORTEX-SE. *Mon. Wea. Rev.*, **149 (3)**, 821–840.

Mead, C., and R. Thompson, 2011: Environmental characteristics associated with nocturnal significant-tornado events in the Great Plains. *Electron. J. Severe Storms Meteor.*, **6 (6)**.

Mesinger, F., and Coauthors, 2006: North American regional reanalysis. *Bull. Amer. Meteor. Soc.*, **87 (3)**, 343–360.

Miller, R. C., 1972: Notes on analysis and severe-storm forecasting procedures of the Air Force Global Weather Central. Tech. rep., AIR WEATHER SERVICE SCOTT AFB IL.

Molina, M. J., and J. T. Allen, 2019: On the Moisture Origins of Tornadic Thunderstorms. *J. Climate*, **32 (14)**, 4321–4346.

Molina, M. J., J. T. Allen, and V. A. Gensini, 2018: The Gulf of Mexico and ENSO influence on subseasonal and seasonal CONUS winter tornado variability. *J. Appl. Meteor. Climatol.*, **57 (10)**, 2439–2463.

Molina, M. J., R. P. Timmer, and J. T. Allen, 2016: Importance of the Gulf of Mexico as a climate driver for US severe thunderstorm activity. *Geophys. Res. Lett.*, **43 (23)**.

Munoz, E., and D. Enfield, 2011: The boreal spring variability of the Intra-Americas low-level jet and its relation with precipitation and tornadoes in the eastern United States. *Climate Dyn.*, **36 (1-2)**, 247–259.

Murphy, T. A., and K. R. Knupp, 2013: An analysis of cold season supercell storms using the synthetic dual-Doppler technique. *Mon. Wea. Rev.*, **141 (2)**, 602–624.

Naylor, J., and M. S. Gilmore, 2012: Convective initiation in an idealized cloud model using an updraft nudging technique. *Mon. Wea. Rev.*, **140 (11)**, 3699–3705.

Nowotarski, C. J., and A. A. Jensen, 2013: Classifying proximity soundings with self-organizing maps toward improving supercell and tornado forecasting. *Wea. Forecasting*, **28 (3)**, 783–801.

Nowotarski, C. J., and E. A. Jones, 2018: Multivariate self-organizing map approach to classifying supercell tornado environments using near-storm, low-level wind and thermodynamic profiles. *Wea. Forecasting*, **33 (3)**, 661–670.

Nowotarski, C. J., P. M. Markowski, and Y. P. Richardson, 2011: The characteristics of numerically simulated supercell storms situated over statically stable boundary layers. *Mon. Wea. Rev.*, **139 (10)**, 3139–3162.

Nowotarski, C. J., J. M. Peters, and J. P. Mulholland, 2020: Evaluating the effective inflow layer of simulated supercell updrafts. *Mon. Wea. Rev.*, **148 (8)**, 3507–3532.

Nunn, K. H., and A. T. DeGaetano, 2004: The El Niño–Southern Oscillation and its role in cold-season tornado outbreak climatology. *Preprints, 15th Symp. on Global and Climate Change and 14th Conf. on Applied Climatology, Seattle, WA, Amer. Meteor. Soc., JP5*, Vol. 2.

Papadopoulos, A., A. K. Paschalidou, P. A. Kassomenos, and G. McGregor, 2014: On the association between synoptic circulation and wildfires in the Eastern Mediterranean. *Theoretical and applied climatology*, **115 (3-4)**, 483–501.

Parker, M. D., 2014: Composite VORTEX2 supercell environments from near-storm soundings. *Mon. Wea. Rev.*, **142 (2)**, 508–529.

Peters, J. M., K. C. Eure, and R. S. Schumacher, 2017: Factors that drive MCS growth from supercells. *17th Conf. on Mesoscale Processes*.

Peters, J. M., H. Morrison, C. J. Nowotarski, J. P. Mulholland, and R. L. Thompson, 2020a: A formula for the maximum vertical velocity in supercell updrafts. *J. Atmos. Sci.*, **77 (11)**, 3747–3757.

Peters, J. M., C. J. Nowotarski, and H. Morrison, 2019: The role of vertical wind shear in modulating maximum supercell updraft velocities. *J. Atmos. Sci.*, **76 (10)**, 3169–3189.

Peters, J. M., C. J. Nowotarski, J. P. Mulholland, and R. L. Thompson, 2020b: The influences of effective inflow layer streamwise vorticity and storm-relative flow on supercell updraft properties. *J. Atmos. Sci.*, **77 (9)**, 3033–3057.

Rasmussen, E. N., 2003: Refined supercell and tornado forecast parameters. *Wea. Forecasting*, **18 (3)**, 530–535.

Rasmussen, E. N., and D. O. Blanchard, 1998: A baseline climatology of sounding-derived supercell and tornado forecast parameters. *Wea. Forecasting*, **13 (4)**, 1148–1164.

Rasmusson, E. M., 1967: Atmospheric water vapor transport and the water balance of North America: Part I. Characteristics of the water vapor flux field. *Mon. Wea. Rev.*, **95 (7)**, 403–426.

Reynolds, R. W., T. M. Smith, C. Liu, D. B. Chelton, K. S. Casey, and M. G. Schlax, 2007: Daily high-resolution-blended analyses for sea surface temperature. *J. Climate*, **20 (22)**, 5473–5496.

Roebber, P. J., 2009: Visualizing multiple measures of forecast quality. *Wea. Forecasting*, **24 (2)**, 601–608.

Ropelewski, C. F., and M. S. Halpert, 1986: North American precipitation and temperature patterns associated with the El Niño/Southern Oscillation (ENSO). *Mon. Wea. Rev.*, **114 (12)**, 2352–2362.

Rotunno, R., and J. Klemp, 1985: On the rotation and propagation of simulated supercell thunderstorms. *J. Atmos. Sci.*, **42 (3)**, 271–292.

Rotunno, R., and J. B. Klemp, 1982: The influence of the shear-induced pressure gradient on thunderstorm motion. *Mon. Wea. Rev.*, **110 (2)**, 136–151.

Rotunno, R., J. B. Klemp, and M. L. Weisman, 1988: A theory for strong, long-lived squall lines. *J. Atmos. Sci.*, **45 (3)**, 463–485.

Sankovich, V., J. T. Schaefer, and J. J. Levit, 2004: A Comparison of Rawinsonde Data from the Southeastern United States During El Nino, La Nina, and Neutral Winters. Preprints. *22nd Conference of Severe Local Storms, Hyannis, MA.*

Schaefer, J. T., 1986: Severe thunderstorm forecasting: A historical perspective. *Wea. Forecasting*,

1 (3), 164–189.

Schaefer, J. T., and R. Edwards, 1999: The SPC tornado/severe thunderstorm database. *Preprints, 11th Conf. on Applied Climatology, Dallas, TX, Amer. Meteor. Soc*, Vol. 6.

Schaefer, J. T., D. L. Kelly, C. A. Doswell III, J. G. Galway, R. J. Williams, R. P. McNulty, L. R. Lemon, and B. D. Lambert, 1980: Tornadoes, when, where, how often. *Weatherwise*, **33**, 52–59.

Schaefer, J. T., and F. B. Tatom, 1999: The relationship between El Niño, La Niña, and United States tornado activity. *Prepared for the 19 th Conference on Severe Local Storms, Minneapolis, MN.*

Schaumann, J., and R. W. Przybylinski, 2012: Operational application of 0-3 km bulk shear vectors in assessing quasi-linear convective system mesovortex and tornado potential. *26th Conf. on Severe Local Storms, Nashville, TN, Amer. Meteor. Soc.*, Vol. 142.

Schenkman, A. D., M. Xue, and M. Hu, 2014: Tornadogenesis in a high-resolution simulation of the 8 May 2003 Oklahoma City supercell. *J. Atmos. Sci.*, **71 (1)**, 130–154.

Shabbott, C. J., and P. M. Markowski, 2006: Surface in situ observations within the outflow of forward-flank downdrafts of supercell thunderstorms. *Mon. Wea. Rev*, **134 (5)**, 1422–1441.

Shapiro, A., E. Fedorovich, and S. Rahimi, 2016: A unified theory for the great plains nocturnal low-level jet. *J. Atmos. Sci.*, **73 (8)**, 3037–3057.

Sherburn, K. D., and M. D. Parker, 2014: Climatology and ingredients of significant severe convection in high-shear, low-CAPE environments. *Wea. Forecasting*, **29 (4)**, 854–877.

Sherburn, K. D., and M. D. Parker, 2019: The Development of Severe Vortices within Simulated High-Shear, Low-CAPE Convection. *Mon. Wea. Rev.*, **147 (6)**, 2189–2216.

Sherburn, K. D., M. D. Parker, J. R. King, and G. M. Lackmann, 2016: Composite environments of severe and nonsevere high-shear, low-CAPE convective events. *Wea. Forecasting*, **31 (6)**, 1899–1927.

Simmons, K. M., and D. Sutter, 2007: Tornado shelters and the housing market. *Construction Management and Economics*, **25 (11)**, 1119–1126.

Smith, B. T., R. L. Thompson, J. S. Grams, C. Broyles, and H. E. Brooks, 2012: Convective modes for significant severe thunderstorms in the contiguous united states. part i: Storm classification and climatology. *Wea. Forecasting*, **27 (5)**, 1114–1135.

Smith, S. R., P. M. Green, A. P. Leonardi, and J. J. OBrien, 1998: Role of multiple-level tropospheric circulations in forcing ENSO winter precipitation anomalies. *Mon. Wea. Rev.*, **126 (12)**, 3102–3116.

Strader, S. M., W. S. Ashley, T. J. Pingel, and A. J. Krmenec, 2017: Observed and projected changes in United States tornado exposure. *Weather, Climate, and Society*, **9 (2)**, 109–123.

Thompson, D. B., and P. E. Roundy, 2013: The relationship between the Madden–Julian oscillation and US violent tornado outbreaks in the spring. *Mon. Wea. Rev.*, **141 (6)**, 2087–2095.

Thompson, R. L., and R. Edwards, 2000: An overview of environmental conditions and forecast implications of the 3 May 1999 tornado outbreak. *Wea. Forecasting*, **15 (6)**, 682–699.

Thompson, R. L., R. Edwards, J. A. Hart, K. L. Elmore, and P. Markowski, 2003: Close proximity soundings within supercell environments obtained from the Rapid Update Cycle. *Wea. Forecasting*, **18 (6)**, 1243–1261.

Thompson, R. L., J. M. Lewis, and R. A. Maddox, 1994: Autumnal return of tropical air to the Gulf of Mexico's coastal plain. *Wea. Forecasting*, **9 (3)**, 348–360.

Thompson, R. L., C. M. Mead, and R. Edwards, 2007: Effective storm-relative helicity and bulk shear in supercell thunderstorm environments. *Wea. Forecasting*, **22 (1)**, 102–115.

Thompson, R. L., B. T. Smith, A. R. Dean, and P. T. Marsh, 2013: Spatial distributions of tornadic near-storm environments by convective mode. *EJSSM*, **8 (5)**.

Thompson, R. L., B. T. Smith, J. S. Grams, A. R. Dean, and C. Broyles, 2012: Convective modes for significant severe thunderstorms in the contiguous United States. Part II: Supercell and QLCS tornado environments. *Wea. Forecasting*, **27 (5)**, 1136–1154.

Thompson, R. L., and Coauthors, 2017: Tornado damage rating probabilities derived from WSR-88D data. *Wea. Forecasting*, **32 (4)**, 1509–1528.

Tippett, M. K., 2018: Robustness of Relations between the MJO and US Tornado Occurrence. *Mon. Wea. Rev.*, **146 (11)**, 3873–3884.

Trapp, R. J., and K. A. Hoogewind, 2018: Exploring a possible connection between US tornado activity and Arctic sea ice. *Nature*, **1 (1)**, 14.

Trapp, R. J., S. A. Tessendorf, E. S. Godfrey, and H. E. Brooks, 2005: Tornadoes from squall lines and bow echoes. Part I: Climatological distribution. *Wea. Forecasting*, **20 (1)**, 23–34.

Uccellini, L. W., and D. R. Johnson, 1979: The coupling of upper and lower tropospheric jet streaks and implications for the development of severe convective storms. *Mon. Wea. Rev.*, **107 (6)**, 682–703.

Verbout, S. M., H. E. Brooks, L. M. Leslie, and D. M. Schultz, 2006: Evolution of the US tornado database: 1954–2003. *Wea. Forecasting*, **21 (1)**, 86–93.

Vesanto, J., J. Himberg, E. Alhoniemi, and J. Parhankangas, 2000: SOM toolbox for Matlab 5. *Helsinki University of Technology, Finland*, **109**.

Wade, A. R., and M. D. Parker, 2021: Dynamics of simulated high-shear, low-cape supercells. *Journal of the Atmospheric Sciences*, **78 (5)**, 1389–1410.

Warren, R. A., H. Richter, H. A. Ramsay, S. T. Siems, and M. J. Manton, 2017: Impact of variations in upper-level shear on simulated supercells. *Mon. Wea. Rev.*, **145 (7)**, 2659–2681.

Weisman, M. L., and J. B. Klemp, 1982: The dependence of numerically simulated convective storms on vertical wind shear and buoyancy. *Monthly Weather Review*, **110 (6)**, 504–520.

Weisman, M. L., and J. B. Klemp, 1984: The structure and classification of numerically simulated convective stormsin directionally varying wind shears. *Mon. Wea. Rev.*, **112 (12)**, 2479–2498.

Weisman, M. L., and R. Rotunno, 2000: The use of vertical wind shear versus helicity in interpreting supercell dynamics. *J. Atmos. Sci.*, **57 (9)**, 1452–1472.

Wilks, D. S., 2011: *Statistical Methods in the Atmospheric Sciences*, Vol. 100. Academic Press.

Williams, B. M., J. S. Allen, and J. W. Zeitler, 2018: Anticipating QLCS Tornadogenesis for Decision Support: The Three-Ingredient Method During the 19-20 February 2017 South-Central Texas Tornadic QLCS Event. *Preprints, 98th Amer. Meteor. Soc. Annual Meeting, Austin, TX.*

Ziegler, C. L., E. R. Mansell, J. M. Straka, D. R. MacGorman, and D. W. Burgess, 2010: The impact of spatial variations of low-level stability on the life cycle of a simulated supercell storm.

Mon. Wea. Rev., **138 (5)**, 1738–1766.

APPENDIX A

CHAPTER 2 APPENDIX

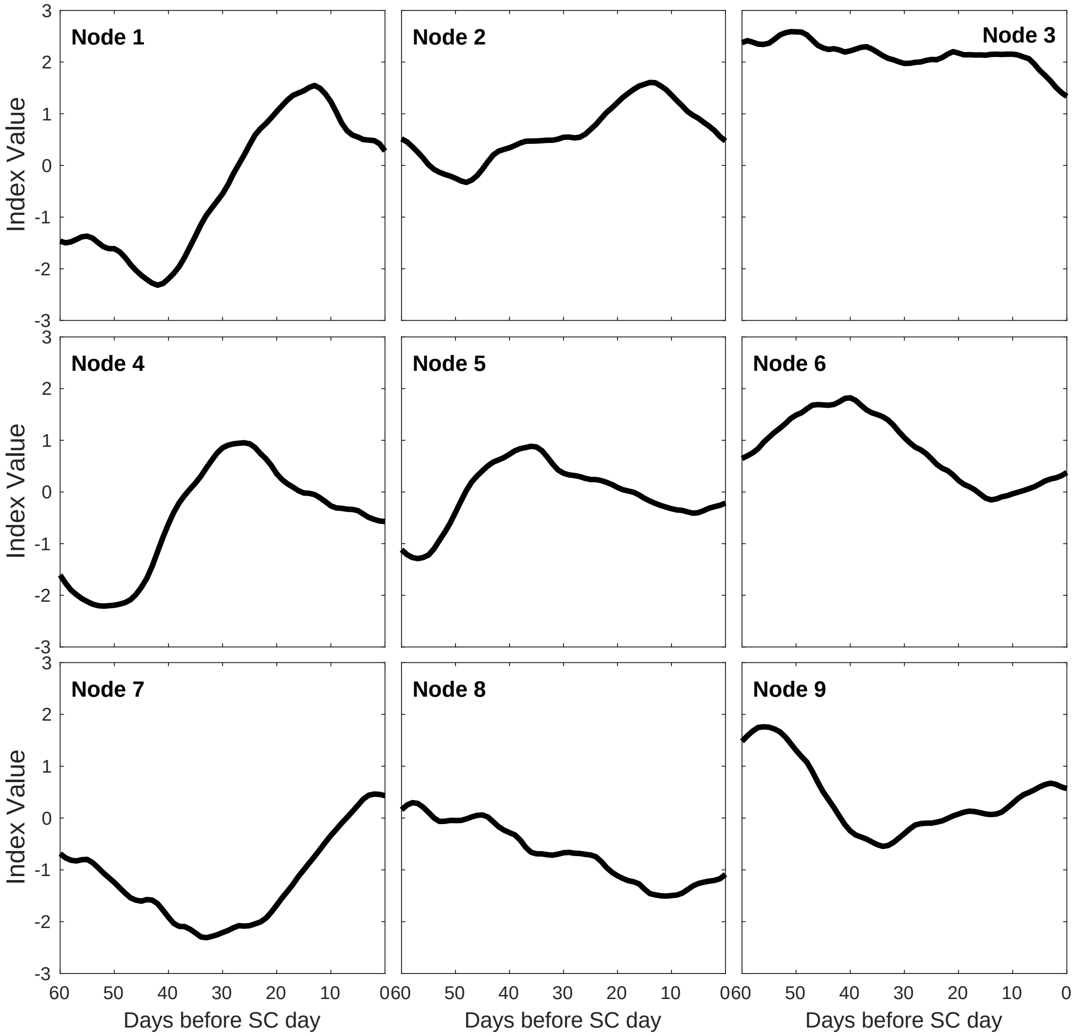

Figure A.1: Sample 3x3 SOM output, corresponding to MAM AO60. Reprinted from Brown and Nowotarski (2020), with permission from American Meteorological Society.

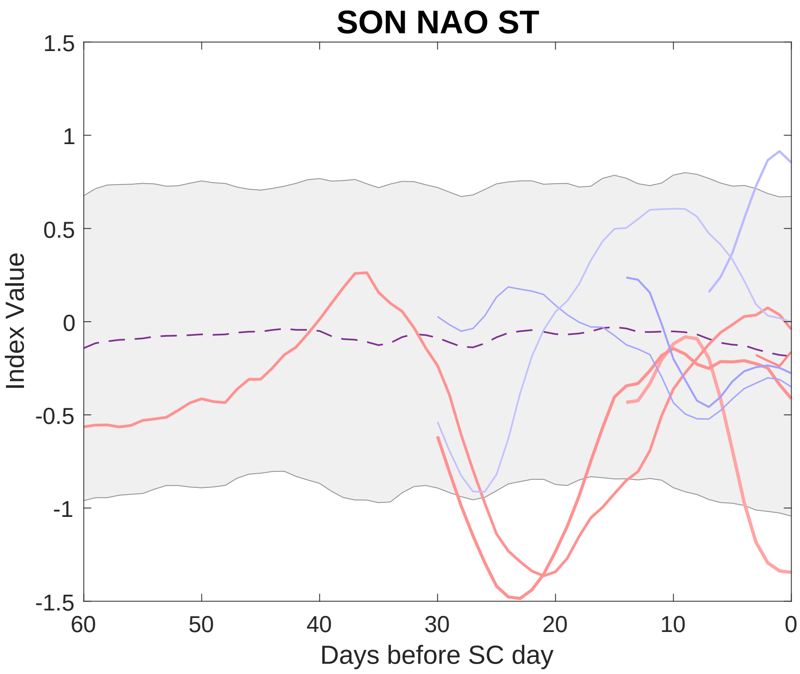

Figure A.2: Significantly tornadic NAO patterns (in red) and null patterns (in blue) associated with SON period, with same line attributes as Figure 2.2. Reprinted from Brown and Nowotarski (2020), with permission from American Meteorological Society.

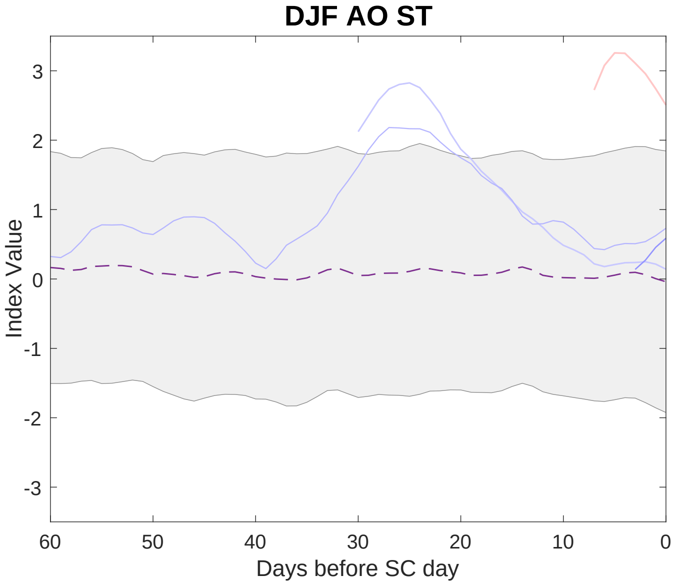

Figure A.3: Significantly tornadic AO patterns (in red) and null patterns (in blue) associated with DJF period, with same line attributes as Figure 2.2. Reprinted from Brown and Nowotarski (2020), with permission from American Meteorological Society.

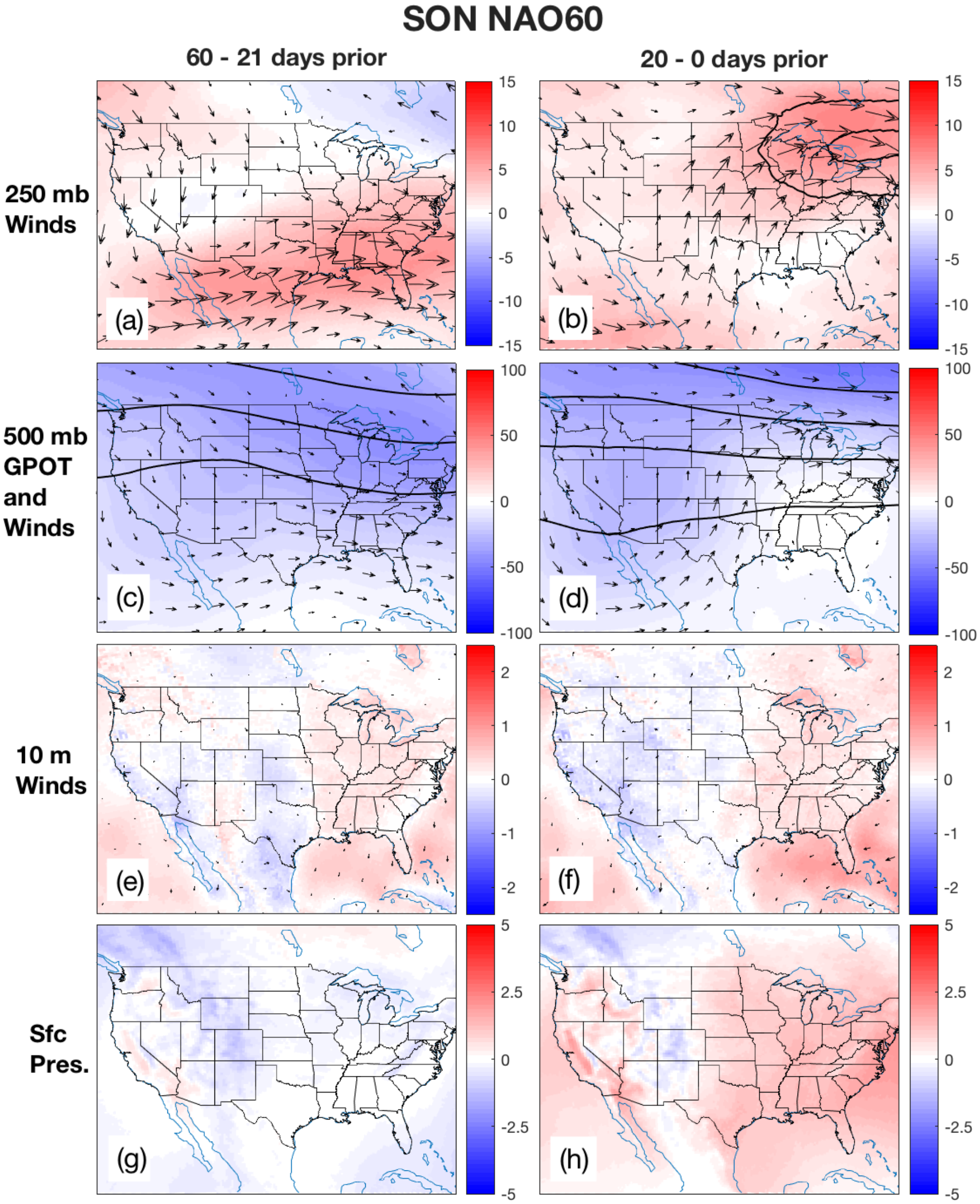

Figure A.4: Composite anomalies associated with SON NAO60 pattern consisting of (a)-(b) 250-mb speed anomalies in m s^{-1} and wind anomaly vectors (with node average speed contours 40 and 45 m s^{-1} shown in black), (c)-(d) 500-mb geopotential height anomalies in meters and wind anomaly vectors (with node average height contours of 5500, 5600, 5700, and 5800 m), (e)-(f) 10 m speed anomalies in m s^{-1} and wind anomaly vectors, and (g)-(h) surface pressure anomalies in mb. Reprinted from Brown and Nowotarski (2020), with permission from American Meteorological Society.

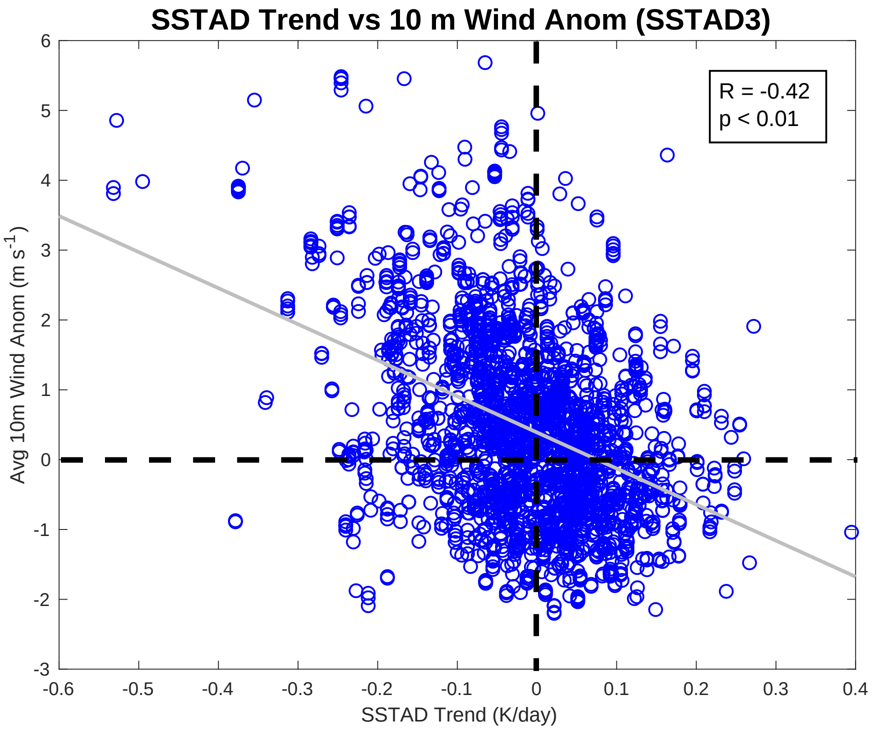

Figure A.5: SSTAD daily trend (in K day^{-1}) and 00Z GOM-averaged 10 m wind anomalies (in m s^{-1}) preceding SC days associated with SSTAD3, with zero lines shown in dotted black, least squares trend line in gray, and associated statistics displayed in legend (upper right). Reprinted from Brown and Nowotarski (2020), with permission from American Meteorological Society.

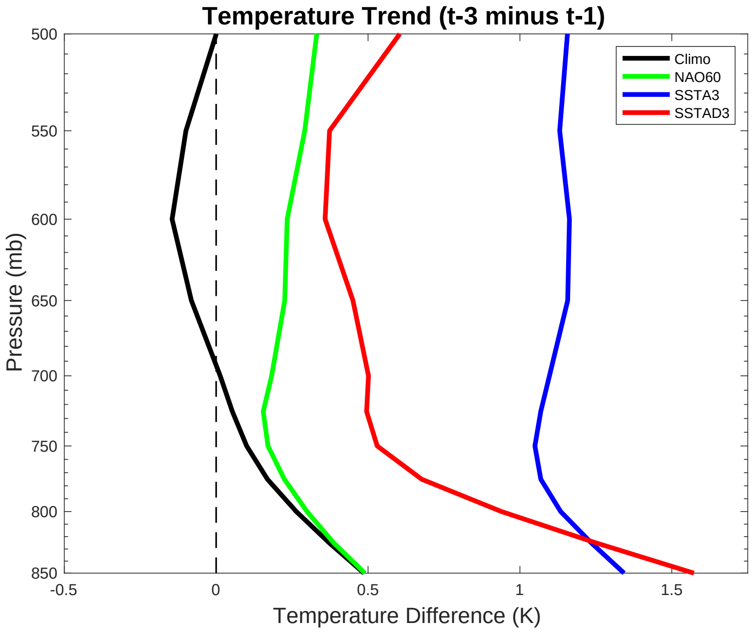

Figure A.6: Difference between domain-averaged temperature profiles (in K) 3 and 1 days out from SC day for SC climatology (black), NAO60 (green), SSTAD3 (red), and SSTA3 (blue), with zero line overlaid in dotted black. Reprinted from Brown and Nowotarski (2020), with permission from American Meteorological Society.

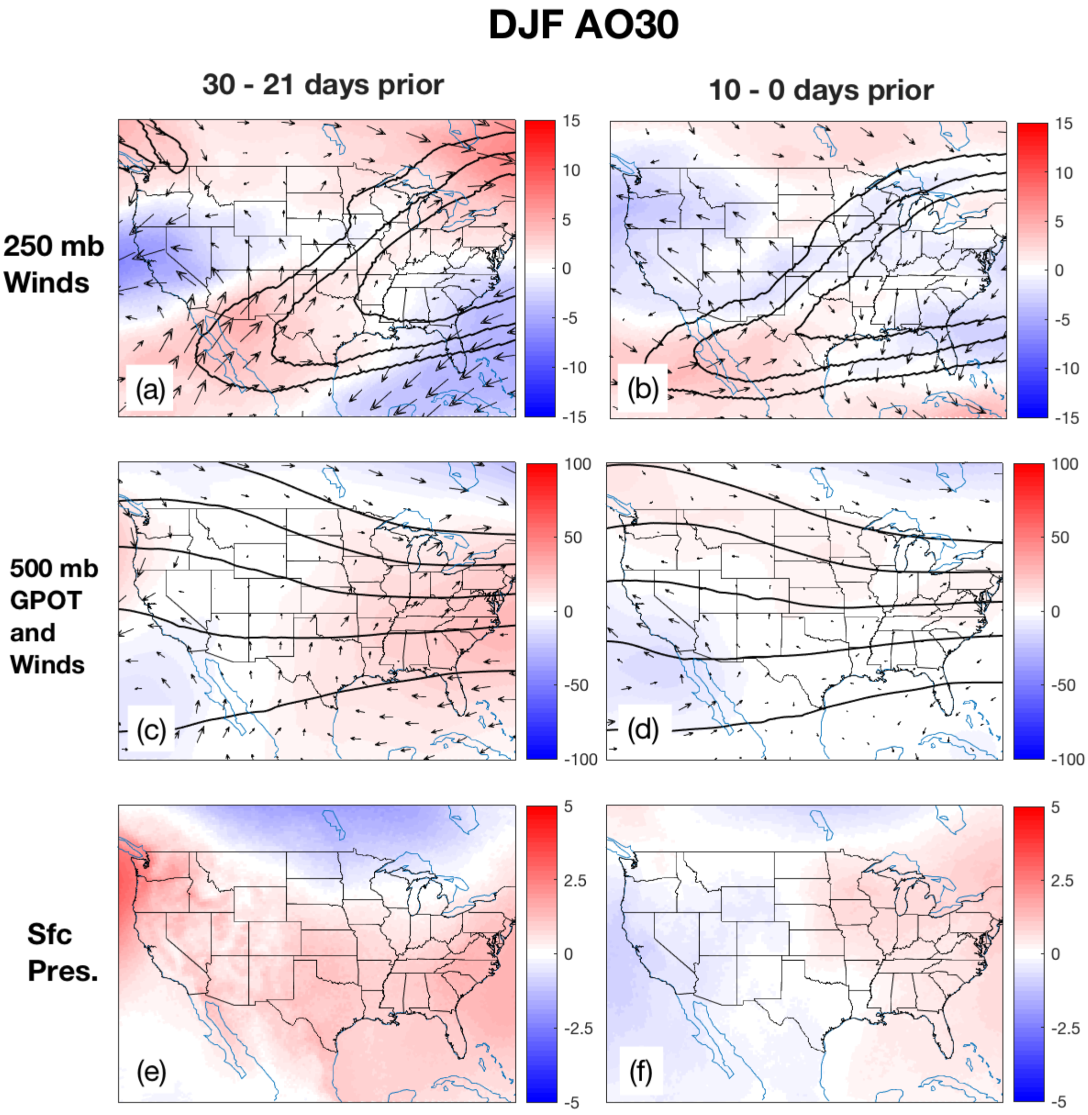

Figure A.7: Composite anomalies associated with DJF AO30 pattern consisting of (a)-(b) 250-mb speed anomalies in m s^{-1} and wind anomaly vectors (with node average speed contours in black of 40, 45, and 50 m s^{-1}), (c)-(d) 500-mb geopotential height anomalies in meters and wind anomaly vectors (with node average height contours of 5400, 5500, 5600, 5700, and 5800 m), and (e)-(f) surface pressure anomalies. Reprinted from Brown and Nowotarski (2020), with permission from American Meteorological Society.

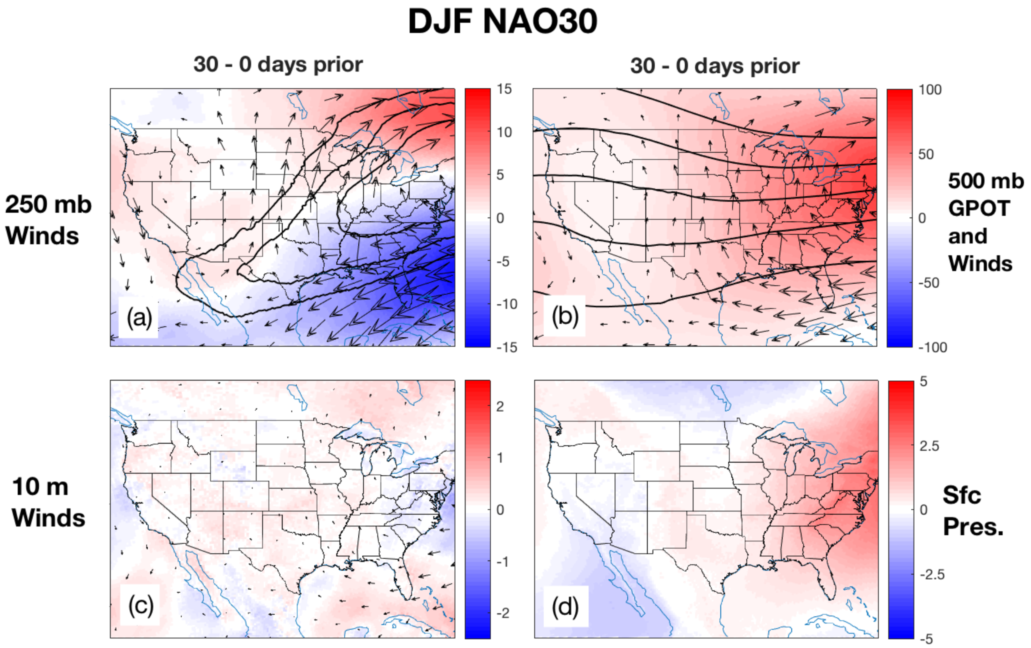

Figure A.8: Composite anomalies associated with DJF NAO30 pattern consisting of (a) 250-mb speed anomalies in m s^{-1} and wind anomaly vectors (with node average speed contours 40, 45, and 50 m s^{-1} shown in black), (b) 500-mb geopotential height anomalies in meters and wind anomaly vectors (with node average height contours of 5500, 5600, 5700, and 5800 m), (c) 10 m speed anomalies in m s^{-1} and wind anomaly vectors, and (d) surface pressure anomalies in mb. Reprinted from Brown and Nowotarski (2020), with permission from American Meteorological Society.

APPENDIX B

CHAPTER 3 APPENDIX

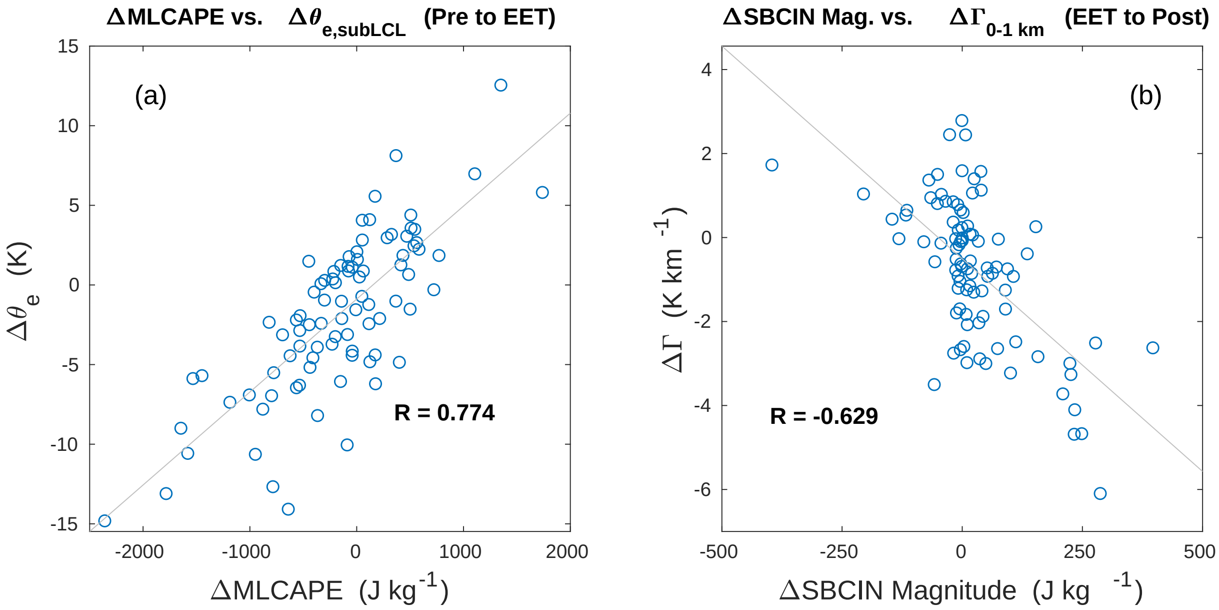

Figure B.1: Correlations between average (a) Pre to EET changes in MLCAPE (in J kg^{-1}) and average sub-LCL equivalent potential temperature (θ_e; in K) and (b) EET to Post changes in SBCIN (in J kg^{-1}) and 0-1 km lapse rate (Γ_{0-1km} in K km^{-1}), during the days contributing to patterns in Figures 3.2-3.4. A linear regression line and R-value for each correlation is shown for reference. Reprinted from Brown et al. (2021), with permission from American Meteorological Society.

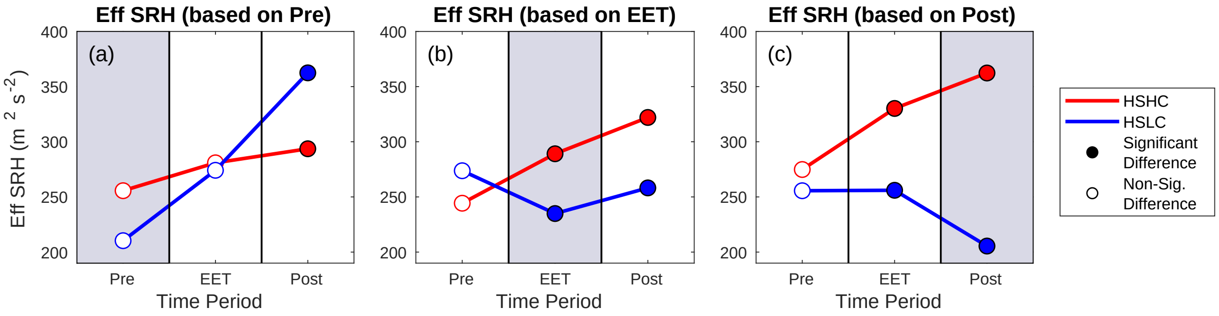

Figure B.2: Time series of average effective layer SRH (Eff SRH; in $m^2\ s^{-2}$), with the same line/color scheme as Figures 3.2-3.4. Reprinted from Brown et al. (2021), with permission from American Meteorological Society.

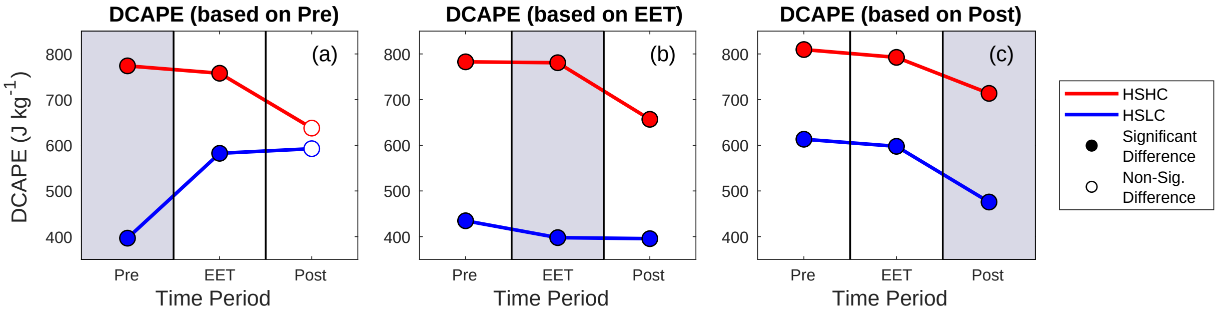

Figure B.3: Time series of average downdraft CAPE (DCAPE; in $J\ kg^{-1}$), with the same line/color scheme as Figures 3.2-3.4. Reprinted from Brown et al. (2021), with permission from American Meteorological Society.

Table B.1: Correlations of thermodynamic variables with average Pre to EET changes in MLCAPE (Columns 1-2) and EET to Post changes in SBCIN (Columns 3-4) for which R values exceed 0.5 in magnitude, during the days contributing to patterns in Figures 3.2-3.4. Reprinted from Brown et al. (2021), with permission from American Meteorological Society.

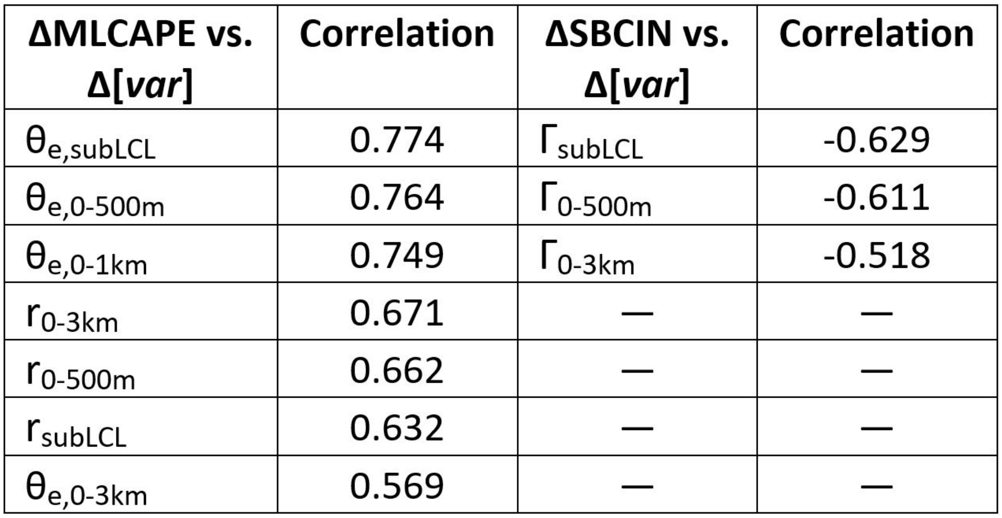

ΔMLCAPE vs. Δ[*var*]	**Correlation**	**ΔSBCIN vs. Δ[*var*]**	**Correlation**
$\theta_{e,\mathrm{subLCL}}$	0.774	Γ_{subLCL}	-0.629
$\theta_{e,\mathrm{0\text{-}500m}}$	0.764	$\Gamma_{\mathrm{0\text{-}500m}}$	-0.611
$\theta_{e,\mathrm{0\text{-}1km}}$	0.749	$\Gamma_{\mathrm{0\text{-}3km}}$	-0.518
$r_{\mathrm{0\text{-}3km}}$	0.671	—	—
$r_{\mathrm{0\text{-}500m}}$	0.662	—	—
r_{subLCL}	0.632	—	—
$\theta_{e,\mathrm{0\text{-}3km}}$	0.569	—	—

Table B.2: Raw sounding-derived variables utilized in TSS analyses, including variable abbreviation and description. Reprinted from Brown et al. (2021), with permission from American Meteorological Society.

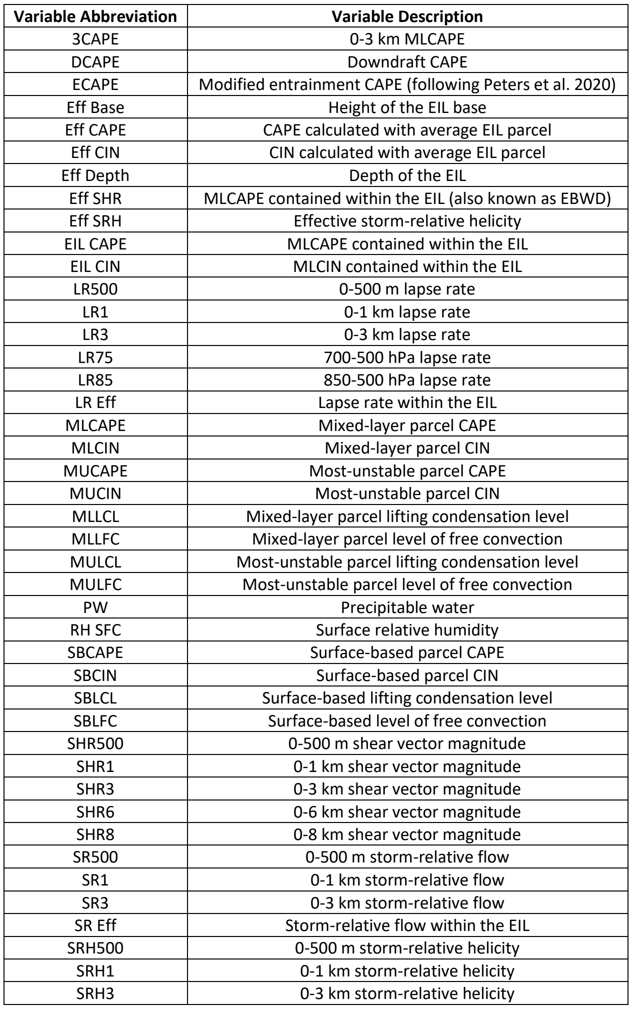

Variable Abbreviation	Variable Description
3CAPE	0-3 km MLCAPE
DCAPE	Downdraft CAPE
ECAPE	Modified entrainment CAPE (following Peters et al. 2020)
Eff Base	Height of the EIL base
Eff CAPE	CAPE calculated with average EIL parcel
Eff CIN	CIN calculated with average EIL parcel
Eff Depth	Depth of the EIL
Eff SHR	MLCAPE contained within the EIL (also known as EBWD)
Eff SRH	Effective storm-relative helicity
EIL CAPE	MLCAPE contained within the EIL
EIL CIN	MLCIN contained within the EIL
LR500	0-500 m lapse rate
LR1	0-1 km lapse rate
LR3	0-3 km lapse rate
LR75	700-500 hPa lapse rate
LR85	850-500 hPa lapse rate
LR Eff	Lapse rate within the EIL
MLCAPE	Mixed-layer parcel CAPE
MLCIN	Mixed-layer parcel CIN
MUCAPE	Most-unstable parcel CAPE
MUCIN	Most-unstable parcel CIN
MLLCL	Mixed-layer parcel lifting condensation level
MLLFC	Mixed-layer parcel level of free convection
MULCL	Most-unstable parcel lifting condensation level
MULFC	Most-unstable parcel level of free convection
PW	Precipitable water
RH SFC	Surface relative humidity
SBCAPE	Surface-based parcel CAPE
SBCIN	Surface-based parcel CIN
SBLCL	Surface-based lifting condensation level
SBLFC	Surface-based level of free convection
SHR500	0-500 m shear vector magnitude
SHR1	0-1 km shear vector magnitude
SHR3	0-3 km shear vector magnitude
SHR6	0-6 km shear vector magnitude
SHR8	0-8 km shear vector magnitude
SR500	0-500 m storm-relative flow
SR1	0-1 km storm-relative flow
SR3	0-3 km storm-relative flow
SR Eff	Storm-relative flow within the EIL
SRH500	0-500 m storm-relative helicity
SRH1	0-1 km storm-relative helicity
SRH3	0-3 km storm-relative helicity

Table B.3: Environmental (top portion) and derived (bottom portion) HSHC and HSLC tor predictors in each examined temporal period, ranked by maximum TSS magnitude (with associated variable threshold shown in parentheses); bolded values indicate a maximum TSS value whose sign was negative. The variables (and their associated units) are as follows - shear/SR-flow quantities (m s^{-1}), SRH quantities (m^{2} s^{-2}), CAPE/CIN quantities (J kg^{-1}), lapse rates (K km^{-1}), LCL/LFC/Eff Base quantities (meters AGL), PW (inches), RH (%), and derived variables (dimensionless). Reprinted from Brown et al. (2021), with permission from American Meteorological Society.

HSHC Pre		HSLC Pre		HSHC EET		HSLC EET		HSHC Post		HSLC Post	
SRH1	0.49 (166.6)	Eff SRH	0.272 (206.2)	SRH1	0.469 (202.1)	PW	0.241 (1.4)	SRH1	0.361 (285.6)	PW	0.284 (1.4)
SHR1	0.468 (12.1)	PW	0.255 (1.5)	SHR1	0.427 (13.5)	DCAPE	**0.221 (263)**	SRH500	0.352 (201.5)	SBCAPE	0.208 (3.4)
SRH500	0.455 (123.6)	RH SFC	0.248 (79.3)	SRH3	0.423 (285.1)	LR75	**0.219 (6.2)**	Eff SRH	0.34 (371.8)	LR500	0.208 (141.2)
SHR500	0.449 (7)	SRH3	0.225 (375.2)	Eff SRH	0.421 (222.7)	SRH1	0.201 (293.9)	SRH3	0.337 (311.3)	LR85	**0.196 (6.2)**
SRH3	0.432 (206.3)	DCAPE	**0.213 (502.3)**	SRH500	0.356 (142.6)	SRH500	0.2 (152.8)	SR3	0.315 (10.2)	DCAPE	**0.192 (432.1)**
Eff SRH	0.426 (204.5)	SRH500	0.213 (162.9)	SHR3	0.347 (19.2)	RH SFC	0.192 (79.3)	SHR500	0.297 (14.6)	LR1	0.191 (4.1)
SBLCL	**0.396 (524.8)**	SRH1	0.209 (311.4)	SHR6	0.317 (26.5)	MLLCL	**0.181 (670.9)**	SR Eff	0.261 (11.6)	SHR1	0.179 (19.9)
LR1	**0.394 (7.7)**	EIL CAPE	0.205 (0.3)	SHR500	0.316 (10.8)	SHR500	0.171 (12.5)	SHR3	0.26 (21.6)	MLCIN	0.175 (-47.8)
MLLCL	**0.369 (772.9)**	MLLCL	**0.195 (724.3)**	SR500	0.312 (15.9)	LR85	**0.164 (6)**	SHR1	0.255 (19)	LR75	**0.174 (6.5)**
RH SFC	0.367 (78.8)	SHR1	0.195 (16.2)	MLLCL	**0.311 (753.3)**	SBCAPE	0.162 (81.6)	SR500	0.226 (15.1)	SRH3	0.172 (419.7)
STP-T03	0.446 (3.4)	STP-T03	0.28 (1)	STP-T03	0.464 (3.2)	STP-FCIN	0.252 (0.1)	STP-F	0.316 (2.7)	STP-FCIN	0.228 (0.4)
STP500*	0.414 (1.8)	STP-FCIN	0.271 (0.1)	STP-E	0.396 (2.5)	STP-F	0.237 (0.2)	STP500	0.314 (4.3)	STP-F	0.223 (0.1)
STP500	0.382 (1.7)	EHI	0.257 (0.6)	SCP	0.391 (12.3)	STP-T03	0.182 (0.7)	STP-E	0.313 (2.8)	STP-T03	0.203 (1.1)
STP-F	0.36 (1.8)	STP500*	0.237 (0.1)	CSCP	0.374 (12.3)	STP500*	0.174 (0.3)	STP-T03	0.308 (6.9)	STP500*	0.199 (0.3)
STP-E	0.352 (1.6)	STP500	0.228 (0)	EHI	0.342 (2.9)	STP500	0.16 (0.3)	STP500*	0.303 (4.3)	EHI	0.19 (0.5)

Table B.4: As in Table C.3, but for sigtor predictors. Reprinted from Brown et al. (2021), with permission from American Meteorological Society.

HSHC Pre		HSLC Pre		HSHC EET		HSLC EET		HSHC Post		HSLC Post	
SRH1	0.59 (197)	Eff Depth	0.485 (1715.9)	SRH1	0.619 (248.9)	SRH500	0.375 (212.5)	Eff SRH	0.527 (422)	SHR1	0.428 (19.9)
SRH500	0.586 (98.9)	SR500	0.453 (18.7)	SHR1	0.61 (14.6)	SRH1	0.37 (278.8)	SRH3	0.519 (444.2)	SRH1	0.38 (436.6)
SHR500	0.581 (8.9)	SR1	0.453 (16.1)	SRH3	0.586 (343.6)	Eff SHR	0.347 (23.1)	SRH500	0.508 (233.7)	SHR500	0.368 (14.3)
SHR1	0.567 (12.3)	Eff SRH	0.44 (227.2)	Eff SRH	0.562 (330.5)	SRH3	0.34 (472.5)	SHR500	0.5 (15.2)	SBLFC	**0.362 (2597.1)**
Eff SRH	0.561 (278.6)	Eff SHR	0.414 (23.5)	SHR3	0.554 (20.4)	SHR1	0.339 (18.4)	SRH1	0.483 (390.2)	SRH3	0.357 (416.7)
SRH3	0.556 (285)	MLCAPE	0.367 (253.2)	SRH500	0.524 (162.5)	SHR500	0.31 (12.3)	SHR1	0.481 (19.8)	LR1	0.353 (4.4)
SR500	0.526 (16)	SRH500	0.352 (162.9)	SHR6	0.505 (27.8)	SR500	0.306 (15.9)	SHR3	0.408 (21.6)	SBCAPE	0.352 (157)
SHR3	0.492 (23.5)	3CAPE	0.337 (2.7)	SR500	0.499 (17.5)	Eff SRH	0.298 (321.2)	SR3	0.405 (10.2)	SR Eff	0.348 (12.8)
SR1	0.48 (15.1)	SBCAPE	0.33 (72.6)	SHR500	0.496 (10.8)	SR1	0.262 (13.9)	SR500	0.391 (16.2)	Eff SHR	0.326 (24.8)
SHR6	0.422 (32)	EIL CAPE	0.33 (2.3)	Eff SHR	0.459 (27.9)	LR75	**0.254 (6.2)**	SR1	0.383 (13.9)	PW	0.325 (1.4)
STP-T03	0.608 (3.6)	EHI	0.579 (0.7)	STP-T03	0.687 (4.2)	STP500*	0.406 (0.5)	STP-T03	0.485 (6.9)	STP-F	0.423 (0.2)
STP500*	0.586 (1.8)	STP-T03	0.53 (1)	STP-E	0.585 (3)	STP-T03	0.398 (0.8)	STP-E	0.442 (2.8)	STP-FCIN	0.416 (0.4)
CSCP	0.552 (13)	STP500	0.507 (0)	SCP	0.584 (13.2)	STP-F	0.398 (0.4)	STP500	0.442 (4.3)	STP500*	0.398 (0.3)
SCP	0.547 (13)	STP-F	0.489 (0.4)	CSCP	0.564 (13.2)	STP-FCIN	0.374 (0.4)	STP500*	0.431 (4.3)	EHI	0.352 (0.4)
STP500	0.538 (1.8)	STP500*	0.487 (0.7)	EHI	0.544 (3.4)	EHI	0.358 (0.4)	STP-F	0.419 (2.6)	STP-T03	0.341 (0.4)

Table B.5: As in Table C.3, but for supercell tor predictors. Reprinted from Brown et al. (2021), with permission from American Meteorological Society.

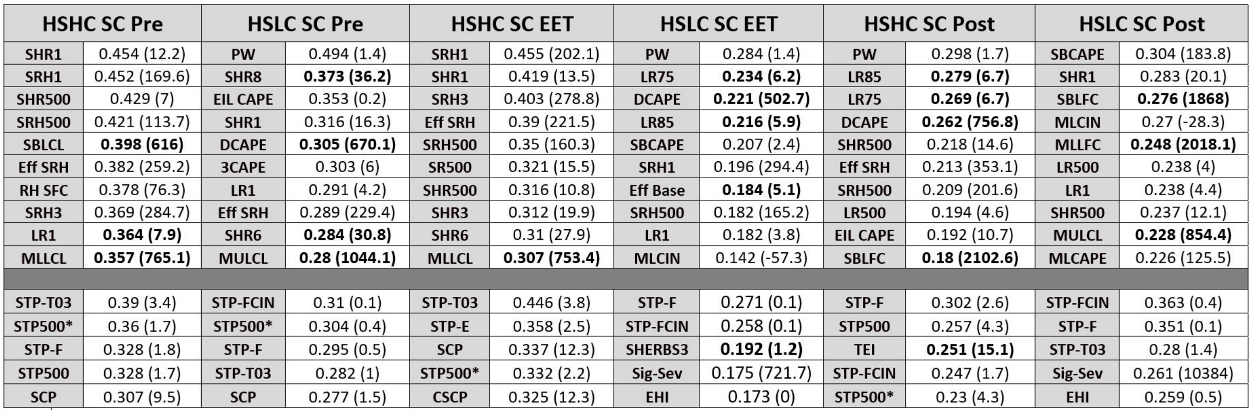

HSHC SC Pre		HSLC SC Pre		HSHC SC EET		HSLC SC EET		HSHC SC Post		HSLC SC Post	
SHR1	0.454 (12.2)	PW	0.494 (1.4)	SRH1	0.455 (202.1)	PW	0.284 (1.4)	PW	0.298 (1.7)	SBCAPE	0.304 (183.8)
SRH1	0.452 (169.6)	SHR8	**0.373 (36.2)**	SHR1	0.419 (13.5)	LR75	**0.234 (6.2)**	LR85	**0.279 (6.7)**	SHR1	0.283 (20.1)
SHR500	0.429 (7)	EIL CAPE	0.353 (0.2)	SRH3	0.403 (278.8)	DCAPE	**0.221 (502.7)**	LR75	**0.269 (6.7)**	SBLFC	**0.276 (1868)**
SRH500	0.421 (113.7)	SHR1	0.316 (16.3)	Eff SRH	0.39 (221.5)	LR85	**0.216 (5.9)**	DCAPE	**0.262 (756.8)**	MLCIN	0.27 (-28.3)
SBLCL	**0.398 (616)**	DCAPE	**0.305 (670.1)**	SRH500	0.35 (160.3)	SBCAPE	0.207 (2.4)	SHR500	0.218 (14.6)	MLLFC	**0.248 (2018.1)**
Eff SRH	0.382 (259.2)	3CAPE	0.303 (6)	SR500	0.321 (15.5)	SRH1	0.196 (294.4)	Eff SRH	0.213 (353.1)	LR500	0.238 (4)
RH SFC	0.378 (76.3)	LR1	0.291 (4.2)	SHR500	0.316 (10.8)	Eff Base	**0.184 (5.1)**	SRH500	0.209 (201.6)	LR1	0.238 (4.4)
SRH3	0.369 (284.7)	Eff SRH	0.289 (229.4)	SHR3	0.312 (19.9)	SRH500	0.182 (165.2)	LR500	0.194 (4.6)	SHR500	0.237 (12.1)
LR1	**0.364 (7.9)**	SHR6	**0.284 (30.8)**	SHR6	0.31 (27.9)	LR1	0.182 (3.8)	EIL CAPE	0.192 (10.7)	MULCL	**0.228 (854.4)**
MLLCL	**0.357 (765.1)**	MULCL	**0.28 (1044.1)**	MLLCL	**0.307 (753.4)**	MLCIN	0.142 (-57.3)	SBLFC	**0.18 (2102.6)**	MLCAPE	0.226 (125.5)
STP-T03	0.39 (3.4)	STP-FCIN	0.31 (0.1)	STP-T03	0.446 (3.8)	STP-F	0.271 (0.1)	STP-F	0.302 (2.6)	STP-FCIN	0.363 (0.4)
STP500*	0.36 (1.7)	STP500*	0.304 (0.4)	STP-E	0.358 (2.5)	STP-FCIN	0.258 (0.1)	STP500	0.257 (4.3)	STP-F	0.351 (0.1)
STP-F	0.328 (1.8)	STP-F	0.295 (0.5)	SCP	0.337 (12.3)	SHERBS3	**0.192 (1.2)**	TEI	**0.251 (15.1)**	STP-T03	0.28 (1.4)
STP500	0.328 (1.7)	STP-T03	0.282 (1)	STP500*	0.332 (2.2)	Sig-Sev	0.175 (721.7)	STP-FCIN	0.247 (1.7)	Sig-Sev	0.261 (10384)
SCP	0.307 (9.5)	SCP	0.277 (1.5)	CSCP	0.325 (12.3)	EHI	0.173 (0)	STP500*	0.23 (4.3)	EHI	0.259 (0.5)

Table B.6: As in Table C.3, but for supercell sigtor predictors. Reprinted from Brown et al. (2021), with permission from American Meteorological Society.

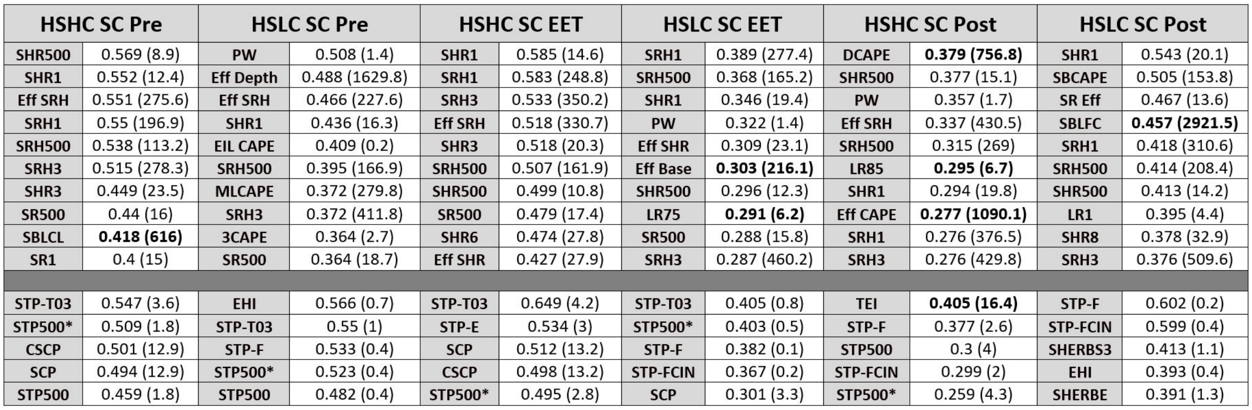

HSHC SC Pre		HSLC SC Pre		HSHC SC EET		HSLC SC EET		HSHC SC Post		HSLC SC Post	
SHR500	0.569 (8.9)	PW	0.508 (1.4)	SHR1	0.585 (14.6)	SRH1	0.389 (277.4)	DCAPE	**0.379 (756.8)**	SHR1	0.543 (20.1)
SHR1	0.552 (12.4)	Eff Depth	0.488 (1629.8)	SRH1	0.583 (248.8)	SRH500	0.368 (165.2)	SHR500	0.377 (15.1)	SBCAPE	0.505 (153.8)
Eff SRH	0.551 (275.6)	Eff SRH	0.466 (227.6)	SRH3	0.533 (350.2)	SHR1	0.346 (19.4)	PW	0.357 (1.7)	SR Eff	0.467 (13.6)
SRH1	0.55 (196.9)	SHR1	0.436 (16.3)	Eff SRH	0.518 (330.7)	PW	0.322 (1.4)	Eff SRH	0.337 (430.5)	SBLFC	**0.457 (2921.5)**
SRH500	0.538 (113.2)	EIL CAPE	0.409 (0.2)	SHR3	0.518 (20.3)	Eff SHR	0.309 (23.1)	SRH500	0.315 (269)	SRH1	0.418 (310.6)
SRH3	0.515 (278.3)	SRH500	0.395 (166.9)	SRH500	0.507 (161.9)	Eff Base	**0.303 (216.1)**	LR85	**0.295 (6.7)**	SRH500	0.414 (208.4)
SHR3	0.449 (23.5)	MLCAPE	0.372 (279.8)	SHR500	0.499 (10.8)	SHR500	0.296 (12.3)	SHR1	0.294 (19.8)	SHR500	0.413 (14.2)
SR500	0.44 (16)	SRH3	0.372 (411.8)	SR500	0.479 (17.4)	LR75	**0.291 (6.2)**	Eff CAPE	**0.277 (1090.1)**	LR1	0.395 (4.4)
SBLCL	**0.418 (616)**	3CAPE	0.364 (2.7)	SHR6	0.474 (27.8)	SR500	0.288 (15.8)	SRH1	0.276 (376.5)	SHR8	0.378 (32.9)
SR1	0.4 (15)	SR500	0.364 (18.7)	Eff SHR	0.427 (27.9)	SRH3	0.287 (460.2)	SRH3	0.276 (429.8)	SRH3	0.376 (509.6)
STP-T03	0.547 (3.6)	EHI	0.566 (0.7)	STP-T03	0.649 (4.2)	STP-T03	0.405 (0.8)	TEI	**0.405 (16.4)**	STP-F	0.602 (0.2)
STP500*	0.509 (1.8)	STP-T03	0.55 (1)	STP-E	0.534 (3)	STP500*	0.403 (0.5)	STP-F	0.377 (2.6)	STP-FCIN	0.599 (0.4)
CSCP	0.501 (12.9)	STP-F	0.533 (0.4)	SCP	0.512 (13.2)	STP-F	0.382 (0.1)	STP500	0.3 (4)	SHERBS3	0.413 (1.1)
SCP	0.494 (12.9)	STP500*	0.523 (0.4)	CSCP	0.498 (13.2)	STP-FCIN	0.367 (0.2)	STP-FCIN	0.299 (2)	EHI	0.393 (0.4)
STP500	0.459 (1.8)	STP500	0.482 (0.4)	STP500*	0.495 (2.8)	SCP	0.301 (3.3)	STP500*	0.259 (4.3)	SHERBE	0.391 (1.3)

Table B.7: As in Table C.3, but for QLCS tor predictors. Reprinted from Brown et al. (2021), with permission from American Meteorological Society.

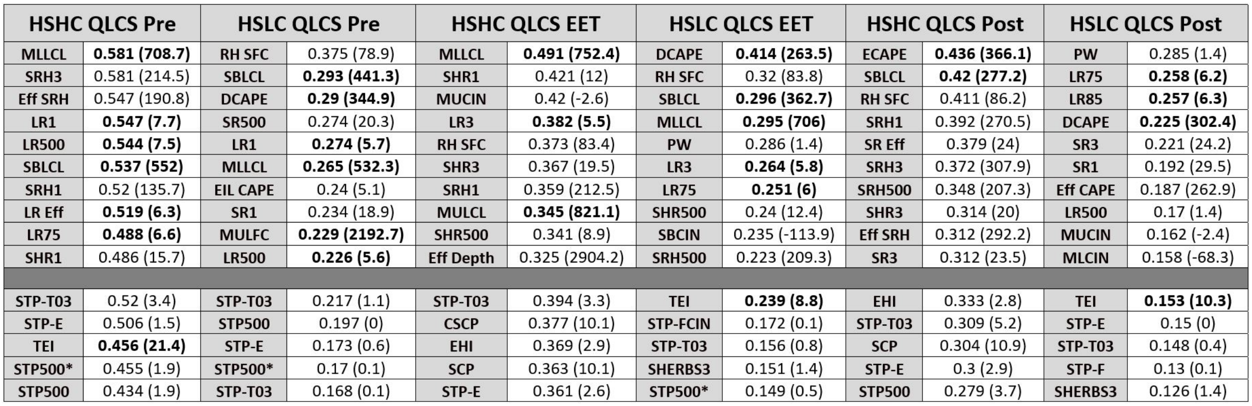

HSHC QLCS Pre		HSLC QLCS Pre		HSHC QLCS EET		HSLC QLCS EET		HSHC QLCS Post		HSLC QLCS Post	
MLLCL	**0.581 (708.7)**	RH SFC	0.375 (78.9)	MLLCL	**0.491 (752.4)**	DCAPE	**0.414 (263.5)**	ECAPE	**0.436 (366.1)**	PW	0.285 (1.4)
SRH3	0.581 (214.5)	SBLCL	**0.293 (441.3)**	SHR1	0.421 (12)	RH SFC	0.32 (83.8)	SBLCL	**0.42 (277.2)**	LR75	**0.258 (6.2)**
Eff SRH	0.547 (190.8)	DCAPE	**0.29 (344.9)**	MUCIN	0.42 (-2.6)	SBLCL	**0.296 (362.7)**	RH SFC	0.411 (86.2)	LR85	**0.257 (6.3)**
LR1	**0.547 (7.7)**	SR500	0.274 (20.3)	LR3	**0.382 (5.5)**	MLLCL	**0.295 (706)**	SRH1	0.392 (270.5)	DCAPE	**0.225 (302.4)**
LR500	**0.544 (7.5)**	LR1	**0.274 (5.7)**	RH SFC	0.373 (83.4)	PW	0.286 (1.4)	SR Eff	0.379 (24)	SR3	0.221 (24.2)
SBLCL	**0.537 (552)**	MLLCL	**0.265 (532.3)**	SHR3	0.367 (19.5)	LR3	**0.264 (5.8)**	SRH3	0.372 (307.9)	SR1	0.192 (29.5)
SRH1	0.52 (135.7)	EIL CAPE	0.24 (5.1)	SRH1	0.359 (212.5)	LR75	**0.251 (6)**	SRH500	0.348 (207.3)	Eff CAPE	0.187 (262.9)
LR Eff	**0.519 (6.3)**	SR1	0.234 (18.9)	MULCL	**0.345 (821.1)**	SHR500	0.24 (12.4)	SHR3	0.314 (20)	LR500	0.17 (1.4)
LR75	**0.488 (6.6)**	MULFC	**0.229 (2192.7)**	SHR500	0.341 (8.9)	SBCIN	0.235 (-113.9)	Eff SRH	0.312 (292.2)	MUCIN	0.162 (-2.4)
SHR1	0.486 (15.7)	LR500	**0.226 (5.6)**	Eff Depth	0.325 (2904.2)	SRH500	0.223 (209.3)	SR3	0.312 (23.5)	MLCIN	0.158 (-68.3)
STP-T03	0.52 (3.4)	STP-T03	0.217 (1.1)	STP-T03	0.394 (3.3)	TEI	**0.239 (8.8)**	EHI	0.333 (2.8)	TEI	**0.153 (10.3)**
STP-E	0.506 (1.5)	STP500	0.197 (0)	CSCP	0.377 (10.1)	STP-FCIN	0.172 (0.1)	STP-T03	0.309 (5.2)	STP-E	0.15 (0)
TEI	**0.456 (21.4)**	STP-E	0.173 (0.6)	EHI	0.369 (2.9)	STP-T03	0.156 (0.8)	SCP	0.304 (10.9)	STP-T03	0.148 (0.4)
STP500*	0.455 (1.9)	STP500*	0.17 (0.1)	SCP	0.363 (10.1)	SHERBS3	0.151 (1.4)	STP-E	0.3 (2.9)	STP-F	0.13 (0.1)
STP500	0.434 (1.9)	STP-T03	0.168 (0.1)	STP-E	0.361 (2.6)	STP500*	0.149 (0.5)	STP500	0.279 (3.7)	SHERBS3	0.126 (1.4)